Structure-Polarization Relationship of Fluorescence labelled Samples and Distinction of Subdiffractional Details

Von der Fakultät für Lebenswissenschaften

der Technischen Universität Carolo-Wilhelmina

zu Braunschweig

zur Erlangung des Grades

eines Doktors der Naturwissenschaften

(Dr. rer. nat.)

genehmigte

D i s s e r t a t i o n

von Nour Murshid Kamel Hafi

aus Kuwait

1. Referent: Prof. Dr. Peter Jomo Walla
2. Referent: Prof. Dr. Karl-Heinz Gericke
eingereicht am: 07.11.2016
mündliche Prüfung (Disputation) am: 16.12.2016

Druckjahr 2017

Vorveröffentlichungen der Dissertation

Teilergebnisse aus dieser Arbeit wurden mit Genehmigung der Fakultät für Lebenswissenschaften, vertreten durch den Mentor der Arbeit, in folgenden Beiträgen vorab veröffentlicht:

Publikationen

1. Hafi, N., Grunwald, M., van den Heuvel, L. S., Aspelmeier, T. et al. Reply to "Polarization modulation adds little additional information to super-resolution fluorescence microscopy". Nat Meth 13, 8-9, (2016).
2. N. Hafi, M. Grunwald, L. S. van den Heuvel, T. Aspelmeier, J.-H. Chen, M. Zagrebelsky, O. M. Schütte, C. Steinem, M. Korte, A. Munk and P. J. Walla, "Fluorescence nanoscopy by polarization modulation and polarization angle narrowing", Nat. Methods, 11, 579-584 (2014).

Patente

1. WALLA, P., J. & HAFI, N. HIGH RESOLUTION LIGHT MICROSCOPE. Germany patent 12805993.8 - 1562 (2013).

Tagungsbeiträge

1. N. Hafi, M. Grunwald, L. S. van den Heuvel, P. J. Walla,. Resolution enhancement using super-resolution by polarization demodulation (SPoD) and excitation polarization angle narrowing (Ex-PAN), P 123, Annual Meeting of the German Biophysical Society, Luebeck Germany, 14-17 September 2014.

Contents

Glossary of Symbols and Acronyms

AFM	Atomic Force Microscopy
BS	Beam-splitter
BSA	Bovine Serum Albumin
biotin-BSA	biotin conjugated Bovine Serum Albumin
CLSM	Confocal Laser-Scanning Microscope
CW	Constant wave
DE-PBS	Dielectric Polarizing beam splitter
DM	Dichroic Mirror
DOE	Diffractive Optical Element
EGFP	Enhanced green fluorescence protein
EM	Electron Microscopy
FWHM	Full Width at Half Maximum
GUVs	Giant unilamellar vesicles
IR	Infra-red
NA	Numerical Aperture
nM	nanometer
nm	Nanometer
OPE	One Photon Excitation
OPO	Optical Parametric Oscillator
PALM	Photoactivated Localization Microscopy
PBS	Phosphate buffered saline
PP	Periodically poled
PSF	Point Spread Function
PSTM	Photon Scanning Tunneling Optical Microscope
pM	picometer
RESOLFT	Reversible Saturable/Switchable Optically Linear Fluorescence Transition-microscopy
SICM	Scanning Ion-Conductance Microscopy

SNOM	Scanning near-field optical microscopy
SPoD	Super-resolution by Polarization Demodulation
SSIM	Saturated structured illumination microscopy
STED	Stimulated Emission Depletion Microscopy
STM	Scanning Tunneling Microscopy
STOM	Scanning Tunneling Optical Microscope
STORM	Stochastic Optical Reconstruction Microscopy
ssDNA	Single stranded DNA
TEM	Transmission Electron Microscopy
TIR	Total Internal Reflection
TIRF or TIRFM	Total Internal Reflection Fluorescence Microscopy
TPE	Two Photon Excitation
UV	Ultra Violet
VIS.	Visible
W	Watt
µL	microliter
µm	micrometer

1 Objective of the Work

Fluorescent labelling in optical light microscopy is a very widespread approach to gain detailed insights into the structure of samples under investigation. However, the labelling procedures, the selected labels as well as the linking of the fluorescent markers to the targeted structure have a very large influence on the results obtained and the type of additional information contained in the fluorescence data.

The objective of this work is to explore additional information contained in the orientation of fluorescence markers labelled to various structures. To this end, a large variety of differently labelled samples was investigated, ranging from single molecules up to samples of highly dense fluorescence. Samples of rather homogeneous label orientation with close orientation structure relationships (phalloidin labelled actin filaments and Texas Red-DHPE labeled GUVs) were compared to samples of rather heterogeneous label orientations (single molecules, EGFP labelled hippocampal neurons). In addition samples with very dynamic fluorescent dyes mobility, albeit still having structure dependent preferred average labeled orientations, (Texas Red-DHPE labelled GUVs) were compared to samples with rather rigid fluorescent dyes orientation (single molecules, fixed EGFP labelled hippocampal neurons). This large range of investigated samples provided valuable insight into the information content provided by molecular orientation. The investigation also revealed new possibilities and exposed limitations when using this information to discern labelled structures on different length scales, including subdiffractional distance regimes.

In order to explore the orientation dependence of the emission of fluorescently labelled samples, the polarization of excitation light was periodically modulated with a constant and well defined frequency. This frequency was accurately synchronized with the video frame rate of the camera system. The advantage of modulating the excitation polarization in a wide field system rather than the differentiation of emission polarization is the intrinsic spatial stability in the optical detection path-way. This prevents shifting in the detected image when the polarization is changed in the detection path or when two images of different po-

larization are imaged onto different parts of the CCD camera. In summary, it allows for comparison of subdiffractional polarization details in a correction free manner. The resulting data observed in this way demonstrates that, depending on the label-structure relationship of the samples, valuable additional information can be obtained about the underlying structures. It reveals that the differentiation of subdiffractional structural details is possible based on different molecular orientations. The approach can be applied to virtually any fluorescence marker, when the markers have a preferred orientation, and with a standard optical microscopy setup. It can also be applied to various excitation and detection schemes such as two- photon excitation microscopy [1]. In summary, this work demonstrates that different molecular orientations or different structurally preferred orientations can be observed in a wide range of samples and that molecular orientations can differentiate subdiffractional details.

2 Introduction

2.1 Light interaction with molecules

Photons have wave-like and particle-like nature, as well as electrons. The interaction between light of a certain energy and a molecule with specific transition density is mostly probable when the electric field oscillation of the light is parallel with the transition dipole moment vector. The transition dipole moment can be defined as the dipole moment of the oscillating charge density and a measure of electronic charge shift during transition[2]. In other words, the transition dipole moment is the direction and magnitude of the change in the charge distribution during transition. The dipole moment can be calculated using the wave functions of the corresponding states (2.1):

$$\vec{M}_{I\to F} = \int \psi_{\mathrm{F}}^{*}(\vec{r}) e\, \vec{r} \psi_{\mathrm{I}}(\vec{r}) \mathrm{d}V \tag{2.1}$$

Where ψ_{F}^{*} is the molecule wave function in the final state; e is the magnitude of the elementary charge; $\vec{\mathrm{r}}$ is the three dimensional coordinates which have their origin in the center of the molecule charge distribution and ψ_{I} is the molecule wave function in the initial state. The probability of exciting a molecule is at maximum when the transition dipole moment vector of the molecule is parallel to the oscillation vector of the electric field (polarization vector). An increase in the transition dipole moment vector increases the probability of absorbing a photon when the energy of photon and polarization match up with the energy difference of the transition states. The parity selection rule determines whether a transition in a certain molecule is allowed (u→g, g→u) or not allowed (u→u, g→g). After molecules have absorbed a photon and the electron is in the excited state, the electron can revert to the ground state in a radiative path (fluorescence) or in a non-radiative path (internal conversion, intersystem crossing). The emitted photon would still have the same polarization; however, molecules usually diffuse and rotate fast enough thus shifting the polarization of emission.

2.2 Linear Polarized light Rotation

A linear polarized light is produced by simply using a polarizing filter which allows only one plane of the unpolarized light to pass through. Most laser systems generate a high quality of linear polarized light. Waveplates are transparent bireferingent optics that are usually made from crystal quartz. Waveplates have a fast axis (extraordinary, n_e) and a slow axis (ordinary, n_o) and the light travels through these axis in velocities that are inversely proportional to the refractive indices of each axis. The difference in velocities results in a difference in the phase delay of the light polarization when both beams recombine and therefore waveplates are also called optical retarders. The retardance (θ) that occurs when the incident light is linearly polarized is described in the following formula:

$$\theta = \frac{2\pi l(n_e - n_o)}{\lambda} \tag{2.2}$$

Here, l is the thickness of the crystal and λ is the wavelength. According to this equation, adjusting the thickness of the crystal and Δn for a certain wavelength can result in a calculated phase shift between the two polarization components. A quarter waveplate is one example of a retarder that shifts the phase of one polarization component a quarter of the wave $\lambda/4$ relative to other polarization component. When the incident linear polarized light is at an angle of 45° to the fast or slow axes, the exiting light is circularly polarized once it recombines. Depending on which phase of the polarization component is shifted, the result will be a left or a right handed circular polarized light (Figure 2-1). A second quarter wave plate will then convert the circular polarized light into a linear polarized light as illustrated in Figure 2-1. When the angle of the incident linear polarized light is at an angle of 45° to the fast or slow axes, it generates equal amounts of fast and slow wave components and a circular polarized light is produced. Placing two quarter waveplates one after the other produces the same effect as using a half waveplate. A half waveplate retards one half of the wave $\lambda/2$. As a result, the incident linear polarized light will rotate at an angle double that of the angle between the incident beam's input plane of polarization and the retarder axes as demonstrated in in Figure 2-2.

The plane of linear polarized light can be rotated using two quarter wave plates or one half waveplate. By fixing one quarter waveplate to secure an angle of 45° between the waveplate axes and the incident linear polarized light, a circular polarized light will exit though the first quarter waveplate. The second quarter waveplate will convert the circular polarized light back into a linear polarized light. Rotating the second quarter waveplate will rotate the exiting linear polarized light. On the other hand, the half waveplate directly rotates the polarized light at double that of the angle between the waveplate axes and the incident linear polarized light. This means that by rotating the half waveplate from 0° to 90° the exiting

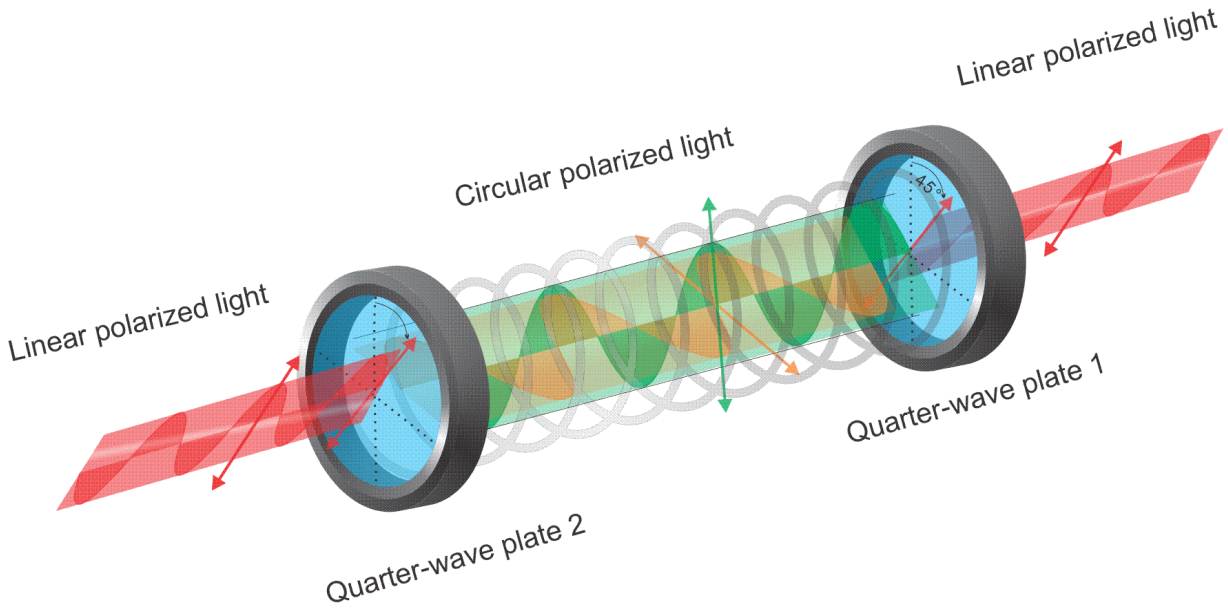

Figure 2-1: Rotation of linearly polarized light using two achromatic quarter-wave plates. The incident linear polarized light passing through the first quarter waveplate is at an angle of 45° to the fast or slow axes. The exiting light when recombined from the slow and fast components is circularly polarized. After passing through the second quarter waveplate the exiting light will be linearly polarized again. Rotating the second quarter wave plate results in rotating the linear polarized light.

polarized light will be rotated at angles from 0° to 180°. Alternatively, the two quarter waveplate system involves rotating the second quarter waveplate from 0°-180° so that the exiting polarized light will be rotated at angles ranging from 0° to 180° (one evolution of rotation). The polarized light completes one evolution of rotation when the half waveplate ro-

tates from 0°-90° or from 90°-180°. When rotating a waveplate, the linear polarized light will interact with the surface of the waveplate covering 360° of rotation. When it comes to the half wave plate there are four regions that can complete one evolution of rotation (0°- 90°, 90°- 180°, 180°- 270°, 270°- 360°). If the incident linear polarized light is ideal then two ranges will be similar (0°- 90° = 180°- 270°, 90°- 180°= 270°- 360°). The difference between these two regions results from the fact that it is hard to achieve an ideal homogeneous wave plate. This problem also arises with quarter waveplates. However, in this case

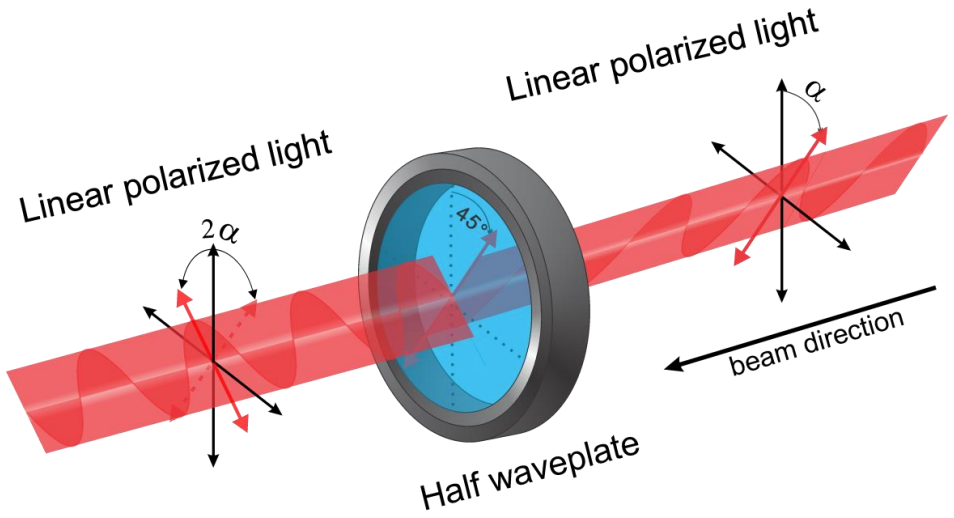

Figure 2-2: Rotation of linearly polarized light using achromatic half-wave plate. The incident linear polarized light with an angle α with the slow axes (red arrow) will rotate by twice the angle (i.e. 2α) when passing through the half waveplate (red dashed arrow and red arrow). Rotating the half waveplate will result in rotating the linear polarized light twice the angle α constantly.

one evolution of rotation requires a rotation of 0°-180°. Thus, the result will stay the same in an ideal polarized light case. In reality, the linear polarized light is non-ideal and is therefore expected to have four different polarized light intensities when half waveplate is used and two different polarized light intensities when two quarter waveplates are used. This is the advantage of the quarter waveplate system over the half waveplate. However, the half waveplate is much easier to align. An achromatic waveplate operates in a wide range of light spectrum.

2.3 History of Microscopes

Optical microscopy, usually referred to as light microscopy, was first invented in the 1590s by the Dutch Zacharias Janssen and his father, Hans Janssen. In the 17th century, Antony van Leeuwenhoek was credited for building a microscope and introducing the first magnified images of biological samples. He was known as the first person to publish observations of the mouth parts and stings of bees, findings he reported to the Royal Society of London in 1673. In 1840, Giovanni Battista Amici was able to increase the resolution of the light microscope by introducing the oil-immersion technique to minimize optical aberrations. In 1855, he introduced the water-immersion objective [3].

Abbe Ernst worked for Carl Zeiss on the scientific basis for designing an optical microscope. In 1872, Zeiss Company manufactured a much higher quality of water immersion objective depending on Abbe's calculations. Meanwhile, Abbe was working on the image formation theory and he noticed that the resolution of optical microscope is diffraction limited. In 1873, Abbe published his theory and described his famous formula in words about the limitation of image resolution [4]. The smallest wave period passing through a structure or the minimum resolvable distance between two distinct objects d is known as Abbe's limit [5].

$$d_{x,y} = \frac{\lambda}{2n \sin \alpha} \qquad d_z = \frac{2\lambda}{n \sin^2 \alpha} \tag{2.3}$$

Where $d_{x,y}$ is the lateral resolution and d_z is the axial resolution. λ is the wavelength of the light, n is the embedding medium refractive index which the light is focused through and α is the half angle of the focused cone exiting the objective lens (Figure 2-3). The term $n \cdot \sin \alpha$ is defined as the numerical aperture, NA. According to Abbe's definition, the maximum achievable resolution depends on the wavelength and the numerical aperture. A few years after Abbe's publication, Lord Rayleigh began an extensive discussion on the mathematical derivation of the image resolution. Rayleigh differs from Abbe in his definition of the resolution between two objects. According to Rayleigh, two points observed with a mi-

croscope and detectors are detected as two Airy discs. The two points are considered to be resolved if the maximum central of one Airy disc observed from one point overlaps with the first minimum of the second Airy disc observed from the second point[5,6].

$$d_{min} = 0.61\frac{\lambda}{n \cdot \sin\alpha} \qquad d_z = \frac{2\lambda n}{n\sin^2\alpha} \tag{2.4}$$

Abbe's and Rayleigh's equations are similar but they differ in the coefficient. The coefficient used in Abbe's lateral resolution equation is 0.5 however, in Rayleigh's lateral resolution, the coefficient is 0.61. Therefore, the lateral resolution calculated with Abbe's equation is less than the one calculated with Rayleigh's equation. The lateral resolution reaches its maximum resolution power when its objective numerical aperture is at maximum and the light emission wavelength is at minimum.

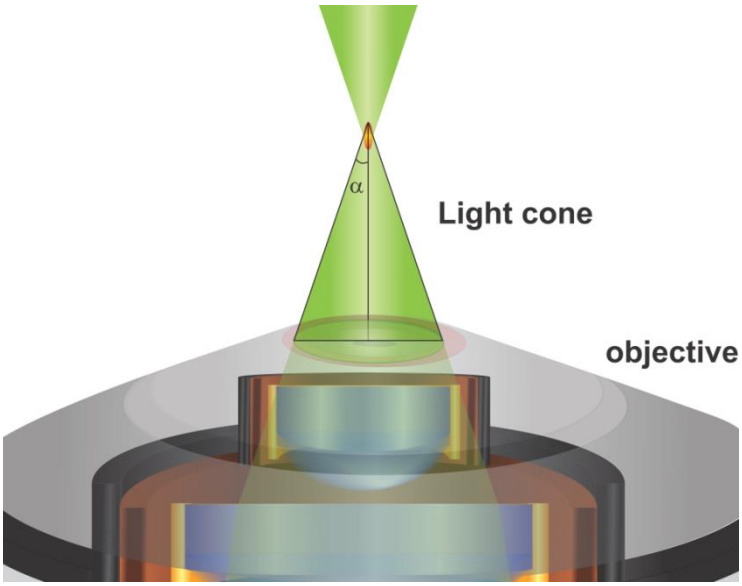

Figure 2-3: Light Cone showing the angle α as it exits a microscope objective.

2.4 Fluorescence Light Microscopy

Despite the magnificent resolution achieved by electron and scanning microscopy, [7,8] imaging the interior of living cells or dynamic living cells in real time is still not possible with these techniques. Moreover, the development of staining and labeling methods of specific cellular components, immuno-labeling, fluorescence in-situ hybridization (FISH), fluorescent proteins and the wide variety of fluorescence markers makes light microscopy a powerful tool for the biological scientist [9-11]. Fluorescence microscopy is a contrast technique that works on detecting fluorescence from, for example, a specifically labeled protein with a fluorescent molecule or fluorescent protein when excited with a specific wavelength. These facts encouraged scientists to place greater focus on finding and developing super resolution fluorescence microscopy techniques, which are capable of surpassing the diffraction limit to sub-10 nm resolution[12]. Super resolution fluorescence microscopy enables biological scientists to study and visualize biological processes at the cellular and subcellular level [7,8,13-22].

2.5 Wide-field Fluorescence Microscopy

Wide-field microscopy is a conventional microscope which illuminates the field of view of the investigated sample with white light. The sample is illuminated from the bottom and observed from the top. Samples labelled with fluorescent markers demand a monochromatic light that matches the excitation wavelength of the fluorescent marker. The emission can be detected from the top of the investigated sample (Brightfield fluorescence microscopy). The emission can also be detected from the bottom if a suitable dichroic mirror is used. The dichroic mirror reflects the excitation light and transmits the emission light towards a detector (inverted fluorescence microscopy). The advantage of inverted microscopy is that the detector is not on the same path as the excitation light. This avoids interference with the detected emission light while the use of good optical filters help to block out all other wavelengths differs from the emission wavelength. Sensitive photodetectors are beneficial for achieving a good resolution or for detecting single molecules. An Electron Multiplying Charge Coupled Device (EMCCD camera) is a very sensitive detector which

has a low readout noise and can detect a single photon very efficiently. An inverted wide-field fluorescence microscope with an EMCCD camera can provide diffraction-limited images of samples and specimens [23].

2.6 Two-Photon Excitation Fluorescence Microscopy

Two-Photon Excitation (TPE) is a nonlinear optical process where the electron cloud responds to the strong electric field component non-linearly. This response causes the two photons to react with the molecule simultaneously. The sum of the two photon energies should correspond to the energy difference between the molecular transition states. The probability of a molecule absorbing two photons simultaneously is proportional to the square of excitation light intensity:

$$P_{Absorption}^{Two-Photon} = I_{Excitation}^{2} \tag{2.5}$$

The advantage of two-photon excitation microscopy over conventional microscopy is that the special and axial resolution is improved down to the diffraction limit. The resolution enhancement is possible because observation is restricted to the focal region of two-photon excitation. One-photon excitation (OPE) also concentrates on the focal region. The difference however, is that one photon excitation occurs with low light intensity resulting in excitation of regions other the focal regions. This obstacle was solved through confocal microscopy by using a pinhole in the detection path. On the other hand, two-photon excitation occurs only in the focal region because a high light intensity is always necessary for excitation. Another advantage of TPE microscopy is that the depth of penetration into the specimen can reach up to 200 mm. The difference between the TPE wavelength and its emission wavelength is also very high relative to OPE wavelength. This difference enables an easy optical alignment and very little overlap in wavelengths. Because the focal region of the TPE in the field of view is about 500 nm using a good pulsed laser system, a scanning system is required in order to produce an image.

2.7 Light Microscopy Techniques

2.7.1 Near field Optical Microscopy

Scanning near-field optical microscopy (SNOM or NSOM) can reach a resolution of a sub-100 nm. The SNOM principle was first proposed by Edward H. Synge in 1928. His idea was later realized and demonstrated in the optical range by two scientists, Lewis et al in 1984 [24] and Pohl et al in 1984 [25]. The SNOM principle involves shifting the diffraction limit to a resolution of less than 100 nm. This occurs using a tiny light spot, with a diameter smaller than the excitation wavelength, to illuminate the surface of a specimen. Meanwhile the distance between probe and sample must not exceed the distance of the excitation wavelength. The subsequently formed evanescent waves provide detailed information about the investigated sample and the evanescent wave intensity decays exponentially as distance from the sample surface increases. Therefore the distance between the probe and the sample should be constantly maintained and should never exceed that of the excitation wavelength. The sample surface then is raster scanned by the probe and the image is reconstructed by collecting all points of optical signals [26,27].

There are three main SNOM configurations, aperture SNOM, apertureless SNOM and the scanning tunneling optical microscope (STOM) [28], also called the photon scanning tunneling optical microscope (PSTM) [29]. Aperture SNOM configuration uses an aperture probe to illuminate the sample surface and the detection signal is collected in the far field. The apartureless SNOM configuration uses a confined excitation beam which is then extremely focused on the top of a pointed probe tip. SNOM and PSTM are based on the principle of frustrated total internal reflection (FTIR). This technique works only with transparent samples. In general, SNOM is able to achieve a high resolution of up to 10-20 nm with a certain configuration in the visible range and the additional knowledge of the chemical information. However, SNOM is restricted in imaging as it can only investigate the surface of the sample and is unable to go any deeper. Moreover, the sample cannot be measured in buffer solutions and must be dry as the distance between the probe and the sample should

be maintained at a constant less than the excitation wavelength. Finally, the SNOM technique is a complicated one and is therefore slow in readout.

2.7.2 Total Internal Reflection Fluorescence Microscopy

Total internal reflection fluorescence microscopy (TIRF or TIRFM) is another technique in optical microscopy which provides high resolution images with very low background. TIRF is also a near field optical microscopy and its principle depends on the total internal reflection phenomena. If the excitation beam travels from a medium with a high index of refraction to a medium with a lower index of refraction, then the beam will be diffracted and transmitted. But, if the incident angle is higher than the critical angle, then the beam will be totally reflected back towards the high refractive index medium. As a result of this phenomenon, an evanescent field forms in a short range of 100 – 200 nm deep in the low refractive index medium. The penetration depth depends on incident angle, for as the angle of incident decreases, the penetration depth increases. However, the angle should be no less than the critical angle in order to maintain the total internal reflection effect. Usually in prism-less TIRF, high numerical aperture objectives are used to bend the excitation beam at an angle greater than the critical angle. The evanescent wave intensity decreases exponentially as the distance from the interface increases. Therefore, the fluorescence intensity also decreases as the distance from the interface decreases [30-32].

TIRF does not break the diffraction limit but it does provide a high signal to background ratio. TIRF is limited to the formed evanescent wave at the interface between two media. This fact prohibits optical sectioning at any plane of the sample, unlike the confocal microscopy. Thus the claim that TIRF breaks the diffraction limit in the axial axis is not entirely accurate.

2.7.3 Confocal Microscopy

The invention of confocal microscopy is credited to Marvin Minsky at Harvard University in 1961 [33]. The confocal microscopy main concept is to illuminate a specimen with a

focused beam spot and detect the fluorescence from the focal excitation volume through a pinhole placed in the exact image focus in the detection path. The sample is then raster-scanned in 3D and the image is reconstructed by recording the points one by one [34]. The pinhole ensure that just the fluorescence from the illuminated spot is passing throw the pinhole and any fluorescence coming out not from the focal volume will be blocked or suppressed by the pinhole in all dimensions. Decreasing the pinhole size leads to reject more out of focus light and thus improving the literal and the axial resolution. However the fluorescence intensity will also decrease as a function of the pinhole size. In 1980s the laser beam was introduced in microscopy and instead of moving the specimen in the confocal microscopy, the laser beam was scanned leading to a faster acquisition time and less instrumental artifacts. This development led to the production of confocal laser-scanning microscope (CLSM) [35]. In an ideal optical system and by using a visible laser beam with a suitable pinhole diameter the resultant detected spot is limited to Abbes diffraction limit. The literal resolution will be 200-300 nm and the axial resolution will be 500-1000 nm. The CLSM was convincing for the biological society, because such a microscope was able to achieve good resolution and thin clear optical sectioning using fluorescent markers without damaging the specimen[36]. CLSM improves resolution by a factor of 1.4 in comparison to a standard widefield microscope [21,37].

2.8 Beyond the Diffraction Limit

One way to increase the resolution is simply by using a shorter wavelength. According to Abbe's diffraction limit, the maximum achievable lateral resolution in light microscopy is ca. 200 nm and the axial resolution of is ca. 500 nm. Many techniques utilize this fact and helped to develop different approaches to break through the diffraction barrier. One example of a shorter wave length imaging system is the use of UV microscopy for detecting the Coumarin-120 single molecule by using a one photon excitation (OPE) wavelength of 350 nm and two photon excitation (TPE) wavelengths of 700 nm [38]. Yet there are very few fluorescent markers which can be used on living cells in the UV range. In addition, exposing living organisms or cells to UV light will ruin them. X-ray microscopy is applicable on wet and frozen samples and it can achieve a resolution up to 20 - 30 nm [39,40]. Electron mi-

croscopy (EM) was invented in 1920 by Ernst Ruska who used the de Broglie wavelength of electrons, located in the Angstrom regime, to break the diffraction limit[41]. However, there are two different EM techniques available, Transmission Electron Microscopy (TEM) and Scanning Electron Microscopy (SEM) and both are relatively expensive and technically demanding. For instance, TEM can be only used on thin samples or on surfaces and the sample preparation is very demanding. Because TEM works in a vacuum, the sample must be fixed, should be embedded in epoxy and then enriched with heavy metals for better contrast. Therefore TEM cannot be used for imaging live cells or organisms in their natural state, although it is widely used on structural biological samples and provides a superior resolution [5,42]. Other non-light microscopy techniques such as Atomic Force Microscopy (AFM), Scanning Tunneling Microscopy (STM) and Scanning Ion-Conductance Microscopy (SICM) are limited to imaging surfaces[3].

2.9 Overcoming the Diffraction Limit

All techniques previously mentioned are still imperfect when it comes to providing a super resolution image for the interior of a living cell in the visible range. The challenge is not just to improve the resolution of fluorescence light microscopy as with the SNOM, CLSM and TIRF or to surpass the diffraction barrier in non-light microscopy as with the AFM, TEM and STM. The challenge is to overcome the diffraction limit in florescence light microscopy, which would provide a super resolution tool for investigating living cells constituents.

2.9.1 Stimulated Emission Depletion Microscopy

In 1994 Stephan Hell and Jan Wichmann introduced the theoretical concept of stimulated emission depletion (STED) microscopy [16] and later in 1999 was implemented by Thomas Klar and Stefan Hell [43]. STED is the first fluorescent optical microscope technique, which was able to overcome Abbes lateral resolution diffraction limit. In STED a second laser is needed beside the excitation laser to suppress the fluorescence emission from the surrounding fluorophores of the excited focal spot. The suppression process is

done by what is called stimulated emission, where the excited state of the fluorophores stimulated with a photon possess an energy matches the energy gap between the excited state and the ground state. STED beam has a doughnut shaped pattern which provides zero intensity in the center of the focal spot. An overlap between the excitation focal spot and the saturated depletion STED pattern produce the effective PSF.

In practice, a pulsed laser beam with low power intensity is focused on a sample spot to excite fluorophores from the ground state S_0 to the first excited state S_1. A second STED laser pulse, with a wavelength longer than the excited beam wavelength and a pulse width within the range of 50-300 ps, is formed into a doughnut shaped. This then works to deplete fluorescence at the periphery of the excited spot. The depleted population has a nonlinear dependence on the STED beam intensity. Thus, if the STED beam is applied at high intensity, exceeding the saturation level of depletion at the periphery, then all fluorescence light coming from this region will be suppressed. The spot center will remain largely unaffected by the STED beam and therefore, the fluorescence signal will be detected from a very small region in the center. This process helps sharpen the effective PSF and to overcome the diffraction limit. The effective PSF or the resolution can be described in the following equation:

$$\delta \approx \frac{\Delta}{\sqrt{1 + \frac{I_{dep}}{I_{sat}}}} \tag{2.6}$$

where δ is the resolution, Δ is the PSF of the diffraction-limited size of the focal spot, I_{dep} is the peak intensity of the depletion laser and $I_{sat}$is the saturation intensity for the fluorophores. The STED microscope has reached a resolution of 6 nm by imaging fluorescent defects in a diamond[44], a resolution of 20 nm by using organic dyes and a resolution of 50-70 nm using fluorescent proteins[10,11,14].

2.9.2 Saturated structured illumination microscopy (SIM)

The working principle of SIM is similar to STED with both techniques using a pattern to improve the resolution. However, the SIM technique involves a positive sinusoidal excitation pattern which is applied and formed by interfering two beams. The multiplication of both patterns results in a beat pattern (moiré fringes). The resulting illumination pattern contains a small number of spatial frequencies that are then translated to the detector. The investigated sample is subsequently scanned by phase shifting and rotating the illumination pattern (Gustafsson, 2000; Heintzmann and Cremer, 1999). A final image is reconstructed from multiple scanned images. The spatial modulation information generated with the illumination pattern is used to improve the resolution of the reconstructed image to approximately 100 nm. The advantage of SIM is that it can be applied on any fluorescence marker that is suitable for fluorescence microscopy. The reason for this is that SIM does not depend on the fluorescence marker's photophysical properties, but rather on the information obtained from the excitation beam pattern. SIM can be combined with either multi-color imaging or two-photon imaging and many other imaging techniques [45-47].

2.9.3 Photoswitchable localization Microscopy

Two similar techniques in nanoscopy were introduced in 2006 by Xiaowei Zhuang for STORM [17], Eric Betzig for PALM [7] and Samuel T. Hess for FPALM [8]. All are based on single molecule, high precision localization microscopy. Michael J. Rust used photoswitchable fluorophores that can be switched on (fluorescing or on state) or off (non-fluorescing or off state) using a beam of two different wavelengths. One beam excites the single fluorescent molecule and simultaneously puts the single molecule in a stable off-state. A second beam with a different wavelength can reactivate the fluorescence molecule when the secondary fluorescence markers are near to the main fluorescence markers. This method was named stochastic optical reconstruction microscopy (STORM). The accuracy of STORM depends on the number of switchable cycles. A number of fluorescing single molecules per cycle are accurately localized and by repeating the localization process for

multiple cycles, a subdiffractional image can be reconstructed with a resolution of ca. 20 nm.

The photoactivated localization microscopy (PALM) technique is very similar to STORM, the only difference being the type of fluorescent samples used in demonstrating each approach. STORM uses cyanine dyes, Cy3-Cy5 pair to switch Cy5 on and off in the presence of Cy3. Alternatively, PALM uses photoactivatable green fluorescent protein (PA-GFP), which is activated by illumination with 405 nm laser beam. A higher wavelength laser beam is used to excite PA-GFP and the fluorescence is detected with a CCD camera. After excitation, PA-GFP reaches a reversible dark state or photo-bleached state. Both the rate of activation and the rate of photo-bleaching are controlled by their respective intensities. The number of activated PA-GFPs can be controlled by changing the intensities of activation and excitation.

The resolution of STORM and PALM techniques is limited by the detection of photon-counts per photoactivation cycle. Cy3-Cy5 pairs and PA-GFP require several thousand photoactivation cycles and several hundred photoactivation cycles respectively. This technique depends on the fluorescence labelling densities and on the structure of the specimen. An increase in the number of detected photons increases the localization precision. Therefore, the image resolution is limited to how accurately each fluorescent marker is localized. In the same manner, when the labelling density is low and the temporal fluctuations of neighboring pixels are distinguishable, a correlation analysis of the temporal fluctuations of each pixel can result in an improved image resolution [14,48,49].

3 Methods and Sample Preparation

3.1 Polarization Modulation Setup

The Polarization Demodulation setup was designed with different Laser systems to provide a wide range of wavelengths used for different methods of sample excitation. The Setup was constructed with a constant wave Sapphire 488-50 laser (CW-488-50, Coherent, Dieburg, Germany) which can provide a single wavelength at 488 nm (Figure 3-1). The Polarization Demodulation setup was also constructed with the Chameleon Ultra II (680 nm - 1080 nm, Coherent, Dieburg, Germany) for the use in two-photon excitation (TPE) imaging and for the use of pumping the optical parametric oscillator (OPO- PP-Automatic VIS., Angewandte Physik & Elektronik, A.P.E., Berlin, Germany). Chameleon Ultra II has a high output power of up to >4.0 W at 800 nm which can be used to pump simultaneously second optical parametric oscillator (OPO- PP-Automatic IR., Angewandte Physik & Elektronik, A.P.E., Berlin, Germany). This is achieved by using an achromatic half-wave plate (AHWP05M-980, Thorlab, Dachau/Munich, Germany) followed by a high energy broadband polarizing cube (PBS1005-SBB, 400-1100 n, RS >99.9%, T_P >97%, Boulder, CO, USA) to split the beam. The splitting ratio is adjusted by rotating the half waveplate. These lasers systems were used as light sources for the setup and the paths of the different laser beams were combined and aligned towards the microscope's objective using dichroic mirrors. The first dichroic mirror (DM1: Laser beamsplitter z 568 sprdc, AHF analysentechnik, Tuebingen, Germany) was used to combine the CW Sapphire 488 nm laser with the OPO visible laser beam up 570 nm. A second dichroic mirror (DM2: 2/3P-Laser beamsplitter spxr-1500, AHF analysentechnik, Tuebingen, Germany) was used to combine the visible laser, either from the Sapphire-488 laser, or from the OPO PP Vis. system or from both, with the Infra-red beam produced by the Chameleon Ultra II (680 nm-1080nm) or by the OPO-PP IR (1000 nm – 1600 nm). A third dichroic mirror was used in the body of the microscope to reflect the excitation beam towards the back aperture of the microscope's objective (NA = 1.35 oil immersion, UPlanSApo, 60x, Olympus, Hamburg, Germany). The third dichroic mirror is built into the microscope's rotating wheel and it was therefore possi-

ble to switch between three different dichroic mirrors depending on the excitation wavelength. The first dichroic mirror 3* (DM3-1: Laser beamsplitter z 488 RDC, AHF analysentechnik, Tuebingen, Germany) was used to reflect 488 nm excitation laser beam and transmit emissions greater than 500 nm. The second dichroic mirror 3* (DM3-2: dual line beamsplitter zt 488/594 RDC, AHF analysentechnik, Tuebingen, Germany) was used to reflect 488 nm and 590 nm excitation laser beams and transmit emissions in the range

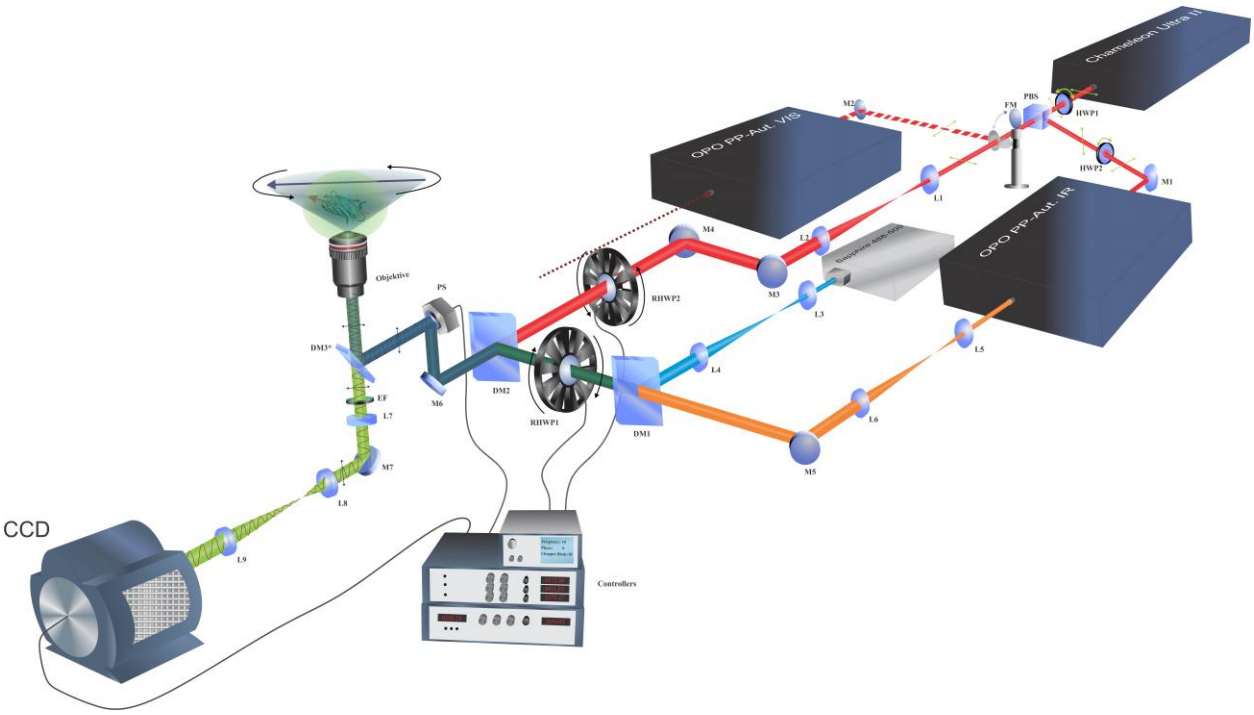

Figure 3-1: Schematic illustration of all The Polarization Demodulation setups combined together.

of 500-570 nm. The third dichroic mirror 3* (DM3-3: 2/3P-Laser beamsplitter spxr-1500, AHF analysentechnik, Tuebingen, Germany) was used to reflect two-photon excitation wavelengths greater than 700 nm and transmit emission wavelengths less than 700 nm. The emission was detected with an electron multiplying, charged-coupled device, back illuminated (iXon 897 EMCCD BV, Andor, Belfast, UK). Depending on the excitation and emission wavelengths, suitable emission filters were used. Some optical parts were added or removed depending on the measuring conditions. A body microscope IX71 (Olympus,

Hamburg, Germany) was used in the setup as it included the objective, the DM3*, a microscope collimating lens (L7) and a mirror (M7).

3.1.1 Polarization Demodulation Setup with Sapphire 488-50 laser

The first polarization modulation setup was aligned with a CW sapphire 488-50 laser (Figure 3-2). The 488 nm laser beam has a diameter of 0.7 mm and it is linearly polarized. The laser beam was expanded to 10 times its diameter using a telescope to ensure a good light interaction with the waveplate. The telescope was combined of two achromatic lenses, the first achromatic lens L1 (Achromatic Doublet, f=30 mm, Thorlab, Dachau/Munich, Germany) and the second achromatic lens L2 (Achromatic Doublet, f=300 mm, Thorlab, Dachau/Munich, Germany) An achromatic half wave plate (AHWP05M-600, 400 – 800 nm, Thorlab, Dachau/Munich, Germany) was built into a rotatable chopper blade (MC1F10, Thorlab, Dachau/Munich, Germany). The rotation speed of the chopper blade with the half waveplate (frequency) was controlled by an optical chopper system and chopper wheel (MC2000, Thorlab, Dachau/Munich, Germany) and synchronized with the EMCCD camera frame rate. The setup was at first constructed with two achromatic quarter waveplates (AQWP05M-600, Thorlab, Dachau/Munich, Germany) aligned one behind the other. The first quarter waveplate was fixed with an angle of 45° to the fast axis in order to convert the linear polarized light to a circular polarized light. The rotation of the second quarter waveplate was synchronized with the EMCCD camera frame rate. The advantage of this construction is that when the linear polarized light is rotated with the quarter waveplate, the intensity variation is around 50% less than when rotated with the half waveplate. The second quarter waveplate has to rotate 180° to complete the 180° rotation of the linear polarized beam. On the other hand, a 90° rotation of the half-wave plate is needed to complete the 180° rotation of the linear polarized beam. The advantage of using two quarter waveplates is that it results in less intensity variation during rotation. The disadvantage however is that it requires the alignment of two quarter waveplates instead of just the one half waveplate.

The collimated beam was focused on the back aperture of the microscope's objective using an achromatic lens L10* (Achromatic Doublet, f=500 mm, Thorlab, Dachau/Munich, Germany). The excitation beam was then reflected by the dichroic mirror D3-1 towards the microscope's objective. The excitation beam covered the entire field of view of the sample (wide-field). The emission was then passed through the dichroic mirror DM3-1 and collimated with the microscopic lens L7. One or two emission filters (ET Bandpass 525/50, AHF analysentechnik, and Brightline HC 525/30, Tuebingen, Germany) were used in the detection path. The detected image size was adjusted using a telescope of two achromatic lenses (L8 and L9 f=depends on the magnification needed, Achromatic Doublet Thorlab, Dachau/Munich, Germany). The EMCCD camera was used for all setup detections.

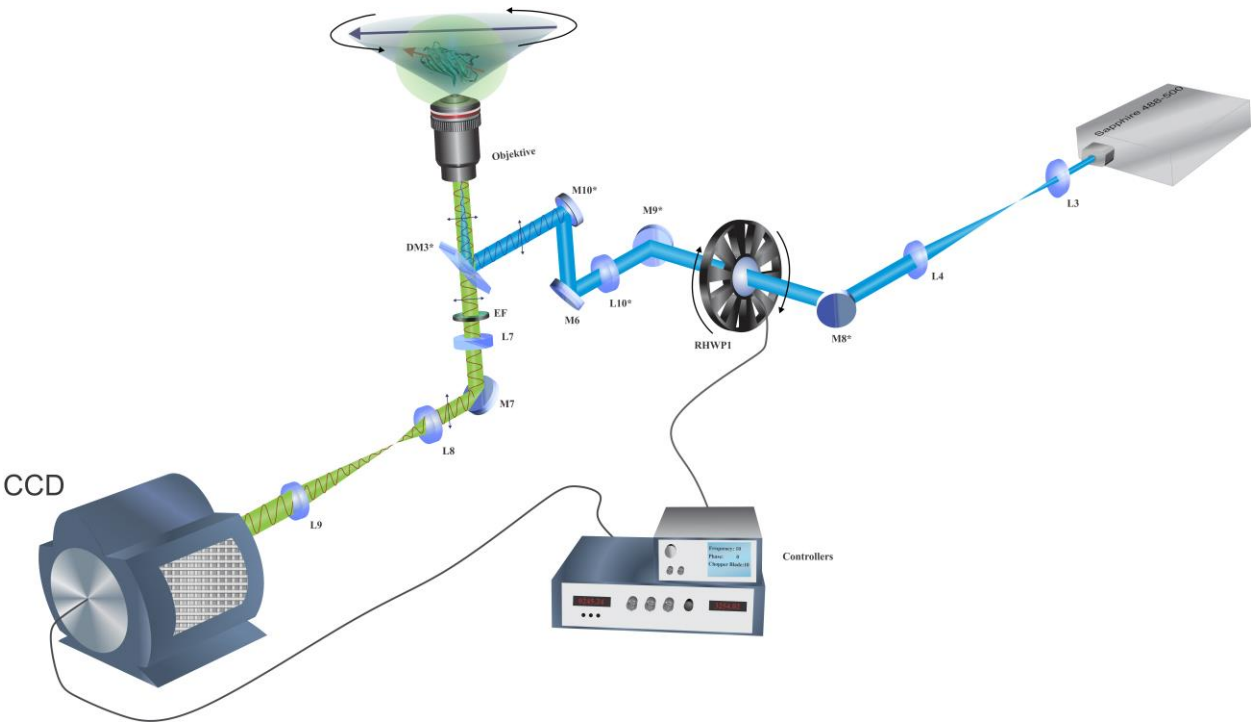

Figure 3-2: The Polarization Demodulation setup setup with Sapphire 488-50 laser.

3.1.2 Combination of Two Photon Excitation Imaging

For the two-photon excitation (TPE) experiments linear polarized light from a pulsed laser (740 nm , 80 MHz, Cameleon, Coherent) is used in combination with set-up one. After beam expansion by a telescope system the linear polarized beam passes a rotating half-wave Plate whose rotation is achieved the same way as described for the OPE path of the 488 nm set-up. The collimated linear polarized light continues through a diffractive optical element (DOE) (MS-225-M-Y-A, 9x9 spots, Laser Components) before a forth telescope system couples the structured beam into the microscope using a dichroic mirror and a high-dynamics Piezo Mirror (S-334.1SL, Physik Instrumente).

For image acquisition with TPE, the high-Dynamics Piezo Mirror is used to scan the sample with a 9x9 pattern of illumination (Figure 4-38). The camera frame frequency remains at 30 Hz and triggers the Piezo Mirror to start scanning at a speed of 120 Hz. This results in four

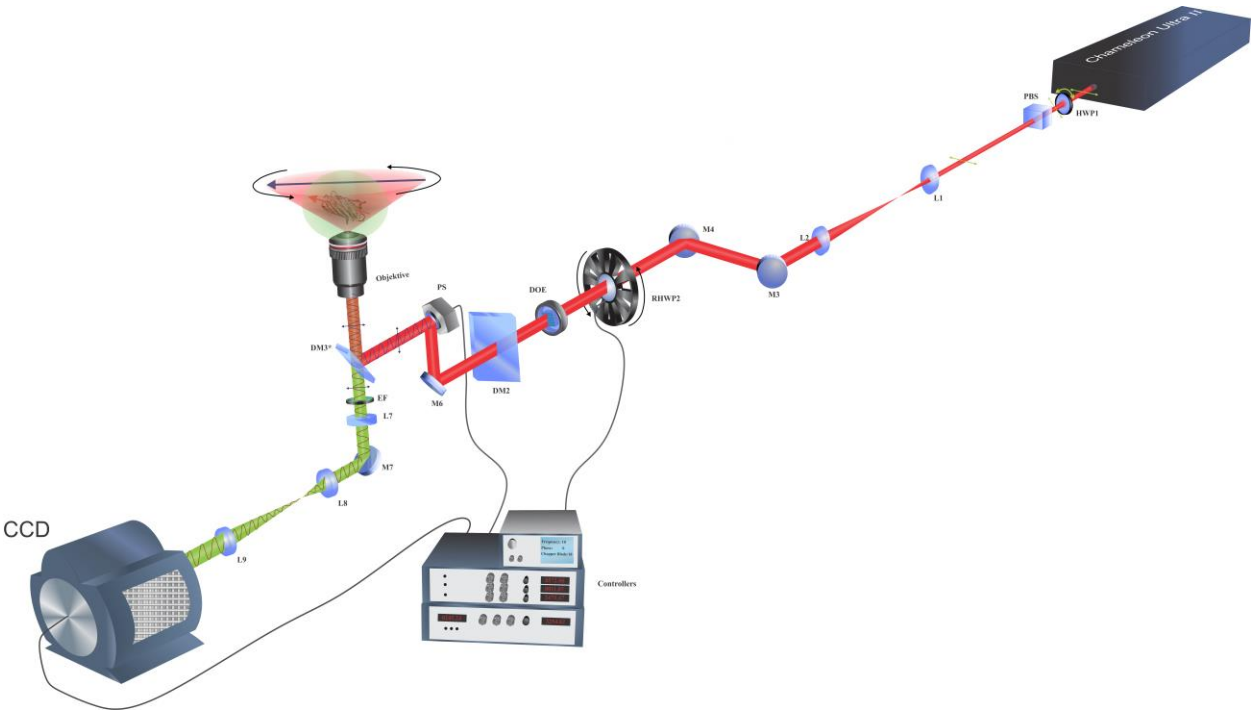

Figure 3-3: Two Photon excitation with Polarization Demodulation setup.

mirror positions that are recorded in one frame. When the 9x9 pattern has completed one full cycle (4 positions per frame), the illuminated area in the field of view has then a homogeneous square shape. The step size of the x and y direction of the scanning mirror is adjusted, so that when the 9x9 structure is moved two steps in x and y directions, The 9x9 pattern will become then a homogenous square shaped of TPE in the field of view.

3.1.3 Polarization splitting in detection path

For the detection path, additional components were added to the setup in order to split fluorescent light into two components. When excited with linearly polarized light, the emitted fluorescent light is also linearly polarized light. The Dielectric Polarizing beam splitter (DE-

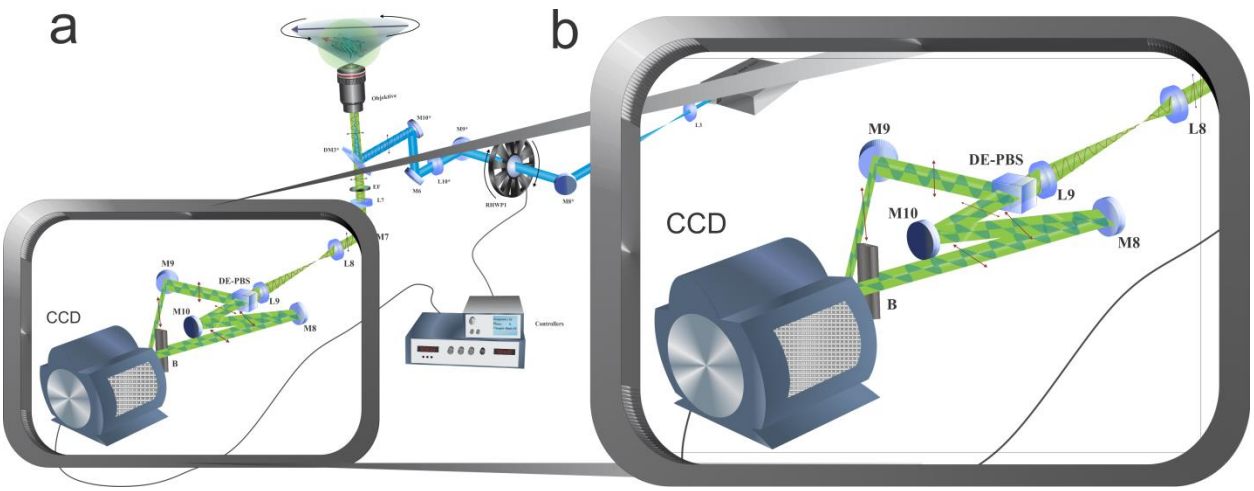

Figure 3-4: Polarized light splitting components added to the setup with Sapphire 488-50 laser (a). Zoom in on the components used for polarized fluorescent light splitting (b).

PBS, PTW20, B-Halle, Germany) was used in the detection path to split the linearly polarized fluorescent light into two components; polarized fluorescent light parallel to the plane of incidence and polarized fluorescent light perpendicular to the plane of incidence. The parallel light component was transmitted with 97-98% efficiency and the perpendicular light component was reflected with 99.9% efficiency. The transmitted component from the beam splitter cube was redirected to the EMCCD camera using two broadband dielectric mirrors

(M8 & M10, BB1-E02, Thorlab, USA). Similarly, the reflected component from the beam splitter cube was also redirected to the EMCCD camera, except this time using just one broadband dielectric mirror (M9, BB1-E02, Thorlab, USA). The path length from the polarizing beam splitter cube to the EMMCD camera must be the same for both components. Likewise, the reflection angles from M8 and M9 towards the EMCCD camera must remain close to one another so that images do not deviate. Both components were detected on the EMCCD camera by locating the polarized fluorescent light on the camera chip, as well as the perpendicular component on the right side of the camera chip and the parallel component on the left side of the camera chip. The two detected parts on the EMCCD camera chip was distinguished simply by using a 1 x 10 cm metal block (Figure 3-4**b**) fixed on a stage for generating a dark line on the EMCCD chip between the two components (blocking light). The image was then flipped 90° when opened or viewed with the software (figure 3.4).

3.2 Samples and sample preparation

3.2.1 Preparation of single molecule samples

10 µL of 100 pM Alexa Fluor® 488 (Invitrogen, Darmstadt, Germany) hydrazide solution (in Milli-Q water) was spin coated on a 18 x 18 mm cover slip Nr. 1 (Gerhard Menzel, Braunschweig, Germany). The cover slip was left for at least 10 minutes to dry and so that the single molecules were homogeneously distributed and fixed with a certain orientation on the cover slip.

3.2.2 Preparation of fixed nerve cell samples

The samples were provided by Prof. Dr. Martin Korte and Dr. Marta Zagrebelsky Holz from the cellular neurobiology department, Technical University of Braunschweig. Primary hippocampal cultures were prepared from C57Bl／6 mice (embryonic day E18). The tissue was incubated for 30 minutes in trypsin–EDTA at 37°C, and then mechanically dissociated. Cells were plated at high density (70.000 per coverslip) on poly (l-lysine)-coated coverslips

(13 mm) and kept in a Neurobasal medium (Gibco) supplemented with 2% B27 (Gibco) and 0.5 mM Glutamax with 5% CO2, 99% humidity and a temperature of 37°C [50]. Primary cultures of hippocampal neurons were transfected at 14 DIV with Lipofectamine2000, following the manufacturer's instructions. To visualize neuronal morphology in detail, either a membrane targeted form of enhanced green fluorescent protein (eGFP) (farnesylated form of eGFP; feGFP) or a construct expressing LifeAct-eGFP [51] were used to label the actin cytoskeleton. Two to four days after transfection, the cells were fixed with 4% PFA in Phosphate buffer, washed and mounted in aqueous anti-fading medium (Biomeda, CA, USA).

3.2.3 Preparation of Giant Unilamellar Vesicles (GUVs)

In cooperation with Professor Dr. Claudia Steinem laboratories (Institute of Organic and Biomolecular Chemistry, Georg-August-Universität Göttingen, Germany), Ole M. Schütte prepared the Giant unilamellar vesicles (GUVs) samples. GUVs were prepared according to the electroformation technique [52]. DOPC (Avanti Polar Lipids), sphingomyelin (Sigma Aldrich), cholesterol (in CHCl3) (Sigma Aldrich), a galactosphingolipid (in CHCl3/MeOH (2:1)) and TexasRed-DHPE (in CHCl3/MeOH (4:1)) (Santa Cruz Biotechnology) were mixed in a molar ratio of 39.5:30:20:10:0.5 yielding a total concentration of 1.5 mg/mL. Following this, 25 µL of the mixture was deposited on indium tin oxide (ITO) coated cover slips. The cover slip was placed under a vacuum at 55 °C for 3 hours to eliminate the solvent. An AC electric field of 1.6 V, 12 Hz was applied for 3 hours at 55 °C in a 0.3 M sucrose solution in ultrapure water. Under these conditions, GUVs with two different types of domains and diameters of several µm were formed [53,54]. 20 µl of the GUVs sample was diluted with 580 µl of 0.01 M PBS in a lab-Tek Chambered Coverslip. After 30 minutes the GUVs were settled on the bottom of the Lab-Tek chambered coverslip.

3.2.4 Preparation of F-actin polymer on surface

G-actin was purified from rabbit skeletal muscle in 99% purity (AKL99-A; Cytoskeleton, Inc., Denver, CO). The G-actin was delivered as a lyophilized protein. One vial of G-actin

protein containing 250 µg was resuspended to 1 mg/ml with 250 µl of General Actin Buffer (BSA01; Cytoskeleton, Inc., Denver, CO) supplemented with 0.2 mM ATP (New England Biolabs Inc., Ipswich, MA) and 1.0 mM DTT (Carl Roth, Karlsruhe, Germany). The mixture was mixed and left on ice for one hour.

General actin buffer was also delivered as lyophilized powder in tube. It was prepared by re-suspending it in 10 ml Milli-Q water, to create a 1x strength buffer containing 5 mM Tris-HCl pH 8.0 and 0.2 mM calcium chloride. 10 µL of 100 mM ATP was added to 90 µL of 1x General Actin buffer. The final concentration was 10 mM ATP. After this, 1M of DTT (1, 4-Dithiothreitol) was prepared with Milli-Q water. 5 µL of the DTT stock solution was added to 95 µL of 1x General Actin buffer to obtain 50 mM. Subsequently, 10 µL of 10 mM ATP and 10 µL of 50 mM DTT were added to 480 µL of 1x General Actin buffer. The result was 500 µL of 1x General Actin buffer supplemented with 0.2 mM ATP and 1.0 mM DTT.

Actin polymerization buffer was delivered as lyophilized powder in tube and it was resuspended in 2 mL of 100 mM Tris HCl pH 7.5 to create a 10X strength buffer containing 100 mM Tris HCl, 20 mM $MgCl_2$, 500 mM KCl, 10 mM ATP and 50 mM guanidine carbonate with a pH of7.5. 45 µL of the 1 mg/ml resuspended G-actin was mixed with 5 µL of 10X Actin polymerization buffer and the mixture was left for one hour in room temperature to polymerize.

ATTO 590 Phalloidin (ATTO-TEC, Siegen, Germany) was used as a fluorescent dye for labelling the F-actin. 10 nmol of ATTO 590 Phalloidin was diluted with 1.5 ml Methanol to get a concentration of 6.67 µM. 50 µL of 10 x polymerization buffer and 5.5 µL of 6.667 µM ATTO 590 Phalloidin were added to 450 µL of milli-Q water. The result was a 1x Polymerization Buffer containing ~70 nM Atto 590 Phalloidin. This solution was used to dilute the polymerized F-actin to 100 fold. 10 µL of the labeled actin filaments solution was spotted onto a microscope coverslip and allowed to spread. Exactly 15 µL of ProLong® Gold Antifade Mountant (Life Technologies**,** Darmstadt, Germany) was then spotted onto the center of the coverslip. Anti-fade mounting media is very important for protecting dyes from photo-

bleaching and for preventing the sample on the coverslip from drying and thus becoming degraded. The sample can then be used for many days.

Before measuring the sample, the sample should be positioned on the coverslip in the same place as the spot of Anti-fade. The sample was measured using the Polarization Demodulation setup (SPoD) microscope with an OPO pulsed laser of 568 nm wavelength and a 15 frame per period modulation speed. For detection, 600 nm longpass and 650/40 nm bandpass filters were used in the detection path (see Figure 3-1). The pixel size was equal to 26.8 nm.

4 Results

4.1.1 Polarization Demodulation

The Polarization Modulation technique was first applied to different types of single fluorescent molecules. For instance, Alexa Fluor® 488 hydrazide was used in the very beginning of the investigation into the Polarization Demodulation technique. Single fluorescent molecules were distributed randomly on a coverslip and their dipole moment orientation was therefore random oriented. The sample concentration was prepared within the pico molar range so that the single fluorescent molecules had a low density on the cover slip. A

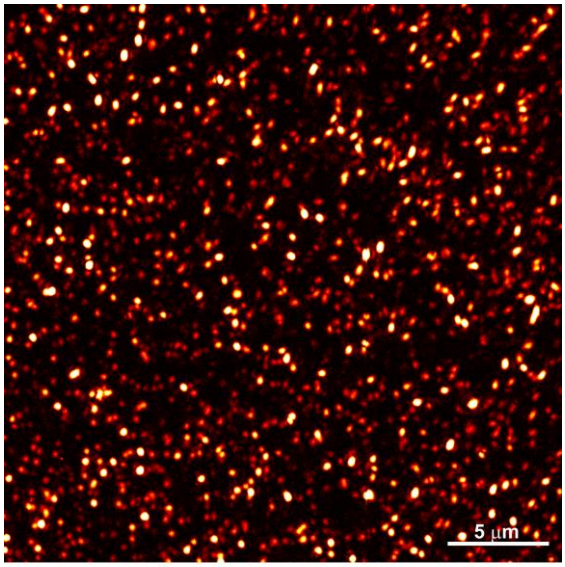

Figure 4-1: Diffraction limited image of Alexa Fluor® 488 hydrazide molecules randomly oriented and fixed on cover slip. The measured sample has a low density of fluorescent dye.

diffraction limited image of the investigated sample is demonstrated in Figure 4-1. The set-up with sapphire 488-50 laser (Figure 3-2) was used to investigate the possibility of modulating randomly oriented single fluorescent molecules and fixing them on a cover slip. One single fluorescent molecule is expected to have a sinusoidal-squared wave. This sinusoidal

wave is synchronized with the rotation angle of the linear polarized light. When the linear polarized light rotates and stands parallel to the dipole moment orientation of the fluorescent molecule, the detected emission will be at its maximum. Following this, the detected emission will be therefore at its minimum when the linear polarized light rotates to stand perpendicular to the dipole moment orientation of the fluorescent molecule. The first experiment demonstrated that single molecules fixed on coverslips can show modulation when rotating the linear polarized light. The single molecules' dipole moments were randomly oriented and therefore, the single molecules were statistically expected to display different phases of the modulation signals.

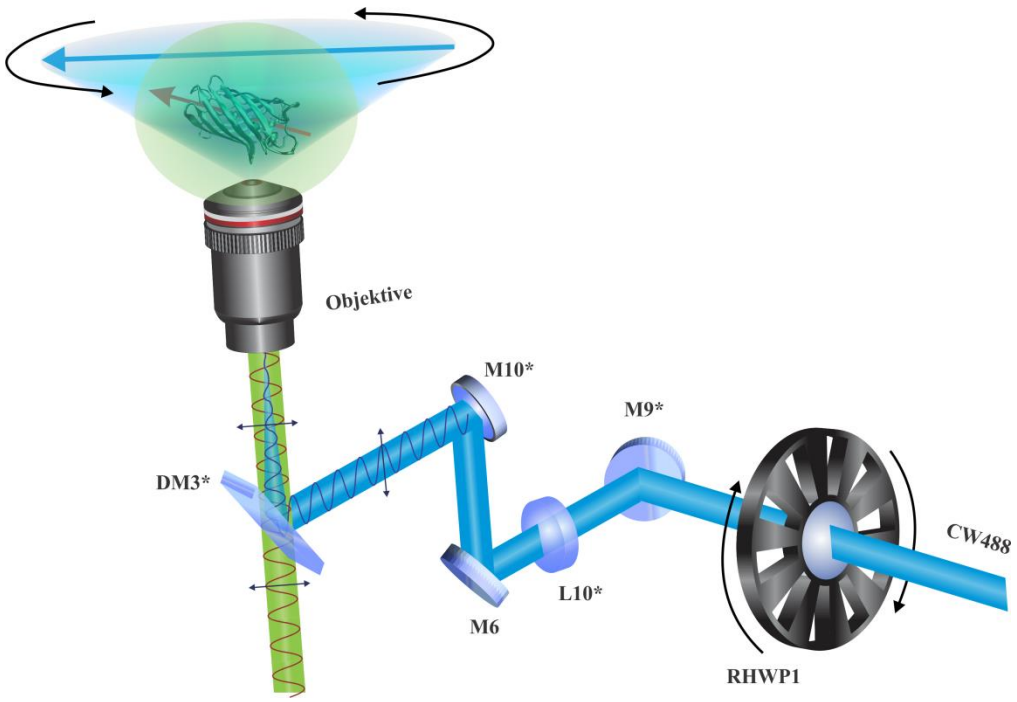

Figure 4-2: The linear polarized beam is rotated by a rotatable half waveplate at a constant frequency and the EGFP has a fixed transition dipole moment (refer to Figure 3-2 for more details).

As previously mentioned, the plane of linear polarized light should be parallel to the transition dipole moment of the fluorescent molecule in order to achieve maximum excitation and thus maximum fluorescence. The angle between the plan of linear polarized light and the transition dipole moment is noted as α. The transition dipole moment orientation of a mole-

cule, which is fixed to a surface, is oriented in three dimensions. The projection of the transition dipole moment on two dimensions (x and y – axes) is considered because the plane of the linear polarized light is rotating on two dimensions (x and y – axes). Figure 4-4 demonstrates, for example, an enhanced green fluorescence protein (EGFP) whose transition dipole moment is represented with a red arrow in three dimensions. The blue arrow

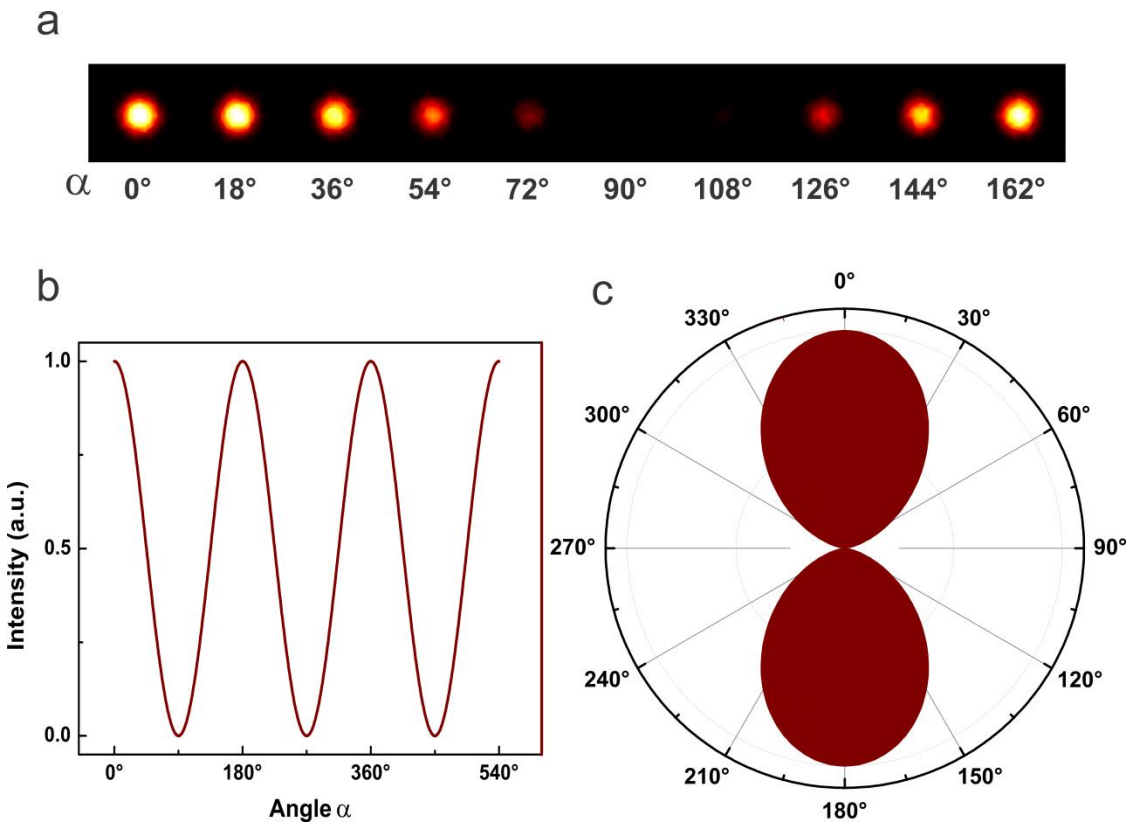

Figure 4-3: Simulated emission of a single fluorescent molecule demonstrates that its florescent intensity depends on the excitation polarization angle (a). The emission cosine square wave, present for three period rotations of the excitation beam, depends on the excitation angle α (b). The polar plot shows the range of polarization angles. This results in effective excitation. Any molecule possessing a dipole moment within this angle range will be excited with maximum fluorescence at $\alpha = \mathbf{0}°$ (c).

demonstrates the orientation of the plane of linear polarized light. The excitation beam is rotated using the rotatable half waveplate. The EGFP will therefore be at maximum excita-

tion when the linearly polarized excitation beam is in a position parallel to the transition dipole moment of the EGFP (i.e. $\alpha = 0°, 180°$) (Figure 3-2). The rotation of the linear polarized excitation light results in a cosine-squared function emission signal (Figure 4-3 **b**). The signal is at its maximum when the polarized beam and the dipole moment are parallel to each other (i.e. $\alpha = 0°, 180°$). Similarly, the signal is at a minimum when the polarized beam and the transition dipole moment are perpendicular to each other (i.e. $\alpha = 90°, 270°$) (Figure 4-3 **a**). The angle range of excitation for a fixed molecule with a certain dipole moment orientation is around ~70° (from ~35°- ~325°) as shown in Figure 4-3 (**c**).

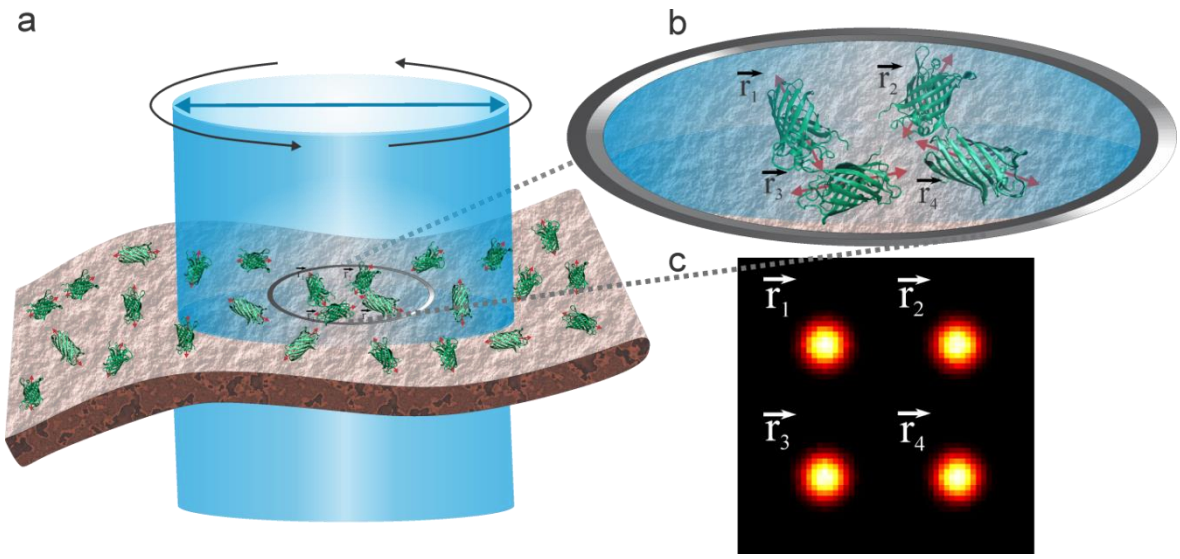

Figure 4-4: Schematic illustration of a labeled biological sample with EGFP molecules demonstrating different dipole moment orientations (red arrows) and a rotating linearly polarized light (blue arrow) (a). An inset of the focal area showing four EGFP molecules with different dipole moment orientations noted with $\vec{r_1}, \vec{r_2}, \vec{r_3}$ ***and*** $\vec{r_4}$ (b). Simulated averaged stacks image of the four EGFP molecules when the emission was detected on a CCD camera (c).

Fluorescent markers are usually labeled or tagged to a surface or to specimen randomly. The concentration of the markers can be controlled, however it is difficult to control the orientation of the markers. Supposing that we used the SPoD technique to investigate a sample labeled with a low concentration of EGFP, EGFP's molecules are expected to have different dipole moment orientations (Figure 4-4 **a** and **b**).

The excitation beam is linearly polarized and it excites the EGFP molecules in the focal area. The emission is then detected by a CCD camera (Figure 4-4 **c**). By focusing on only four EGFP molecules and detecting their individual fluorescence, different signals can be detected. The fluorescence intensity of an immobilized fluorescent molecule is proportional to the cosine-squared of the angle α (4.1).

$$I_{Fl} \propto \cos^2 \alpha \qquad 4.1)$$

These four EGFP molecules have different dipole moment orientations as illustrated in Figure 4-4 **b**. Therefore, these molecules fluoresce just when the dipole moment orientations of the EGFP molecules are in the excitation angle range α**.**

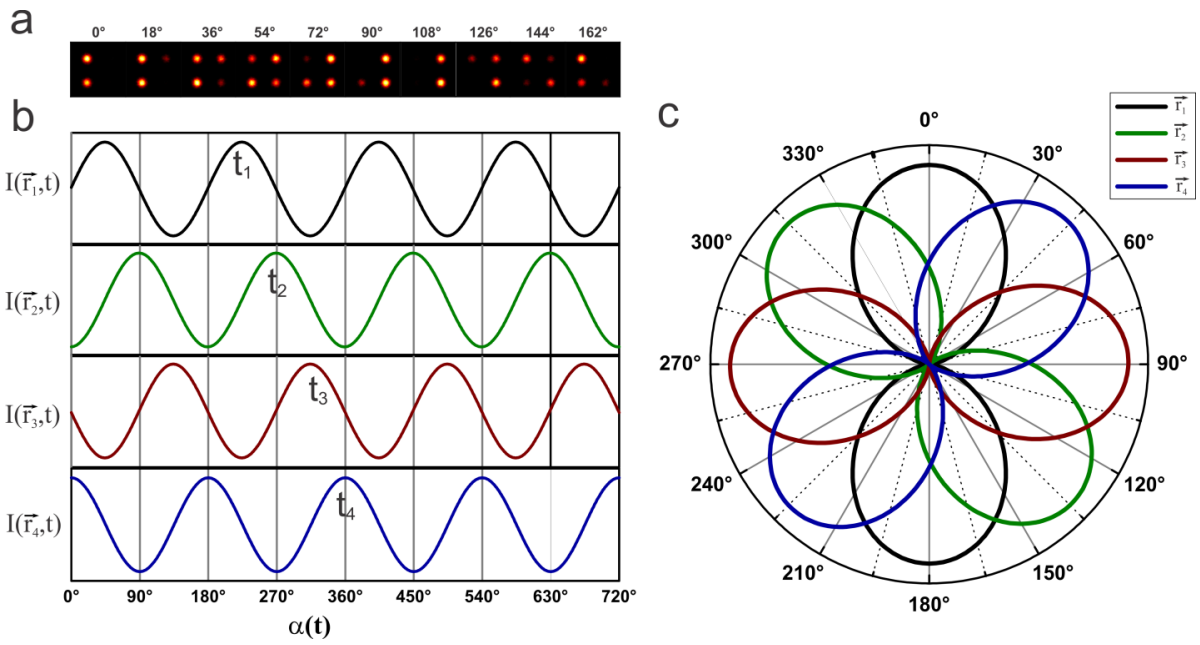

Figure 4-5: The four EGFP molecules of different molecular orientations are illustrated when excited by the rotating linear polarized light. Simulation of ten frames with 18° step of rotation of the linear polarized light rotation demonstrates different fluorescence intensities of four fluorescent markers per time-frame (a). Fluorescence intensity of four fluorescent markers ($\vec{r_1}, \vec{r_2}, \vec{r_3}$ and $\vec{r_4}$) showing cosine-squared functions that differ in their phases (t_1, t_2, t_3 and t_4) (b). The effective excitation angle range of the four differently oriented fluorescent molecules with a phase shift of 45° between each frequency illustrated in black, blue, red and green polar curves (c).

While rotating the linearly polarized excitation beam, the EGFP molecules will start fluorescing (blinking) in different time frames. The four EGFP molecules possess a different fluorescence intensity at a certain time (frame) or at a certain angle of rotation of the polarized excitation light (Figure 4-5 a). All single fluoresce EGFP molecules will show a cosine-squared signal with their fluorescence intensity. The difference in these signals, in this

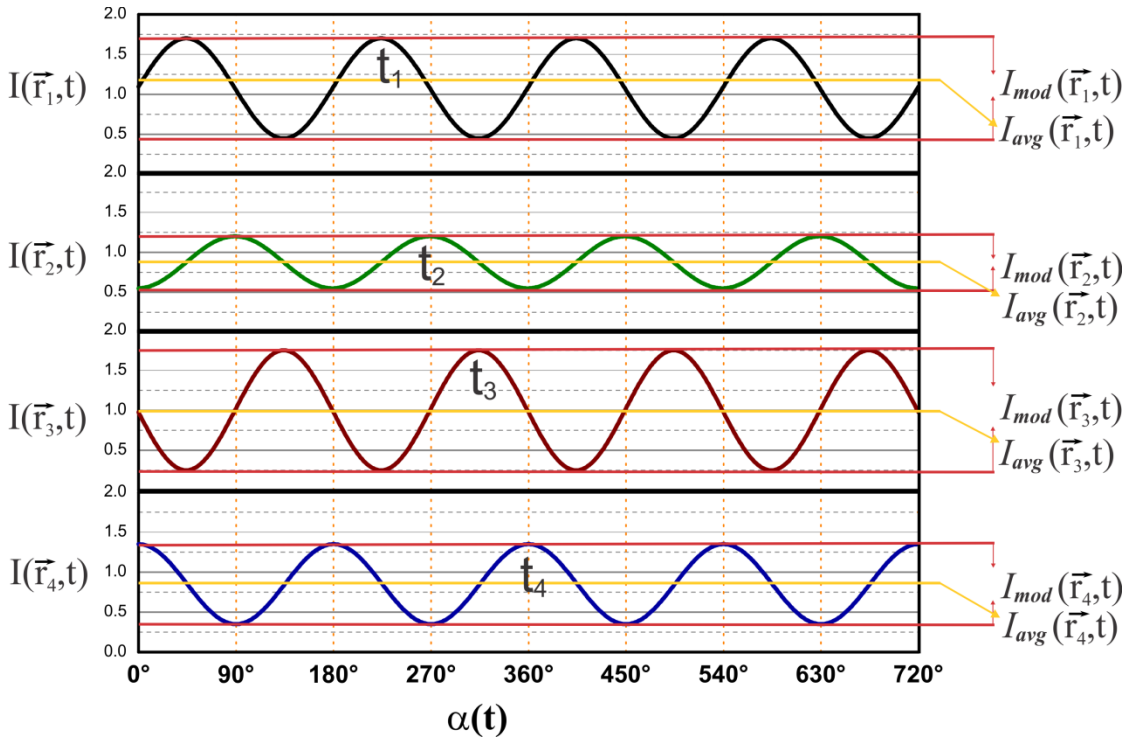

Figure 4-6: Four signals from four fluorescent markers are having different phases (t_1, t_2, t_3 and t_4) and also different modulation intensity ($\boldsymbol{I_{mod}(\vec{r_1}, t)}$, $\boldsymbol{I_{mod}(\vec{r_2}, t)}$, $\boldsymbol{I_{mod}(\vec{r_3}, t)}$ ***and*** $\boldsymbol{I_{mod}(\vec{r_4}, t)}$) and finally different average modulation intensity ($\boldsymbol{I_{avg}(\vec{r_1}, t)}$, $\boldsymbol{I_{avg}(\vec{r_2}, t)}$, $\boldsymbol{I_{avg}(\vec{r_3}, t)}$ ***and*** $\boldsymbol{I_{avg}(\vec{r_4}, t)}$).

instance, is the phase (Figure 4-5 b). The maximum intensity of the first EGFP molecule is not overlapping the second, the third or the fourth EGFP molecules (Figure 4-5 **c**). The phase shift between these four molecules is 45° as illustrated in the polar plot (Figure 4-5 **c**). Using these data, fluorescent markers can be distinguished by their dipole moment orientations distinctions. There are also parameters which can be also an addition to the dipole moment orientations information.

Fluorescent markers vary in their absolute fluorescence intensities for the same type of fluorescent markers as well as for different types of fluorescent markers. The variations in fluorescence intensities results in different modulation intensities I_{mod}. The reason is that fluorescent markers for the same type don't possess exactly the same quantum yield of emission. Furthermore, the fluorescent molecules wobble, whether they are labelled or put on a surface, and therefore the all over orientation differs. The background or the offset of each signal (from one pixel) on the CCD camera can be also different. The background or the offset is then neglected when only the average modulation intensity I_{avg} is considers. If two modulated signals would have the same intensity the average will not necessarily be the same because the modulation amplitude is different (Figure 4-6).

4.1.2 Pixel calibration

The microscope objective works to provide a highly focused light on a sample. Depending on its numerical aperture value, the image will be magnified in a certain factor. Should the image requires further magnification, a telescope in the detection path may also be used, as shown in Figure 3-1 (L8 and L9). The magnification factor is equal to the ratio of the focal lengths between L9 and L8. Changing one of these two lenses or both of them together, will also change the magnification factor.

Image pixel size in two dimentions was calibrated using a Micrometer Calibration Slide. This Slide contains a scale of 2 mm divided into 200 subdivisions (Micrometer slide 2 mm/200 parts, Labor- und Medizintechnik Rost, Germany). In order to detect the subdivisions under the microscope, normal room light was utilized. It was then possible to detect some of the micrometer calibration slide subdivisions as shown in Figure 4-7. In Figure 4-7, four dark lines were observed. There is a distance of 431 pixels between line 4 and line 1 which corresponds to 30.000 nm. Dividing 30.000 nm by 431 pixels results in 69.6 nm per pixel. The microscope includes an additional lens which magnifies the image to 1.6 times its size and this lens was used to produce this image in Figure 4-7. Therefore, the pixel size should also be divided by 1.6, providing a result of 43.5 nm per pixel.

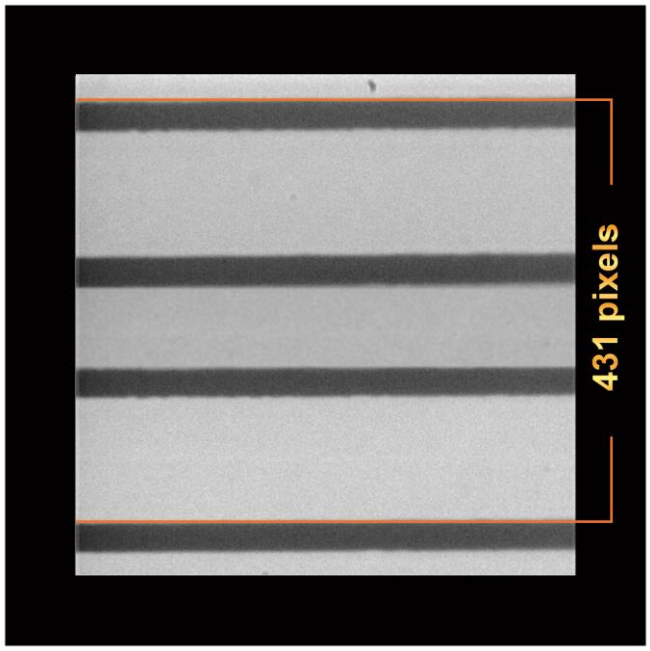

.

Figure 4-7: An image of 4 subdivisions of micrometer calibration slide which contains 200 subdivisions in 2 mm scale

The telescope (L8 and L9) in the detection path was exchanged and therefore the image scale was changed. Figure 4-8 (a-d) demonstrates four different calibrated images. The first image in Figure 4-8 (a) was measured with a 1.6x additional lens in the microscope. Two subdivisions were detected and the pixel size therefore is equivalent to 27.1 nm per pixel in the vertical direction. Figure 4-8 (b) shows the horizontal scale with two subdivisions detected. The pixel size in this dimension is 27.0 nm per pixel using a 1.6x lens. Both images (Figure 4-8 a and b) were measured again, but this time without the 1.6x additional lens (Figure 4-8 c and d). The result is 42.8 nm per pixel in the vertical direction (Figure 4-8c) and 42.6 nm per pixel in the horizontal direction. These values comply with the measured pixel size values obtained by using the 1.6x additional lens which is equal to 1.6 time the pixel sizes in Figure 4-8 (a and b).

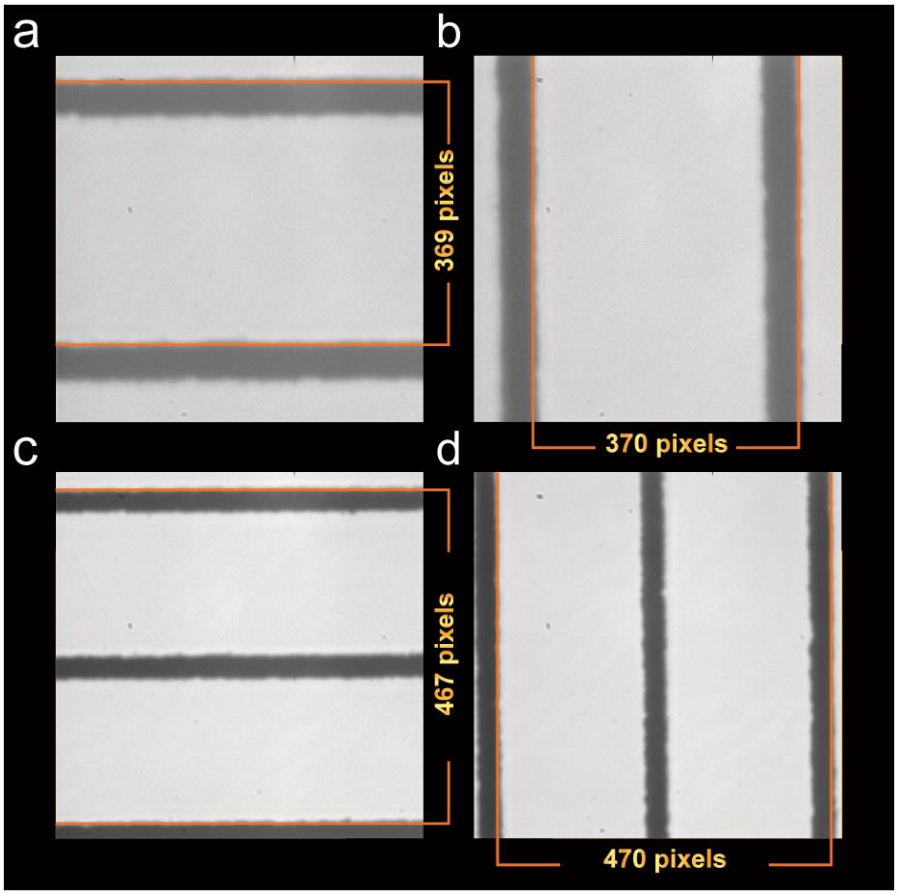

Figure 4-8: Micrometer calibration slide which contains 200 subdivisions in 2 mm scale. Image showing two subdivisions in a vertical direction using additional 1.6x lens (a). Image showing two subdivisions in a horizontal direction using additional 1.6x lens (b). Image showing two subdivisions in vertical direction without using additional 1.6x lens (c). Image showing two subdivisions in a horizontal direction without using additional 1.6x lens (d)

4.1.3 Single Molecule Imaging and validation

The first experiment was carried out on immobilized Alexa Fluor® 488 fluorescent molecules on a cover slip. In the previous section it was demonstrated how four fluorescent molecules have their own individual signals and described the appearance of the simulated average image. A simulation of an image with 625 fluorescent molecules forming a grid-like structure is shown in Figure 4-9. The stimulated fluorescent molecules are separated from

each other and they are not overlapping (Figure 4-9 a). The temporal frequencies in each pixel of an image can be determined using the Fourier transform. The modulation frequency is controlled and all fluorescent molecules will therefore have the same frequency. The difference lies in the phase of each fluorescent molecule's frequency which is the relative proportions of the sine and cosine parts of a frequency the Fourier transform. Each pixel

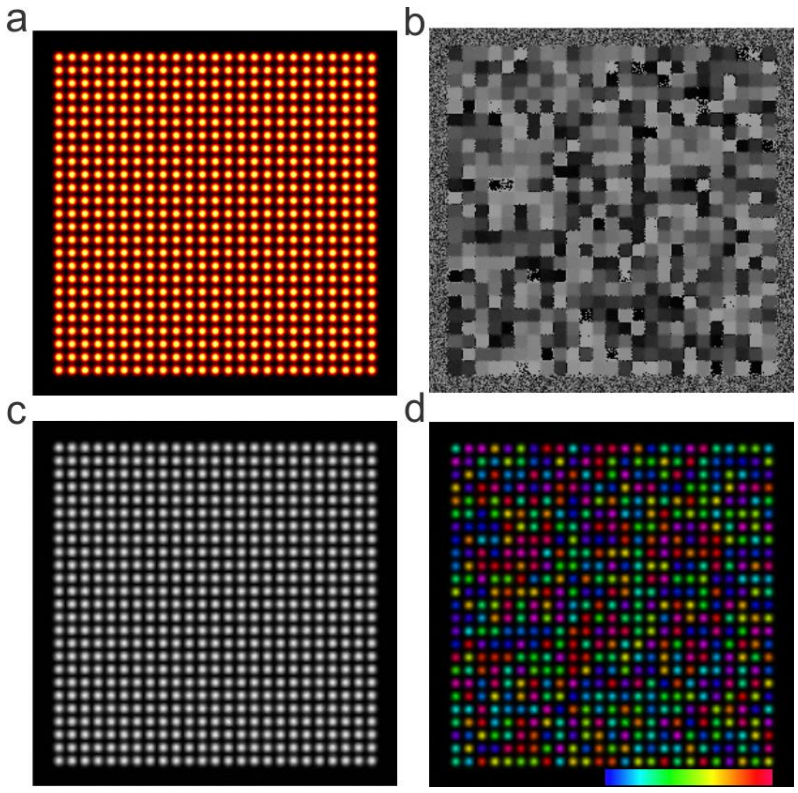

Figure 4-9: Simulated average image of single fluorescent molecules (a). Phase image produced with the Fourier transform of each pixel of the phase average data (b). Modulation Amplitude obtained with the Fourier transform of each pixel in the image (c). Color coded image is a combination of the phase image and the modulation amplitude image and displays different colors (different phases) of the fluorescent molecules (d).

would have a different value (phase code) if the detected signal has a different frequency (which is not the case here) or if it has a different phase (Figure 4-9 b). The Fourier transformation magnitude represents the amplitude of the modulated frequency. This amplitude depends on the fluorescence intensity of the marker (Figure 4-9 c). Using their modulation

amplitudes and their phases to distinguish single molecules is represented by the color coded image, clearly displays a range of different colors (Figure 4-9 d).

When fluorescent single molecules are prepared for imaging on a cover slip, the distribution of those fluorescent molecules will be random and inhomogeneous. The single molecule's distribution density on the coverslip is controlled simply by the fluorescent single molecule concentration. Some single molecules will be attached to other single molecules and some will not. In biological samples, the concentration of the fluorescent molecule should usually be enough (quiet high) to characterize the structure. In this case, the fluorescent molecules will be close to each other and thus cannot be detected or recognized as a single molecule.

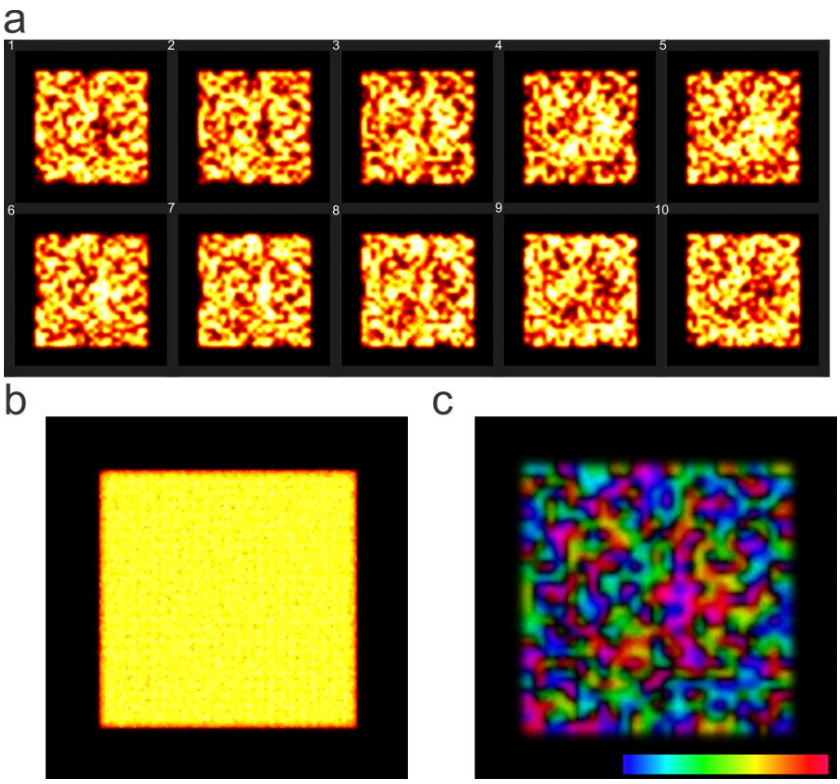

Figure 4-10: Simulated image of overlapping fluorescent markers demonstrates different phases in 10 averaged phase frames (10 periods of rotations) of 100 frames with10 frames per period (a). The average of 100 frames shows a homogeneous fluorescent area (b). Modulation of fluorescent molecules can still be detected and visualized with a color coded image (c).

However, even if the fluorescent molecules are overlapping or are too close to one another, modulated signals from each pixel can still be detected (Figure 4-10). If the sample concentration is not high, then it is possible to recognize that the sample is showing a modulation. The structure in the first frame ($\alpha = 0°$) looks different to that of the other frames in the same period (Figure 4-10 a). The average image of one period stack will combine all structures in one period and there will appear to be no difference between any of the molecules.

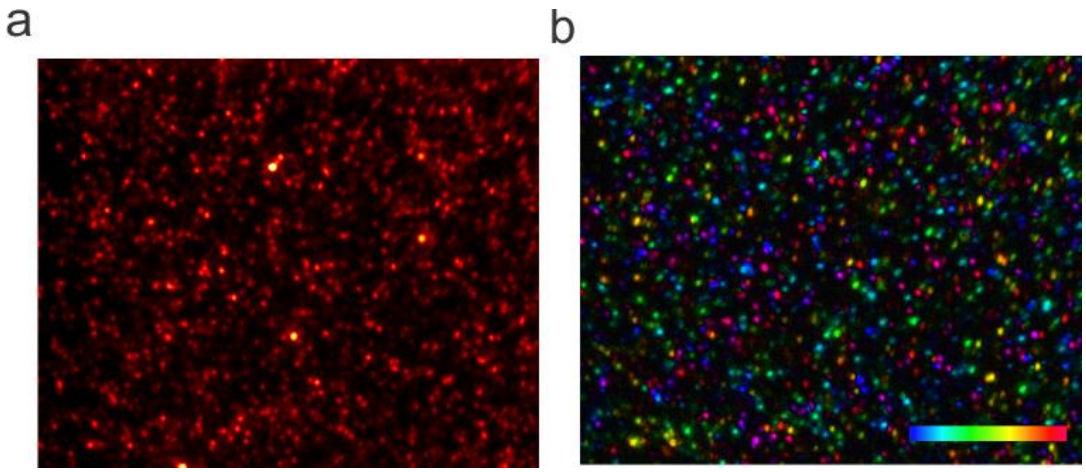

Figure 4-11: Averaged-stack image of immobilized Alexa Fluor® 488 Hydrazide single molecules on a cover slip sample (a). Color coded image produced from the Fourier transform, showing the amplitude and phase of the measured Alexa Fluor® 488 Hydrazide.

The maximum excitation wavelength for Alexa Fluor® 488 Hydrazide is 493 nm and the maximum emission wavelength is 517 nm. Using the setup in Figure 3-2, Alexa Fluor® 488 Hydrazide was measured with a modulation frequency of 20 frames per period. One period is equivalent to a 180° rotation of the linear polarized light. The EMCCD camera's exposure time and frequency were synchronized with the rotatable halfwaveplate to achieve 20 frames per period. The sample was prepared in nanomolar concentration. The diffraction limited image in Figure 4-11 (a) shows the Alexa Fluor® 488 Hydrazide single molecules randomly distributed on a coverslip. Comparatively, the color coded image in Figure 4-11 (**b**) shows Alexa Fluor® 488 Hydrazide single molecules experiencing different phases in

the same manner as the simulated color coded image in Figure 4-10 (d). The first experiment using Polarization Demodulation technique on Alexa Fluor® 488 Hydrazide did indeed display modulation of fluorescent molecules which were directly fixed on a coverslip.

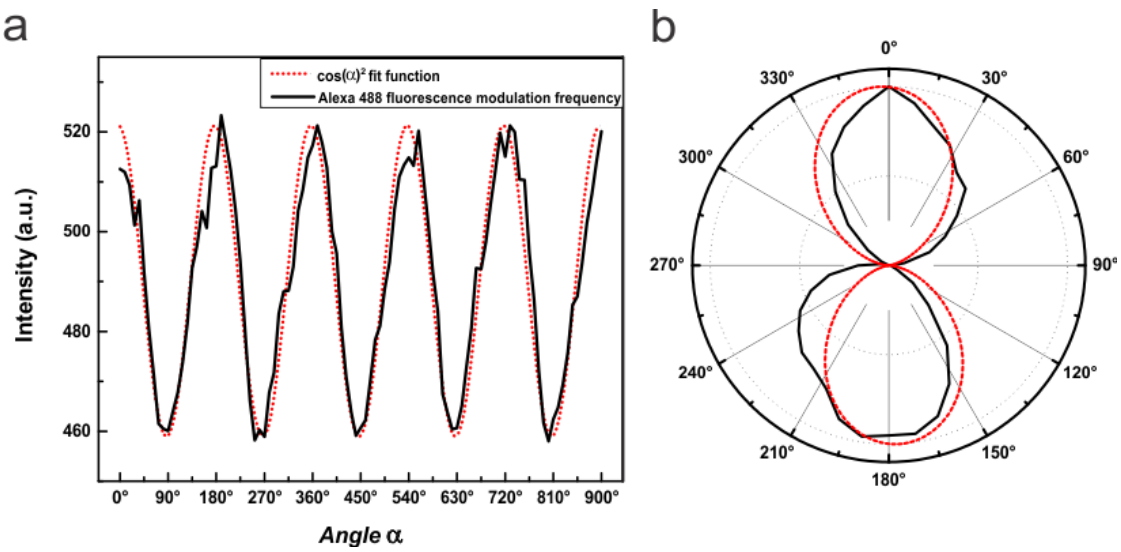

Figure 4-12: Alexa Fluor® 488 Hydrazide single molecule modulated signal (black curve) fitted with a cosine–squared function (red dotted line) (a). Polar plot of one Alexa Fluor® 488 Hydrazide single molecule fitted with a simulated polar plot of a cosine-squared function (b).

The modulation signal of the Alexa Fluor® 488 Hydrazide fits very well with the cosine-squared function (Figure 4-12 **a**). Also the polar plot of the Alexa Fluor® 488 Hydrazide modulation signal fits very well with the simulated polar plot (Figure 4-12 **b**).

The modulation signals of four selected molecules from the Alexa Fluor® 488 Hydrazide measured sample also show cosine-square functions (Figure 4-13 **a**). These signals differ from each other in their phases, their modulation intensities and their average intensities. The simulated modulation signals in Figure 4-5 comply with the real data measured using Alexa Fluor® 488 Hydrazide. By plotting these four modulation signals in a polar plot, the effective excitation angle range for each molecule is shown to be different from the others (Figure 4-13 **b**) and can be nicely compared with the simulated polar plot in figure

(Figure 4-5 **c**). Meanwhile, when the four molecules spatially overlap, the phase information is maintained in each molecule.

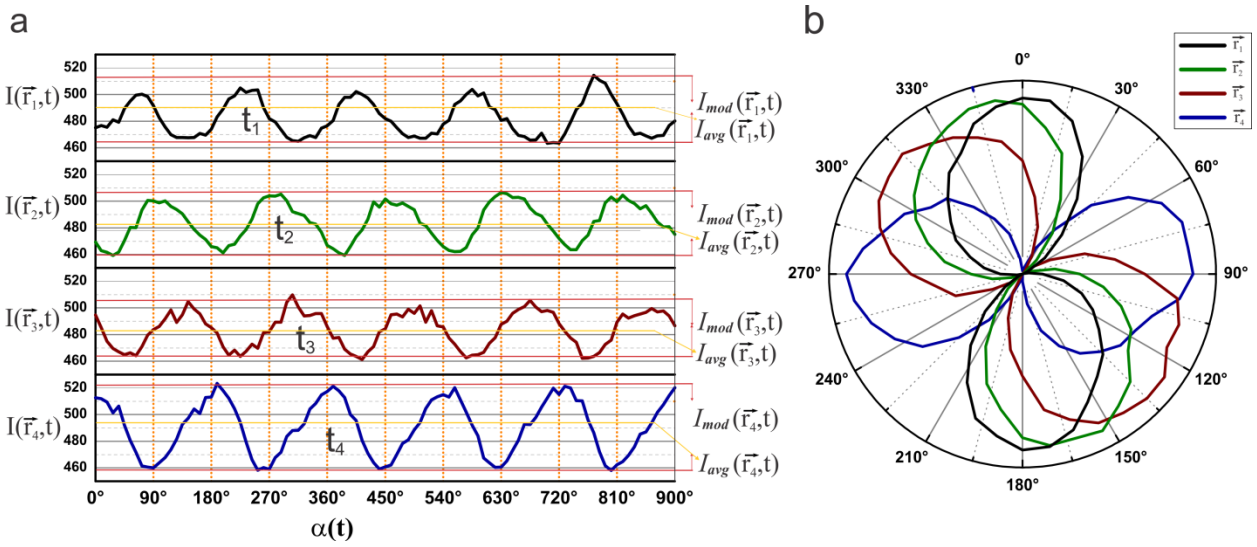

Figure 4-13: modulation signals of four selected molecules from the Alexa Fluor® 488 Hydrazide sample, each with different phases as noted with **(t_1, t_2, t_3 and t_4),** different modulation amplitudes noted with **($I_{mod}(\vec{r_1},t)$, $I_{mod}(\vec{r_2},t)$, $I_{mod}(\vec{r_3},t)$ and $I_{mod}(\vec{r_4},t)$)** and different average modulation intensities noted with **($I_{avg}(\vec{r_1},t)$, $I_{avg}(\vec{r_2},t)$, $I_{avg}(\vec{r_3},t)$ and $I_{avg}(\vec{r_4},t)$** (a).

By using the orientation information of each single molecule, it is possible to distinguish between two single molecules by their phases when they overlap spatially but they differ in their orientations. Figure 4-14 demonstrates that using the modulation amplitudes information alone enables separation between two single molecules down to 77 nm in these examples. Column Figure 4-14 (d) shows clearly two maxima that correspond to two single molecules positions. The two maxima are undetectable in the diffraction limited plot (column Figure 4-14 **c**). By 77 nm distance, the two maxima are not clearly observed but the phase separation between the two single molecules is shown in column Figure 4-14 (e). The position of each curve (the maximum of the blue and the red curve) complies very well with the corresponding two maxima in column Figure 4-14 (d) for the 77 nm distance.

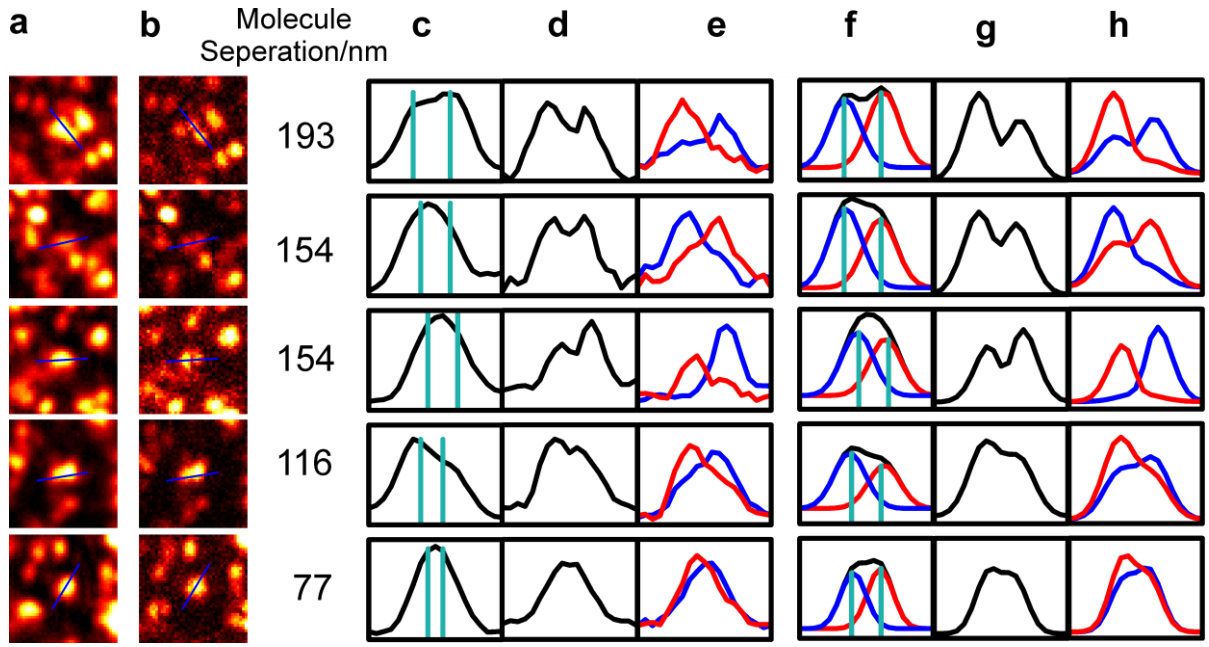

Figure 4-14: Diffraction limited image of two single molecules and a profile plot (blue line), as used for the data shown in c-h (a). Corresponding modulation amplitude image and a profile plot (blue line) are used as well for the data shown in c-h (b). Profile plot graphs of the diffraction limited image shown in a (c). Vertical cyan lines indicate the true position of single molecule in each profile plot (c). Corresponding profile plots of the modulation amplitude shown in b (d). Corresponding profile plots to the raw modulating data in two selected image time frames both with maximum phase separation (e). The red and blue curves are single time frames. Fitted curves of the data shown in c, d and e with two modulating Gaussian functions demonstrate the theoretical curves without noise (f, g and h). The blue and the red curves in h are the fitting curves to the corresponding curves shown in e. The blue and the red curves in f represent two Gaussian peak functions separated into two peaks. Their center, indicated with cyan vertical lines, shows the fitting position of the actin fibers.

4.1.4 Polymerized F-actin on Surface

The actin molecule is a single polypeptide formed of 375 amino acids and has a globe-shaped structure in its monomer form. Therefore, the actin monomer is termed G-actin (G; Globular). The G-actin monomers polymerize to form a linear fibrous (also termed filamentous (F)) actin which is the main constituent element of thin filaments and microfilaments in all types of eukaryotic cells. The G-actin monomer is composed of four subdomains form-

ing two lobes and a cleft. Inside the cleft is an ATP or ADP and Mg^{+2}, all bound together and the nucleotide stabilizes the G-actin monomer (Figure 4-15).

The G-actin monomer polymerizes into F-actin filament when the ionic strength of the solution has reached a certain level. This is achieved through the addition of Na+, Mg^{+2} or K^{+} -ions. The F-actin filament will depolymerize if the ionic strength decreases. The pointed end is found on the side of subdomain 4 and subdomain 2 and the barbed end is positioned in the opposite direction on the side of subdomain 3 and subdomain 1. Polymerization of G-actin takes place over three steps. The assembly starts with the nucleation process which involves the formation of Actin dimers and trimmers. A stable nucleus is usually made up of three or four subunits, and once formed, enables the process to continue to the elongation stage. The elongation takes place at both ends; however, the growth rate at the barbed end is five to ten times faster than at the pointed end. The reason for this is that the incorporated G-actin monomers hydrolyze ATP to ADP which leads to a conformational change in subdomain 2 [55].

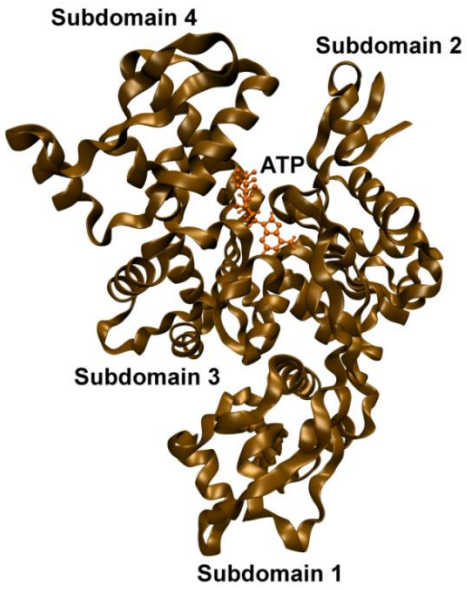

Figure 4-15: G-actin monomer structure shows subdomains1, 2, 3 and 4. ATP binds to the G-actin at its cleft center. The protein structure (1P8Z) was downloaded from RCSB PDB library and visualized using VMD software.

The interaction of G-actin at the pointed end is therefore weakened and the dissociation of actin monomers is increased. After a certain time, the concentration of G-actin monomers decreases and reaches equilibrium with F-actin. At this stage, the exchange rate between polymerization and dissociation is equal. Thus, the total mass of the filament is constant.

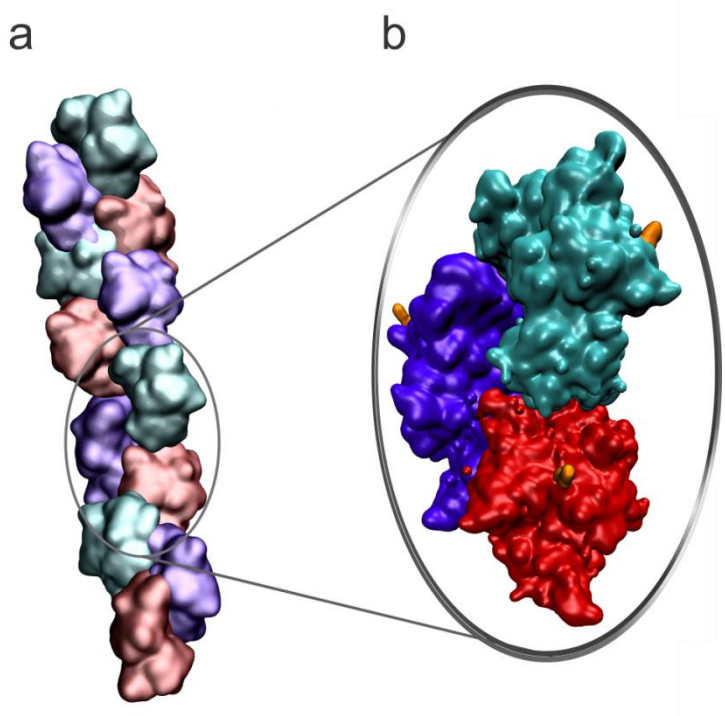

Figure 4-16: F-actin in alpha-helix structure (a). Oligomer of 3 actin monomers forming a nucleus for elongation phase in the polymerization process (b). The three monomers are colored with cyan, red and violet. One ATP molecule is bound to each monomer and they are illustrated in orange color. The illustration of the F-actin and the oligomer structures is an approximation and it is not a precise drawing [56].

F-actin is a long double-stranded, right-handed, helical filamentous formed from G-actin monomers (Figure 4-16). One monomer translation relative to the preceding monomer is ~27.5 Å and rotates 166°. This means that the structure repeats itself every 27.5 Å but it rotates 166°. Phalloidin is a bicyclic heptapetide extracted from the *Amanita phalloides* mushroom. Phalloidin binds specifically to the F-actin polymer at the interface between its subunits. This means that Phalloidin binds the subunits together, preventing F-actin from

depolymerizing. Another theory on stabilizing F-actin through conformational changes of F-actin induced by Phalloidin was suggested by another group of scientists. Oda et al. determined the position and the orientation of Phalloidin in F-actin [57] with the help of the Lorenz F-actin model [58,59]. The role of Phalloidin in stabilizing F-actin is due to Phalloidin binding between the two strands in F-actin.

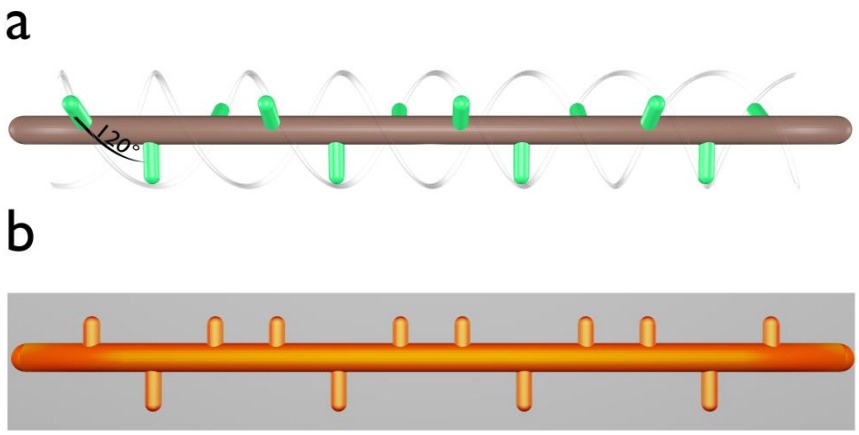

Figure 4-17: Illustration of F-actin (in brown) labelled with fluorescent dyes (in green) (a). The fluorescent dyes are attached to high-affinity filamentous actin Phalloidin linker. The fluorescent molecules are oriented perpendicular to the F-actin fiber. The fluorescent dyes rotate around the f-actin fiber at 120° per fluorescent dye as depicted in (a). When the labelled F-actin in (a) is viewed in two dimensional view as is usually the case in wide-field microscopy then the sample appear as it is illustrated in (b). It appears as the fluorescent dyes are in plane with the F-actin fiber and the fluorescent dyes are still perpendicular to the F-actin extension.

The position of Phalloidin in F-actin was located between three monomers and Phalloidin orientation was determined by estimating the most plausible orientation of Phalloidin electron densities as illustrated in Oda et al. figure 4 [56]. The result was that Phalloidin electron density orientation is perpendicular to F-actin sheet. In the same study, the orientation of Rhodamine fluorescent dye was also determined in the same manner as Phalloidin. In Oda et al. figure 7 [56] they showed that the electron density of Rhodamine is oriented along with Phalloidin electron density orientation. In this work, F-actin was labelled with ATTO 590

Phalloidin fluorescent dye and we expect that ATTO 590 dye is oriented as it was described for Rhodamine. Figure 4-17 shows a Schematic illustration depicting labelled F-actin with fluorescent dyes oriented perpendicular to F-actin extension. The fact that F-actin is a double stranded α-helical polymer and the fact that monomers rotate 166° relative to the preceding monomer make it difficult to estimate the angle of the fluorescent dye around F-actin. The fluorescent dye shall always be perpendicular to F-actin fiber and this dimension is fixed. Supposing that the fluorescent dyes are rotating in 120° step (Figure 4-17 a) and if the sample was prepared on a coverslip and measured with a standard wide-field microscope, the image will appear in 2-D (Figure 4-17 b) as an example. If this sample illuminated with a linear polarized laser beam then the fluorescence dyes will be excited when the linear polarized light is parallel to the fluorescent dyes or perpendicular to the f-actin extension. Thereby the sample should show a homogenous fluorescence when excited with a linear polarized light.

The position where Phalloidin binds to F-actin is located between three monomers. Phalloidin orientation was determined by estimating the most plausible orientation of Phalloidin electron densities as illustrated by Oda et al. in figure 4 [56]. The result was that the Phalloidin electron density orientation is perpendicular to the F-actin sheet. The same study determined the orientation of Rhodamine fluorescent dye in the same manner as Phalloidin. As Oda et al. show in figure 7 [56], the electron density of Rhodamine is oriented along with Phalloidin electron density orientation. In this work, F-actin was labelled with ATTO 590 Phalloidin fluorescent dye and it was expected that the orientation of the ATTO 590 dye would be determined in the same way as it was for Rhodamine. Figure 4-17 shows a Schematic illustration depicting fluorescent dyes oriented perpendicular to F-actin extension. The fact that F-actin is a double stranded α-helical polymer and that the monomers rotate 166° relative to the preceding monomer makes it difficult to estimate the angle of the fluorescent dye around F-actin. It is certain however that the fluorescent dye shall always be perpendicular to the F-actin fiber and that this dimension is fixed. Supposing that the fluorescent dyes rotate in a 120° step as depicted in Figure 4-17 (a), and that the sample was prepared on a coverslip and measured with a standard wide-field microscope, the image should appear in two dimensions as depicted in Figure 4-17 (b), for example. If this

sample was to be illuminated with a linear polarized laser beam, then the fluorescent dyes will be excited when the polarization of light is parallel to the fluorescent dyes or perpendicular to the f-actin fiber. Therefore, the sample should have a homogenous fluorescence when excited with a linear polarized light.

ATTO 590 phalloidin labelled actin filaments was polymerized and prepared on a coverslip, as explained in section 3.2.8, and measured using the Polarization Demodulation setup illustrated in Figure 3-1. The excitation laser beam, with a 568 nm wavelength, was generated by OPO pp Vis. and used to illuminate F-actin labelled with ATTO- 590 Phalloidin samples. The F-actin filaments are considered to be just as densely labeled as other biological samples. They are also homogenously labeled and their label orientations persist in a certain order, as illustrated in Figure 4-17. The advantage of this is that when the neighboring actin filaments have different orientations, one actin filament can be selectively excited with linear polarized light and the fiber positions can be well defined. Figure 4-18 shows these facts in details, where an average stacked image of actin filament shows just a diffraction limited image (Figure 4-18 a) but a corresponding color coded phase image provides more information about their orientations (Figure 4-18 b). An inset of the crossing region as an example, the image shows two fibers with an angle of 70° between them and two different colors denoting different phases (Figure 4-18 c). One period of rotation is recorded within 15 frames and each frame has an exposure time of $\sim$33 ms which leads to a recording accuracy of one frame per 12° of linear polarized light rotation. Frames 2, 7 and 14 are averaged from 30 periods and some fragments in frames 2, 7 and 14 are invisible due to the rotation of the linear polarized light (Figure 4-18 d, e and f). Two crossing fibers differing by 70° in frame 2, 7 and 14 are excited and they appear as shown in figure 3-33 g when linear polarized light is oriented parallel to the middle of the two fibers crossing. Rotating the linear polarized light to be parallel to each fiber results in exciting one fiber while the second fiber remains unexcited as shown in Figure 4-18 (h and i). When the angle between the two fibers decreases the overlap of the two fibers emission increases because the labels orientations become similar.

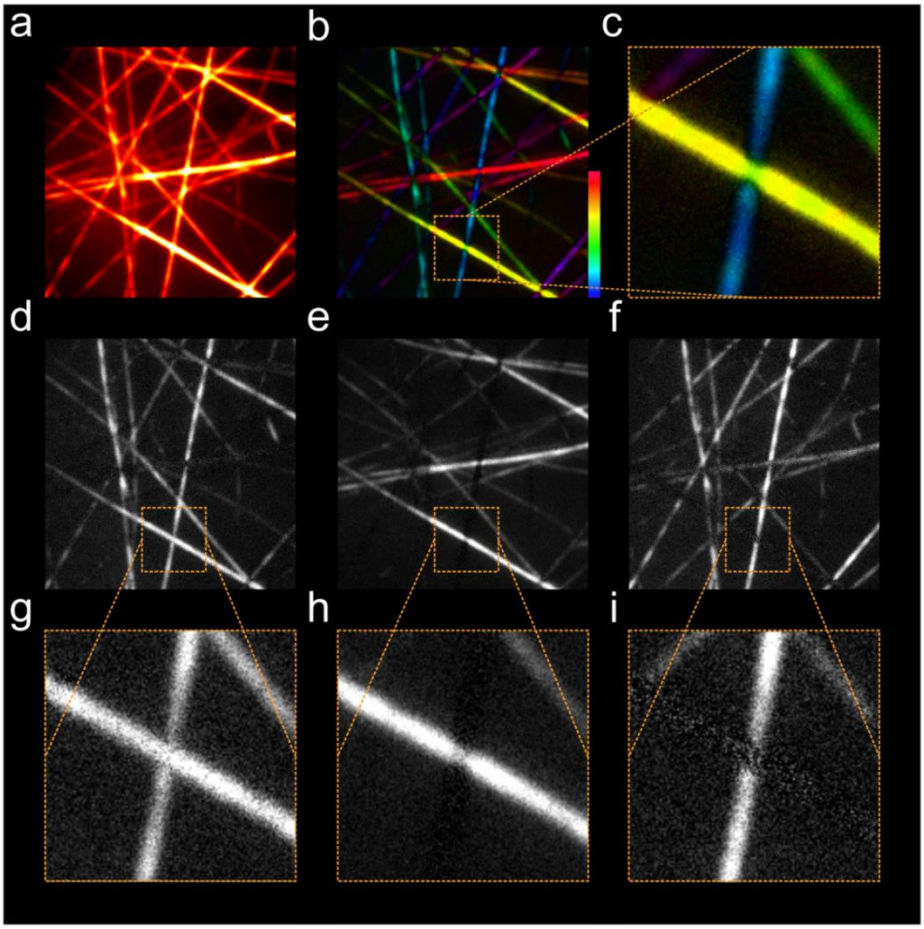

Figure 4-18: Diffraction limited image of F-actin showing actin fibers in line structure (a). Corresponding color coded image produced from the Fourier transform amplitude and phase of the modulated stacked-image of F-actin (b), Zooming in at a crossing of two F-actin fibers from the corresponding color coded image shows two colors that represent two frequencies along each fiber (c). At the crossing point, the modulation frequencies from each actin fiber reach a high overlap. The amplitude of the two frequencies therefore decreases or in some cases demolish. One period of rotation of the linear polarized excitation beam occurred within 15 frames. Frame 2, 7 and 14 are shown in (d, e and f) respectively. Zooming in (d, e and f) to the same region in (f) shows that the crossing two fibers in frame 2 appears clearly (g). On the other hand in frame 7 and after rotating the linear polarized light 60° from its position in frame 2, one F-actin fiber appears and the second F-actin fiber disappears (h). After rotating the linear polarized light 84° from its position in frame 7 which leads to frame 14, the F-actin fibers switch their appearance. The reason is that f-actin fibers are homogeneously oriented along F-actin fiber and therefore they are selectively excited when the angle between the fibers is close to 90°.

4.1.5 Subdiffractional structures in Labelled Actin Fibers

Periodic signals with different phases can be obtained from labeled rigid sample structures ranging from single molecules attached to a microscope coverslips to densely labeled nerve cells. Even if the sample has a very dynamic fluorescent dye mobility it is still possible to detect modulation (GUVs samples in Figure 4-42). The modulation amplitude depends on the number of photons emitted and the noise of the CCD camera background, as well as the overlap of signals from adjacent emitters, as illustrated in Figure 4-6. According to Abbe's law, diffraction limited structures are unresolvable with a standard imaging light microscopy. This is due to the fact that the spatial overlap of emitters takes place below the diffraction limit. The recorded periodical signals with SPoD set-up from different emitters provides additional information about the orientation of one emitter in one pixel or in a nanoarea in the case of single molecule sample. The additional information about the average orientation of several emitters in one pixel or in a nanoarea can be also determined .

Linear fibrous actin samples show a homogeneous label orientation when labelled with phalloidin –Marker as described in section 4.1.4. ATTO 590 Phalloidin was used to label F-actin, resulting in a fluorescent dye that oriented at an angle perpendicular to the actin fiber extension. The linear actin fiber has a $\sim$ 9 pixels point spread function (PSF) corresponding to $\sim$240 nm PSF. The PSF was determined by the FWHM of the fitted Gaussian function. The measured linear actin fiber was then fitted with a Gaussian function to find the best fitting line which represents the true position of the actin fiber. A diffraction limited image of a crossing linear actin fiber is limited to a resolution of $\sim$250 nm. By modulating two linear actin fibers that differ in their molecular orientations, it should be possible to differentiate between the two fibers at a level below the diffraction limit, when considering the raw modulation information. A simulation of one period (60 frames per 180° of rotation) for two fibers crossing at 90° angles demonstrates the full separation of the two fibers in the Time-Frame scale, as illustrated in Figure 4-19. The distance between the two maxima of the actin fibers shows a 90° shift (Figure 4-19 b) and this complies with the true angle between the two actin fibers. A three dimensional projection of one period shows a clear separation between the two fiber structures (Figure 4-19, a i-v). The third dimension corresponds to

the time frame. 10 periods of recording, for example, will reproduce the separation between the two fibers in each period (Figure 4-19 c i-v and d). The advantage of measuring multi-periods instead of one period is that it reduces noise and background in measured samples and improves the modulation amplitude of these samples once the measured periods are averaged.

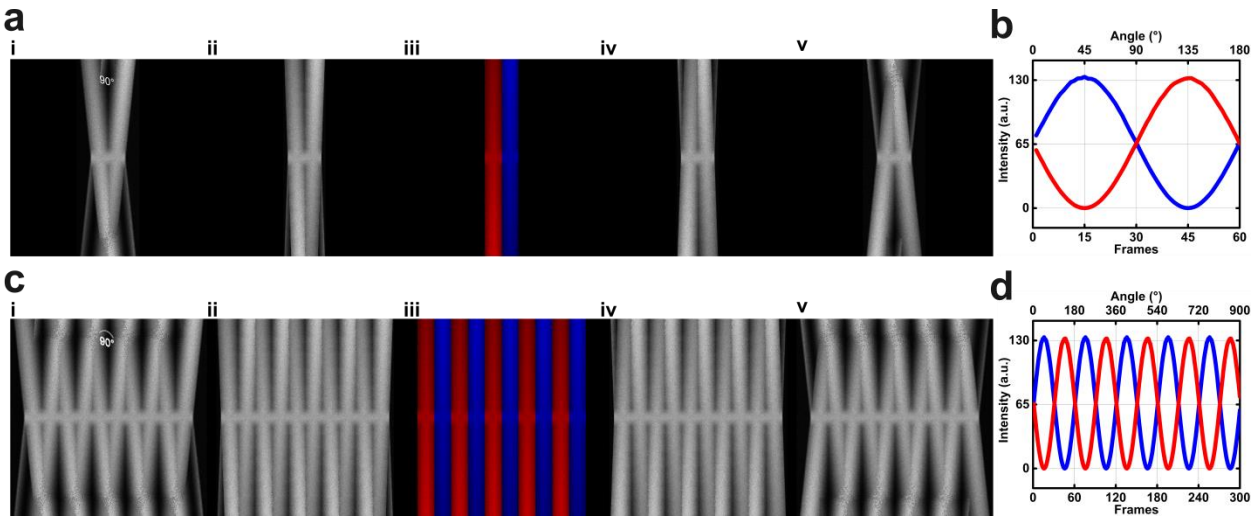

Figure 4-19: Simulation of two actin fibers of a homogenous label orientation. The angle between the two fibers in the crossing region is 90°. One period of 60 frames per 180° of rotation is simulated and illustrated in 3D stacks (a i-v). The 3D illustration clearly shows the complete separation between the two fibers in the time frames axis. The phase shift between the two fibers is 90° which correspond to a half rotation and a half period of 30 frames (b). Measuring ten periods results in the same separation in each period (c i-v) and the phase shift maintain by 90° for all periods (d).

ATTO 590 phalloidin labelled actin filaments were systematically investigated. A series of profile plots of the modulation amplitudes in the vicinity of the crossing fibers are demonstrated for different crossing angles. The angles correspond to the phase difference of the

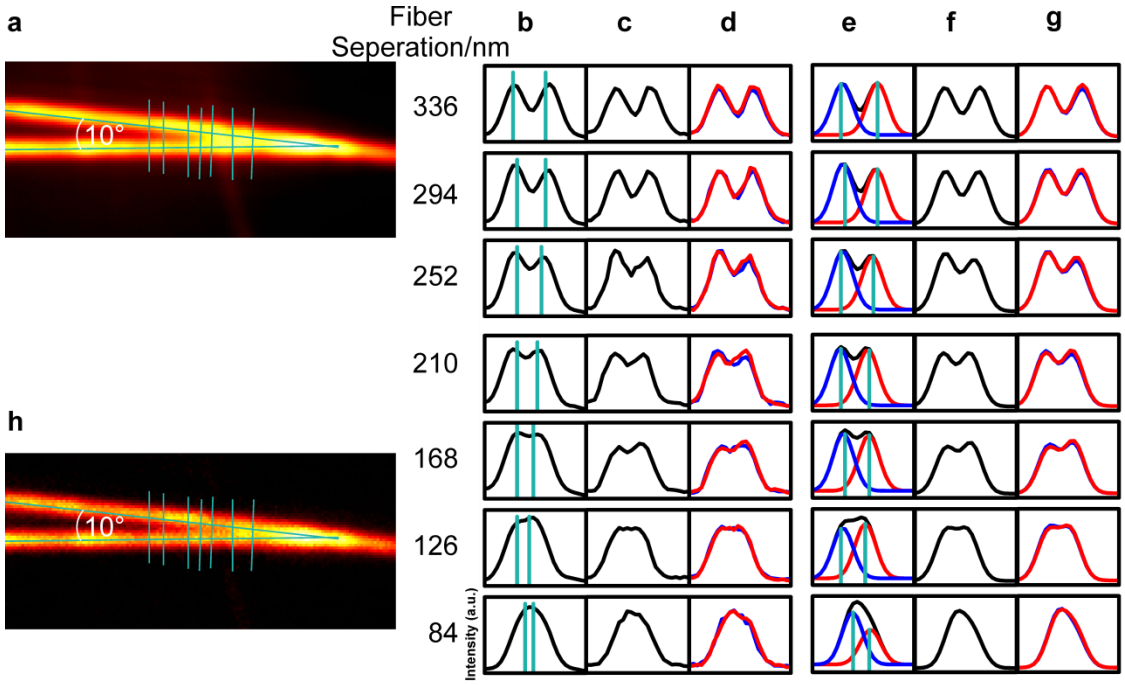

Figure 4-20: Diffraction limited image of two actin fibers differing by 10° in label polarization. Fitted cyan lines show the true positions for each actin fiber and seven vertical profile plots, as used for the data shown in b-g (a). Profile plot graphs of the diffraction limited image shown in a (b). Vertical cyan lines indicate the true position of actin fiber in each profile plot (b). Corresponding profile plots of the modulation amplitude shown in h (c). Corresponding profile plots to the raw modulating data in two selected image time frames both with maximum phase separation (d). The red and blue curves are single time frames. Fitted curves of the data shown in b, c and d with two modulating Gaussian functions demonstrate the theoretical curves without noise (e, f and g). The blue and the red curves in g are the fitting curves to the corresponding curves shown in d. The blue and the red curves in e represent two Gaussian peak functions separated into two peaks. Their center, indicated with cyan vertical lines, shows the fitting position of the actin fibers. The modulation amplitude image, the true actin fiber positions and the profile plots correspond to (h).

molecular orientation of each actin fiber. Two labeled actin fibers sample differing by ~10° in their direction and polarization is investigated. The true position of each fiber can be determined by fitting the entire fiber with a Gaussian function from specific image frames of the raw modulating data. The Gaussian maximum corresponds to the center of the fiber. Once the series of center points were fitted along the entire actin fiber for a best linear fit, the true position of each actin fiber could be determined (Figure 4-20 a and h, cyan lines

along the actin fiber). A series of profile plot lines were chosen for distances below and above the diffraction limit. These plot lines were previously determined along with the true positions of the actin fibers (Figure 4-20 a and h, seven cyan lines perpendicular to the virtual center of the two actin fibers). The profile plots of the modulation amplitudes were plotted as distances in nanometer against intensity.

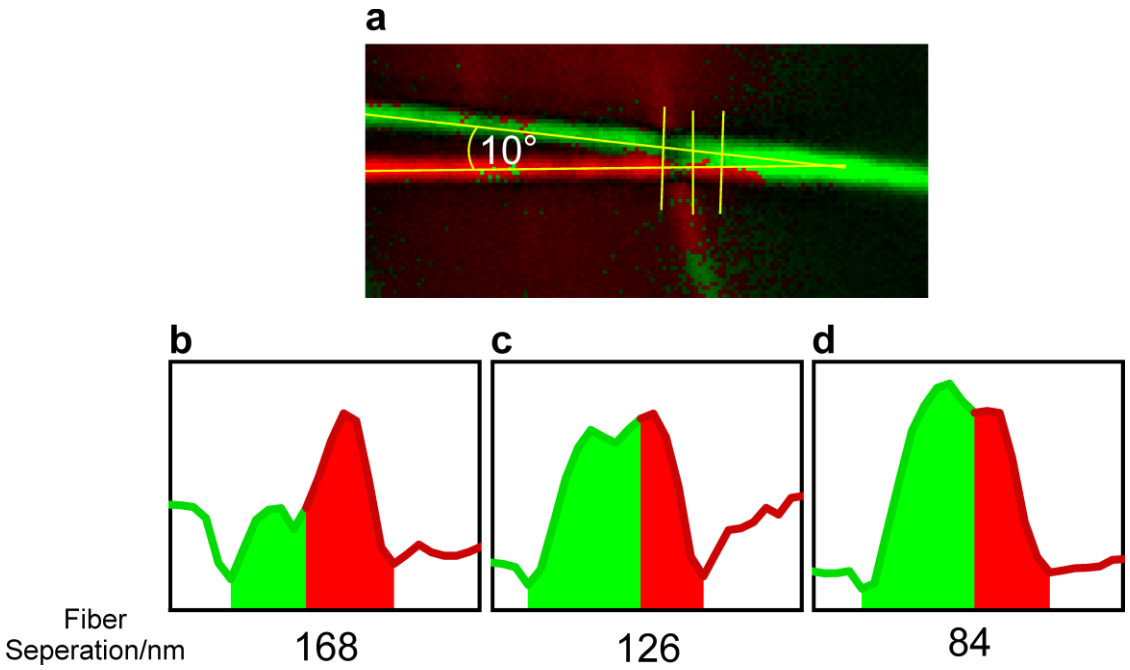

Figure 4-21: Two labeled actin fibers sample differing by ~10° in their direction and polarization are separated by their phases and demonstrated in two colors; red and green. The two crossing actin fibers show clearly two phases along each fiber in red and green until they completely overlap (a). Corresponding profile plots (yellow lines) with distances below the diffraction limit are plotted showing distinguishable two colors phase separation at 168 nm, 126 nm and 84 nm true fibers separation distances (b-d).

With just 10° of phase separation, it is hard to use the information directly for further subdiffractional separation (column Figure 4-20 d). The linear polarized light has a distribution over a rotation step of 12° which make it hard to distinguish any phases below an angle of 12°. If the step resolution improved then it would be possible to gain more information on the subdiffractional region. However, phase separation in the subdiffractional crossing region is observed (Figure 4-21) when illustrating the fibers using their frequency information

defined only by two colors. Since the actin fiber is homogeneously oriented, the crossing region shows two colors which corresponds to two different phases. The phase separation distinguishes the two actin fiber down to ~84 nm (Figure 4-21 b-d).

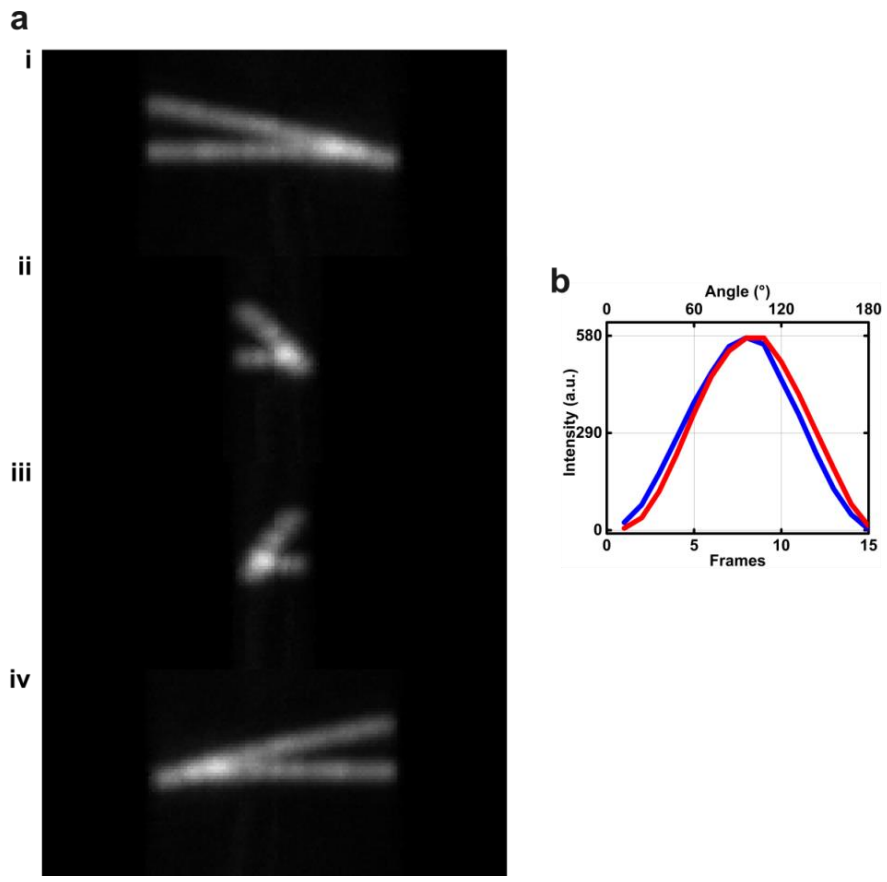

Figure 4-22: One period of 15 frames per 180° of rotation is constructed in 3D projection with fuor different angle rotating around the y-axis (a). The angle between the actin fiber direction and polarization is 10° and no clear separation can be observed. Plotting the intensity of each actin fiber against time frames (blue and red curves) shows a slight phase shift (b).

One period of the raw modulating data is constructed to a 3D image (Figure 4-22 a i-iv), comparable to the simulated 3D actin fibers in Figure 4-19 (a). The simulated 3D figure with a polarization and direction angle of 90° demonstrated a good phase separation in the time frame dimension. With a 10° phase shift however it is difficult to distinguish the actin fibers because almost no phase shift is detected (Figure 4-22 b). With higher polarization

angle of the actin fiber, it should be possible to observe a clearer fiber separation and a clearer phase shift. An animation video of the 3D structure is one of the best ways to view the separation between the actin fibers.

The next investigated labeled actin filament differs in labeling orientation and fiber direction by 40°. From diffraction limited images, separation below the Abbe-limit ~250 nm is not possible (column Figure 4-23 b). However, the modulation amplitude data demonstrates that the two fibers can be separated down to a distance of ~134 nm (column Figure 4-23 **c**). Distinct time frames of the modulating part of the raw data show that the two fibers can be differentiated even further, down to a distance of about 54 nm (column Figure 4-23 d). Fitting two Gaussian functions to diffraction limited images (column Figure 4-23 e), to the modulation amplitude data (column Figure 4-23 f) and to distinct time frames of the modulating part (column Figure 4-23 g) demonstrates how the peaks and the separation should be theoretically, avoiding peak noises und deviations. The fittings in column (f) show two peaks separated down to 134 nm distance and column (g) shows distinguishable peaks down to 54 nm.

The phase separation for this sample in the subdiffractional crossing region can be again observed (Figure 4-24) when illustrating the fibers using their frequency information defined only by two colors. Since the actin fiber is homogeneously oriented, the crossing region shows two colors which corresponds to two different phases. The phase separation distinguishes the two actin fiber also here down to ~54 nm (Figure 4-21 b-d).

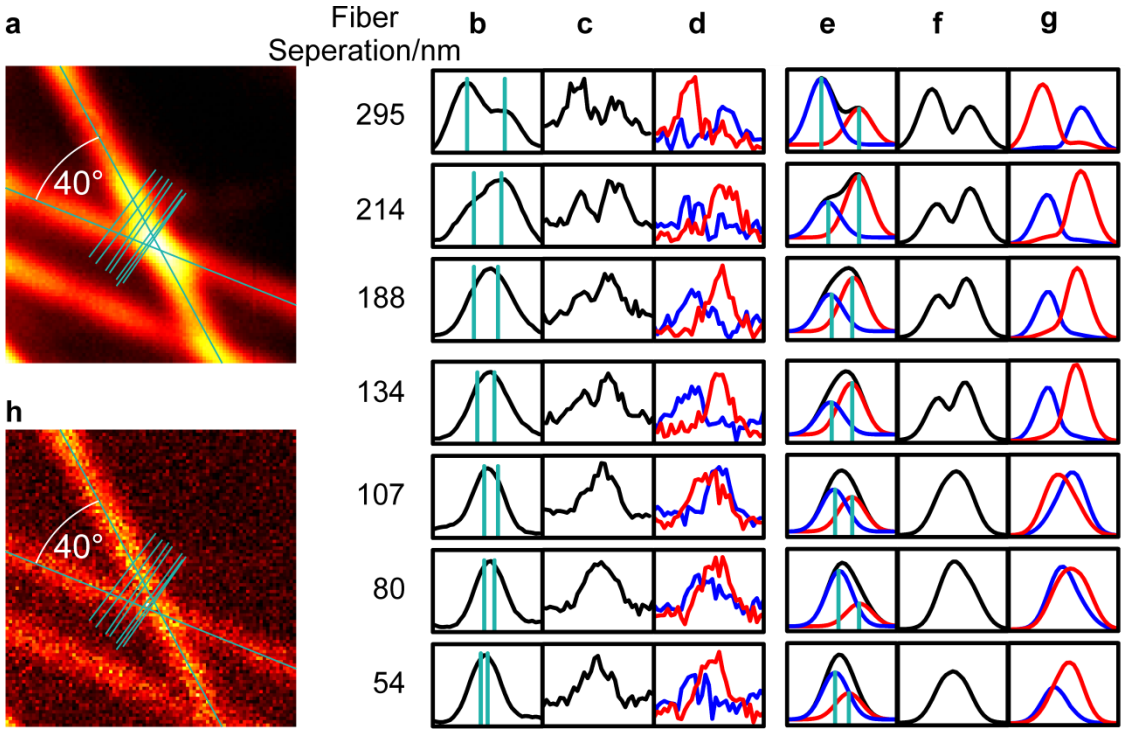

Figure 4-23: Diffraction limited image of two actin fibers differing by 40° in label polarization. Fitted cyan lines show the true positions for each actin fiber and seven vertical profile plots used for the data shown in b-g (a). Profile plot graphs of the diffraction limited image shown in a (b). Vertical cyan lines indicate the true position of the actin fiber in each profile plot (b). Corresponding profile plots of the modulation amplitude shown in h (c). Corresponding profile plots of the raw modulating data in two selected image time frames, each of which has a maximum phase separation (d). The red and blue curves are single time frames. Fitted curves of the data shown in b, c and d with two modulating Gaussian functions display the theoretical curves without noise (e, f and g). The blue and the red curves in g are fitting curves corresponding to the curves shown in d. The blue and the red curves in e are the two Gaussian peak functions. They are separated into two peaks and their center is represented by cyan vertical lines showing the fitting position of the actin fibers. The modulation amplitude image, the true actin fiber positions and the profile plots correspond to a (h).

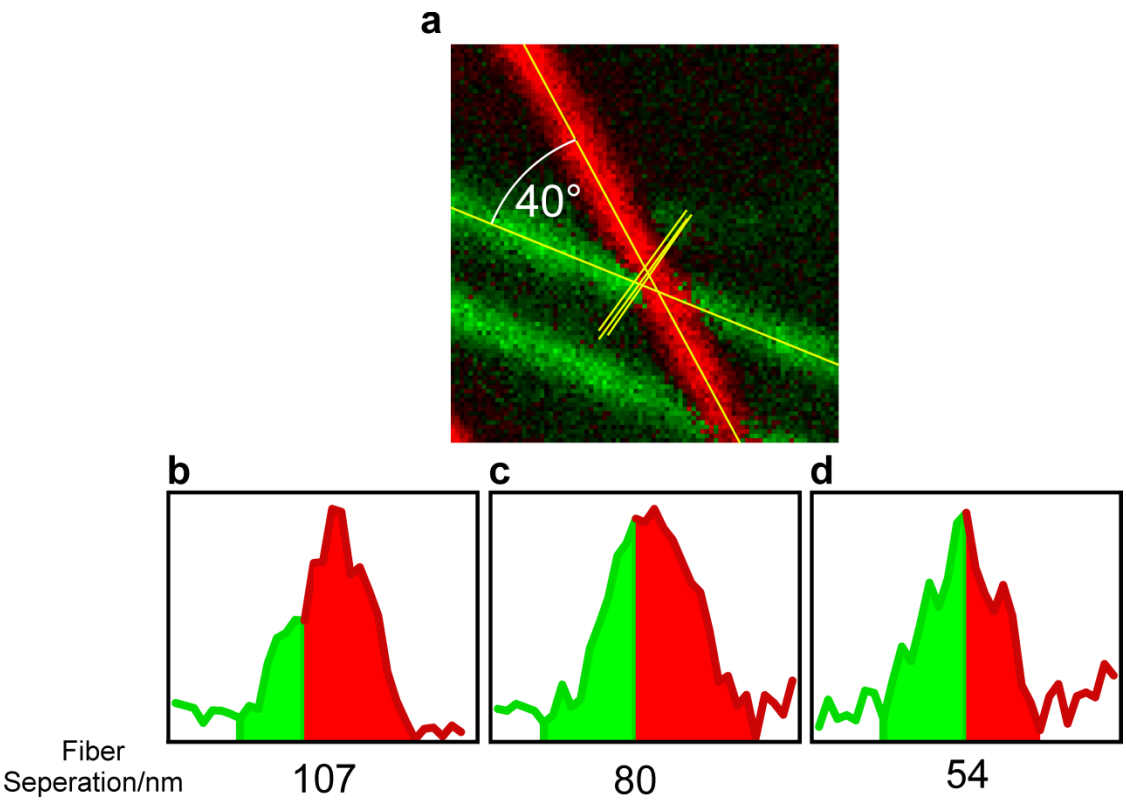

Figure 4-24: Two labeled actin fibers sample differing by ~40° in their direction and polarization are separated by their phases and demonstrated in two colors; red and green. The two crossing actin fibers show clearly two phases along each fiber in red and green until they completely overlap (a). Corresponding profile plots (yellow lines) with distances below the diffraction limit are plotted showing distinguishable two colors phase separation at 107 nm, 80 nm and 54 nm true fibers separation distances (b-d).

Again one period of the raw modulating data is constructed to a 3D image (Figure 4-25 a i-iv). With 40° phase shift it is possible to distinguish the actin fibers as it is shown in view position (ii) and (iii). The phase shift of 40° is observed (Figure 4-25 b). An animation video of the 3D structure can show the separation between the actin fibers much more clearly.

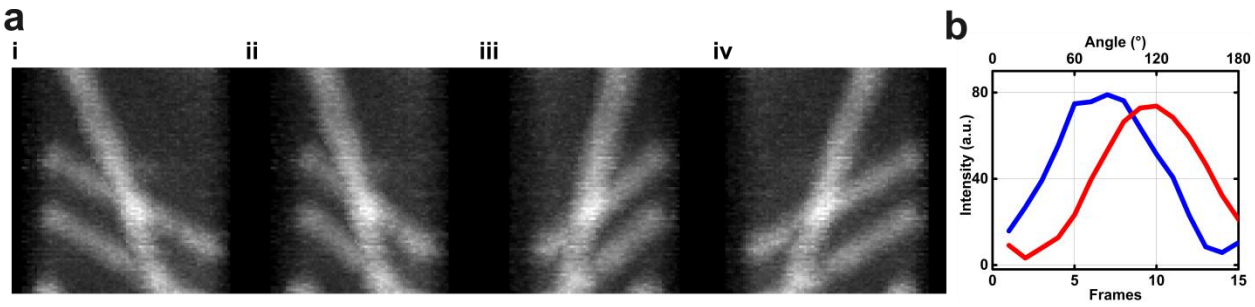

Figure 4-25: One period of 15 frames per 180° of rotation is constructed in 3D view. The view shows four different angles rotating around the y-axis (a). The angle between the actin fiber's direction and polarization is 40° and a separation can be observed in ii and iii. Plotting the intensity of each actin fiber against time frames (blue and red curves) indicates the phase shift of ~40° between the two actin fibers (b).

The investigation of labeled actin filament continues examining labeling orientation and fiber direction differing by 50°. The diffraction limited images demonstrate yet again that no separation below ~250 nm is possible (column Figure 4-26 b). Since the modulation amplitudes are relatively different in this example, further separation from the amplitude data alone is difficult. However, distinct time frames of the modulating part of the raw modulation data show again that the two fibers could be clearly differentiated down to a distance of about ~54 nm (column Figure 4-26 d). Moreover, when illustrating the fibers using their frequency information defined only by two colors, the phase separation distinguishes the two actin fiber also here down to ~54 nm (Figure 4-27 b-d).

Fitting two Gaussian functions to diffraction limited images (column Figure 4-26 e) to the modulation amplitude data (column Figure 4-26 f), and to distinct time frames of the modulating part (column Figure 4-26 g) demonstrates theoretically optimum curves avoiding high peak noise und deviations. The fittings in column (g) contain distinguishable peaks (red and blue) down to 54 nm.

When repeating the construction of a 3D image of one period of raw data for a 50° sample (Figure 4-28 a i-iv), it is possible to distinguish the actin fibers in (ii) and (iii). The phase shift of 50° is indicated with the red and blue curves (Figure 4-28 b). Other actin fibers ap-

pear in the 3D image and they have phases different to those of the two actin fibers under investigation. Thus, it is difficult to distinguish between the actin fibers in this way. An animation video of the 3D structure would solve this problem and show clearly the separation between the two actin fibers.

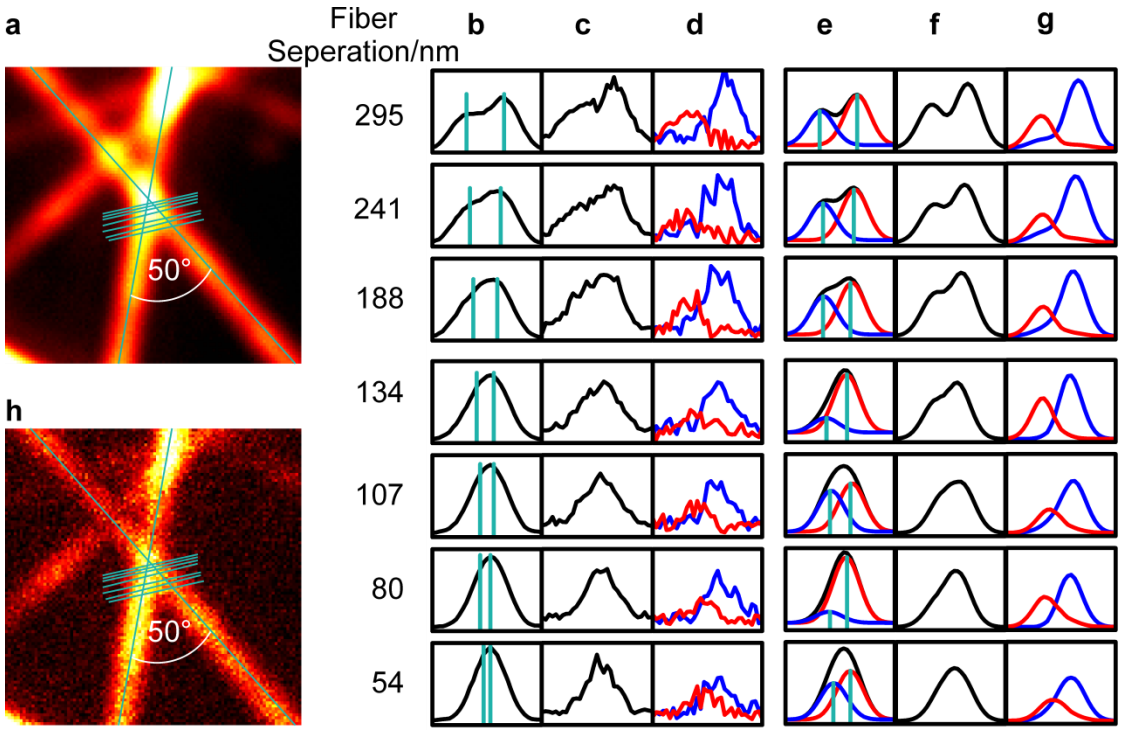

Figure 4-26: Diffraction limited image of two actin fibers differing by 50° in label polarization. Fitted cyan lines show the true positions for each actin fiber. The seven vertical profile plots were used for the data shown in b-g (a). Profile plot graphs of the diffraction limited image shown in a (b). Vertical cyan lines indicate the true position of the actin fiber in each profile plot (b). Corresponding profile plots of the modulation amplitude shown in h (c). Corresponding profile plots of the raw modulating data in two selected image time frames, both with maximum phase separation (d). The red and blue curves are single time frames. The fitted curves from the data shown in b, c and d with two modulating Gaussian functions demonstrate the theoretical curves without noise (e, f and g). The blue and the red curves in g are fitting curves corresponding to the curves shown in d. The blue and the red curves in e are the two Gaussian peak functions separated into two peaks. Their center is represented by cyan vertical lines showing the fitting position of the actin fibers. The modulation amplitude image, the true actin fiber positions and the profile plots correspond to a (h).

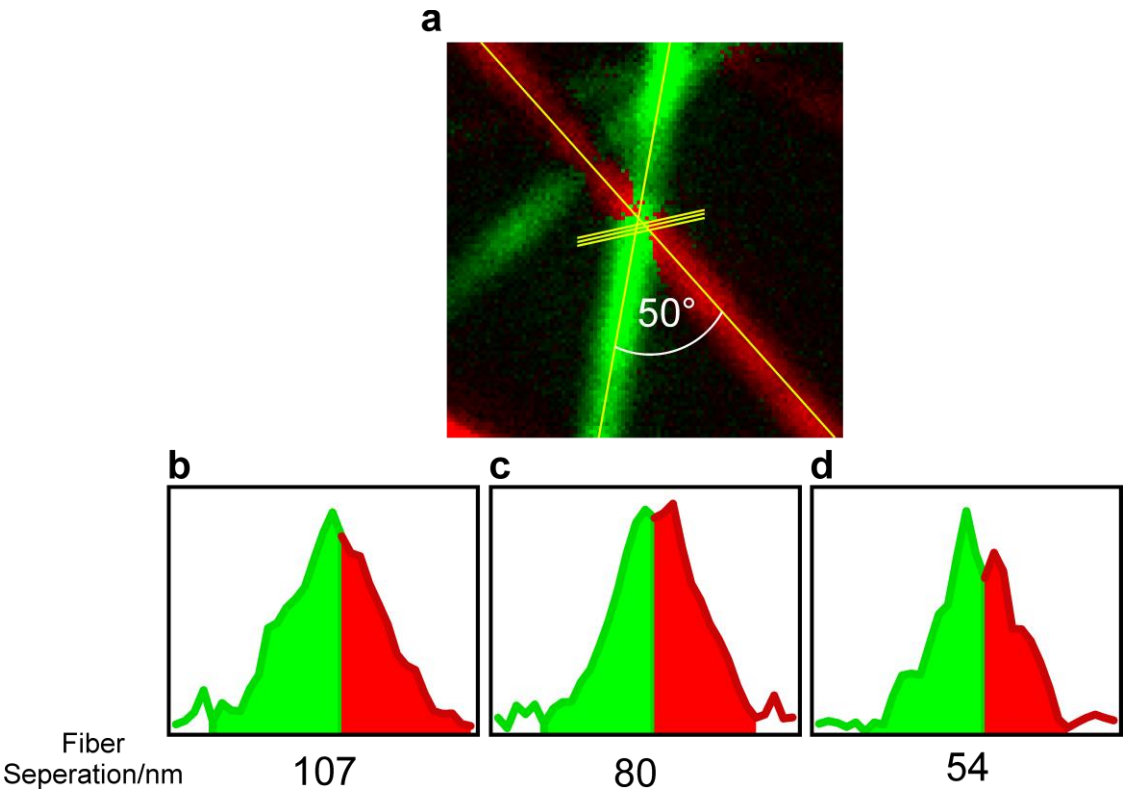

Figure 4-27: Two labeled actin fibers sample differing by ~50° in their direction and polarization are separated by their phases and demonstrated in two colors; red and green. The two crossing actin fibers show clearly two phases along each fiber in red and green until they completely overlap (a). Corresponding profile plots (yellow lines) with distances below the diffraction limit are plotted showing distinguishable two colors phase separation at 107 nm, 80 nm and 54 nm true fibers separation distances (b-d).

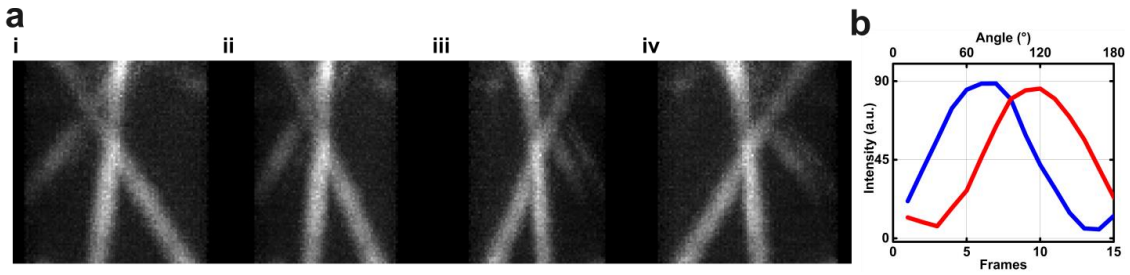

Figure 4-28: One period of 15 frames per 180° of rotation is constructed in 3D view. The view shows four different angles rotating around the y-axis (a). The angle between the actin fiber's direction and polarization is 50° and a separation can be observed in ii and iii. Plotting the intensity of each actin fiber against time frames (blue and red curves) indicates the phase shift of ~50° between the two actin fibers (b).

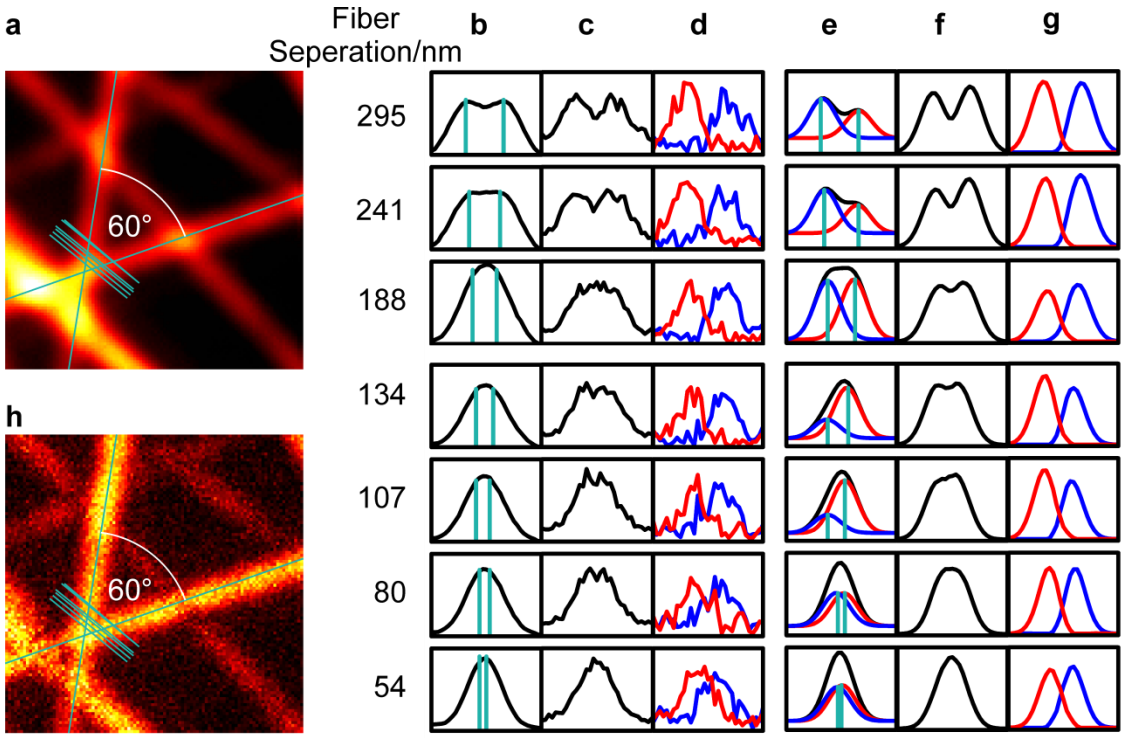

Figure 4-29: Diffraction limited image of two actin fibers differing by 60° in label polarization. Fitted cyan lines represent the true positions for each actin fiber and the seven vertical profile plots were used for the data shown in b-g (a). Profile plot graphs of the diffraction limited image shown in a (b). Vertical cyan lines indicate the true position of the actin fiber in each profile plot (b). Corresponding profile plots of the modulation amplitude shown in h (c). Corresponding profile plots of the raw modulating data in two selected image time frames, both with maximum phase separation (d). The red and blue curves are single time frames. Fitted curves of the data shown in b, c and d with two modulating Gaussian functions demonstrate the theoretical curves without noise (e, f and g). The blue and the red curves in g are fitting curves corresponding to the curves shown in d. The blue and the red curves in e are the two Gaussian peak functions separated into two peaks. Their center is represented by cyan vertical lines showing the fitting position of the actin fibers. The modulation amplitude image, the true actin fiber positions and the profile plots correspond to a (h).

The sample with labeling orientation and fiber direction difference of 60° was measured following the same procedure. The diffraction limited images demonstrate also that no separation below ~250 nm is possible (column Figure 4-29 b). Like with the exemplary data at 50°, separating the fibers from the modulation data only is very little. However, again distinct time frames of the modulating part of the raw data shows that the two fibers can be

differentiated even further, down to a distance of about 54 nm (column Figure 4-29 d). As well as, illustrating the fibers using their frequency information defined only by two colors shows that the phase separation distinguishes the two actin fiber clearly down to ~54 nm (Figure 4-30 b-d).

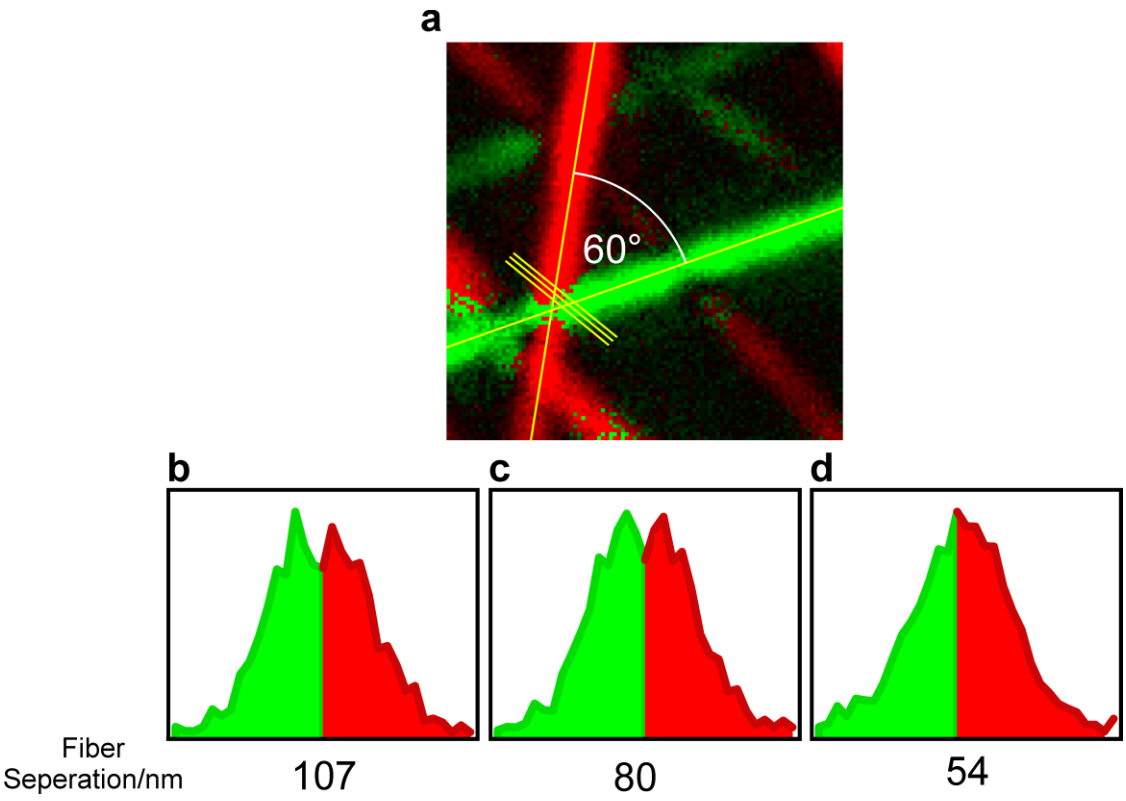

Figure 4-30: Two labeled actin fibers sample differing by ~60° in their direction and polarization are separated by their phases and demonstrated in two colors; red and green. The two crossing actin fibers show clearly two phases along each fiber in red and green until they completely overlap (a). Corresponding profile plots (yellow lines) with distances below the diffraction limit are plotted showing distinguishable two colors phase separation at 107 nm, 80 nm and 54 nm true fibers separation distances (b-d).

Fitting two Gaussian functions to diffraction limited images (column Figure 4-29 e), to the modulation amplitude data (column Figure 4-29 f) and to distinct time frames of the modulating part (column Figure 4-29 g) demonstrates theoretically optimum curves avoiding high peak noise und deviations. The fittings in column f show two peaks separation down to a

distance of about 130 nm and column g shows distinguishable peaks (red and blue) down to 54 nm.

The 3D image structure of 60° from one period of raw data shows clearly distinguishable actin fibers (Figure 4-31 a i-iv). Due to the high phase separation, it is possible to differentiate easily between the two actin fibers as shown in ii and iii. The phase shift of 60° is clearly observed with the red and blue curves (Figure 4-31b).

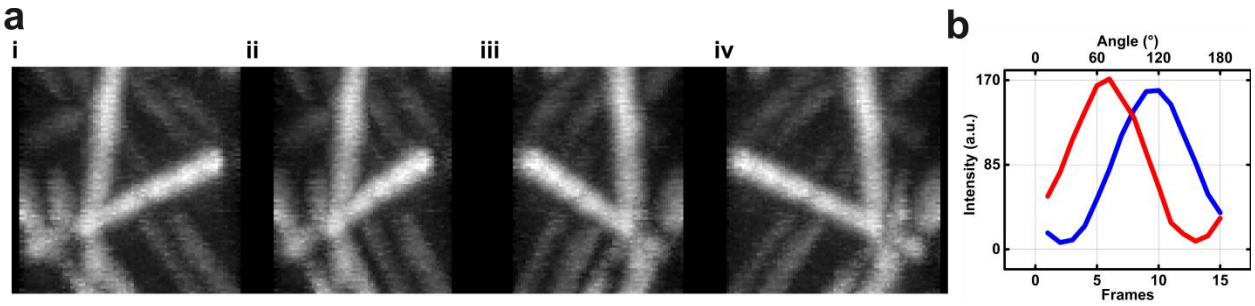

Figure 4-31: One period of 15 frames per 180° of rotation is constructed in 3D showing four different angle rotating around the y-axis (a). The angle between the actin fiber direction and polarization is 60° and a separation cannot be easily with images indicated. An animation video of the 3D structure can better show the separation. Plotting the intensity of each actin fiber against time frames (blue and red curves) shows a phase shift of ~60° (b).

The investigation of labeled actin filament continues examining labeling orientation and fiber direction differing by 70°following the same procedure. The diffraction limited images demonstrate also that no separation below ~250 nm is possible (column Figure 4-32 b). However, the modulation amplitude data demonstrates that the two fibers could be separated significantly below 250 nm but with high peak noises. In comparison with the theoretical curves demonstrated in column (f), the curves show that recording more periods, and thus reducing the noises, should allow to separate the fibers clearly from the amplitudes significantly further.

Actin fiber separation is more obvious at distances of 188 nm even if the noise is high. Distinct time frames of the modulating part of the raw data shows that the two fibers can be

differentiated even further, down to a distance of about 54 nm (column Figure 4-32 d). Similar to the previous samples, an illustration of the fibers using their frequency information defined only by two colors shows that the phase separation distinguishes the two actin fiber clearly down to ~54 nm (Figure 4-33 b-d).

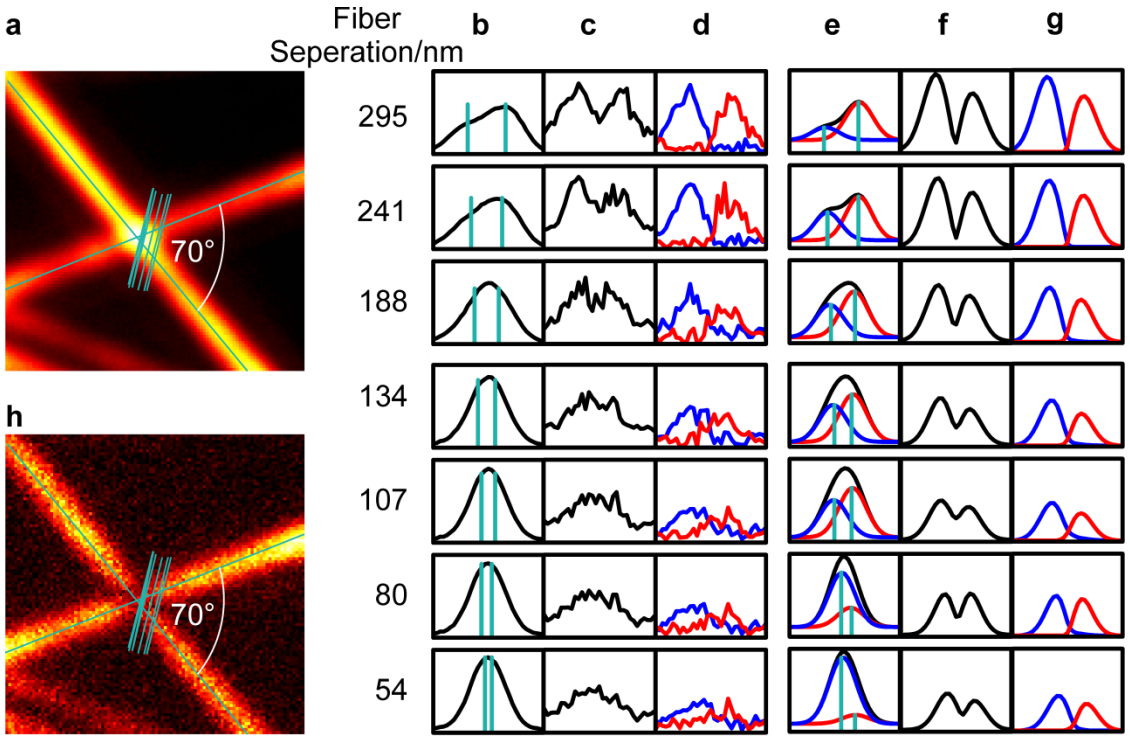

Figure 4-32: Diffraction limited image of two actin fibers differing by 70° in label polarization. Fitted cyan lines show the true positions for each actin fiber and the seven vertical profile plots were used for the data shown in b-g (a). Profile plot graphs of the diffraction limited image shown in a (b). Vertical cyan lines indicate the true position of the actin fiber in each profile plot (b). Corresponding profile plots of the modulation amplitude shown in h (c). Corresponding profile plots of the raw modulating data in two selected image time frames, both with maximum phase separation (d). The red and blue curves are single time frames. Fitted curves of the data shown in b, c and d with two modulating Gaussian functions demonstrate the theoretical curves without noise (e, f and g). The blue and the red curves in g are fitting curves corresponding to the curves shown in d. The blue and the red curves in e are the two Gaussian peak functions separated into two peaks. Their center is represented by cyan vertical lines showing the fitting position of the actin fibers. The modulation amplitude image, the true actin fiber positions and the profile plots correspond to a (h).

Fitting two Gaussian functions to diffraction limited images (column Figure 4-32 e), to the modulation amplitude data (column Figure 4-32 f) and to distinct time frames of the modulating part (column Figure 4-32 g) demonstrates theoretically optimum curves avoiding high peak noise und deviations. The fittings in column f show two peaks separation down to a distance of 54 nm and column g shows distinguishable peaks (red and blue) down to 54 nm.

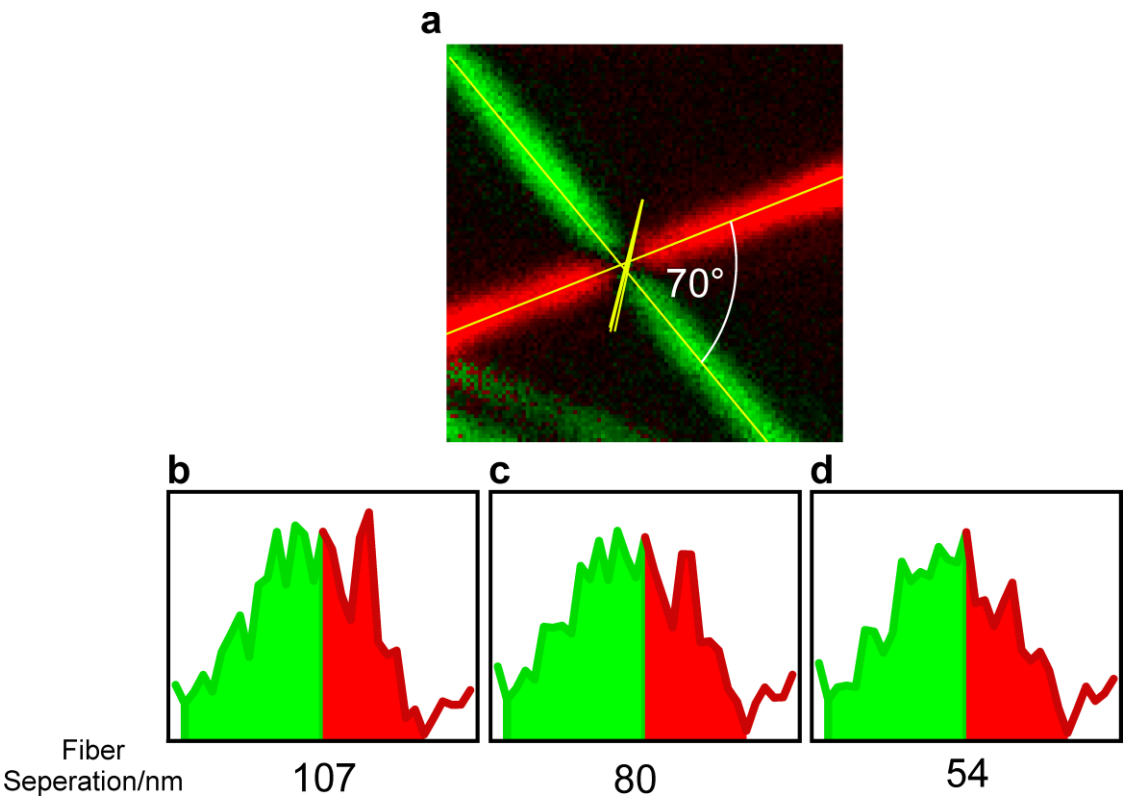

Figure 4-33: Two labeled actin fibers sample differing by ~70° in their direction and polarization are separated by their phases and demonstrated in two colors; red and green. The two crossing actin fibers show clearly two phases along each fiber in red and green until they completely overlap (a). Corresponding profile plots (yellow lines) with distances below the diffraction limit are plotted showing distinguishable two colors phase separation at 107 nm, 80 nm and 54 nm true fibers separation distances (b-d).

The 3D image structure of 70° from one period of raw data shows clearly distinguishable actin fibers (Figure 4-34 a i-iv). Due to the high phase separation, it is possible to differentiate easily between the two actin fibers as shown in ii and iii. The phase shift of 70° is clearly observed with the red and blue curves (Figure 4-34 b).

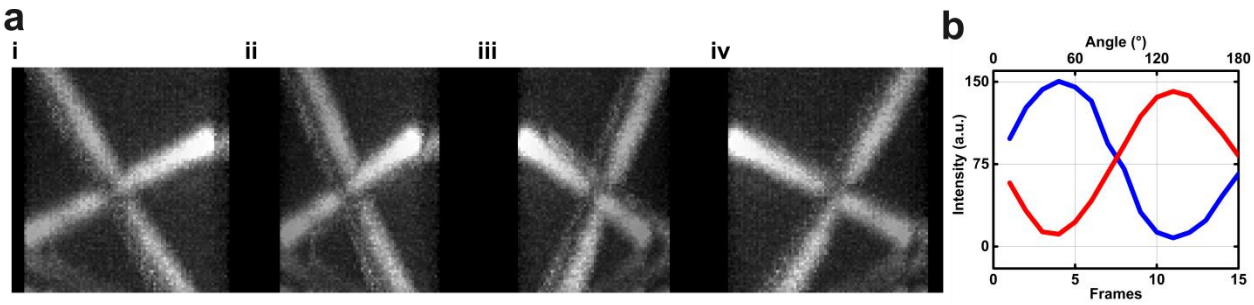

Figure 4-34: One period of 15 frames per 180° of rotation is constructed in 3D showing four different angle rotating around the y-axis (a). The angle between the actin fiber direction and polarization is 70° and a separation cannot be easily with images indicated. An animation video of the 3D structure can better show the separation. Plotting the intensity of each actin fiber against time frames (blue and red curves) shows a phase shift of ~70° (b).

Finally, the sample with a polarization difference of 80° was measured. The diffraction limited images demonstrate again in this case that no separation below ~250 nm is possible (column Figure 4-35 b). However, the modulation amplitude data demonstrated that the two fibers could be separated at least down to 134 nm with peak noises. Actin fiber separation is also observed at distances down to 80 nm, however, the peak noises are high. Still, the separation below 134 nm can deviate from true position as is clearly visible at a distance of 80 nm in column b. Distinct time frames of the modulating part of the raw data show that the two fibers can be differentiated down to a distance of about 54 nm (column Figure 4-35 d). As well here, an illustration of the fibers using their frequency information defined only by two colors shows that the phase separation distinguishes the two actin fiber clearly down to ~54 nm (Figure 4-36 b-d).

Fitting two Gaussian functions to diffraction limited images (column Figure 4-35 e), to the modulation amplitude data (column Figure 4-35 f) and to distinct time frames of the modu-

lating part (column Figure 4-35 g) shows the theoretical optimum curves avoiding high peak noise und deviations. The fittings in column f show a more convenient position than the raw data in c with a distance of 80 nm. Column g shows distinguishable peaks (red and blue) down to 54 nm.

The last 3D image structure of 80° from one period of raw data shows distinguishable actin fibers (Figure 4-37 a i-iv). Due to the high phase separation as in the 70° sample, it is possible to differentiate easily between the two actin fibers, as shown in iii and iv. The phase shift of 80° is clearly observed with the red and blue curves (Figure 4-37 b).

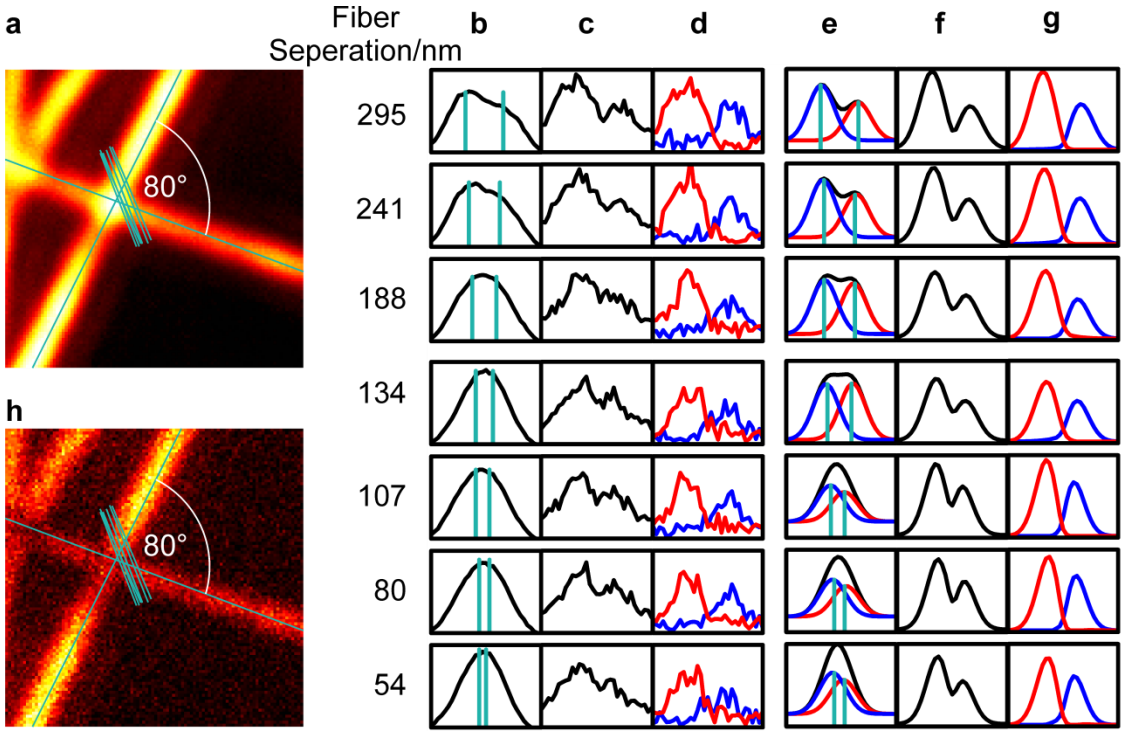

Figure 4-35: Diffraction limited image of two actin fibers differing by 80° in label polarization. Fitted cyan lines show the true positions for each actin fiber and the seven vertical profile plots were used for the data shown in b-g (a). Profile plot graphs of the diffraction limited image shown in a (b). Vertical cyan lines indicate the true position of the actin fiber in each profile plot (b). Corresponding profile plots of the modulation amplitude shown in h (c). Corresponding profile plots of the raw modulating data in two selected image time frames, both with maximum phase separation (d). The red and blue curves are single time frames. Fitted curves of the data shown in b, c and d with two modulat-

ing Gaussian functions demonstrate the theoretical curves without noise (e, f and g). The blue and the red curves in g are fitting curves corresponding to the curves shown in d. The blue and the red curves in e are the two Gaussian peak functions separated into two peaks. Their center is represented by cyan vertical lines showing the fitting position of the actin fibers. The modulation amplitude image, the true actin fiber positions and the profile plots correspond to a (h).

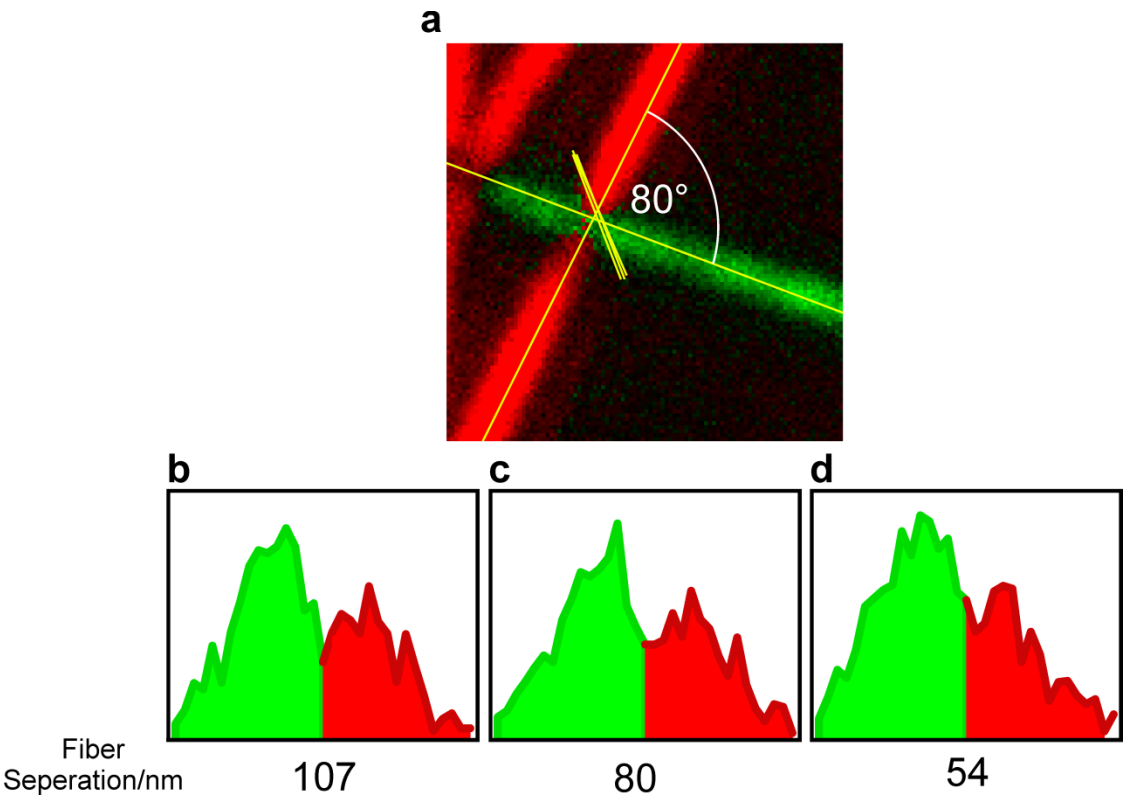

Figure 4-36: Two labeled actin fibers sample differing by ~80° in their direction and polarization are separated by their phases and demonstrated in two colors; red and green. The two crossing actin fibers show clearly two phases along each fiber in red and green until they completely overlap (a). Corresponding profile plots (yellow lines) with distances below the diffraction limit are plotted showing distinguishable two colors phase separation at 107 nm, 80 nm and 54 nm true fibers separation distances (b-d).

All the investigated homogeneously densely labeled samples of phalloidin labelled actin filament demonstrated that with the diffraction limited image, no separation below ~250 nm is possible (column b). The raw modulation data however, showed that separation below the diffraction limit is possible at distances down to 134 nm, for most of the samples (column c). Distinct time frames of the modulating part and two color phase separation of the

raw data showed every time that the two fibers can be differentiated down to a distance of about 54 nm (blue and red curves, column d). The corresponding fitting curves showed how the separation would theoretically appear without noise and with less deviation. Therefore, it is obvious that modulation information can discern homogeneous densely labelled structures at distances down to 138 nm spatially and down to 54 nm by their phases.

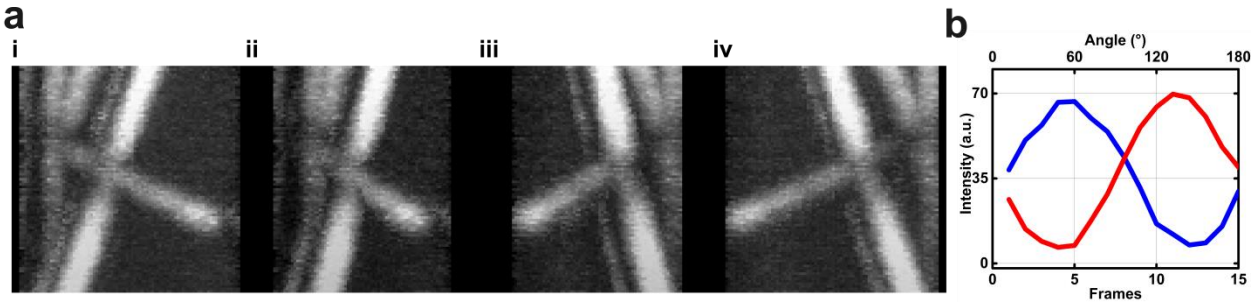

Figure 4-37: One period of 15 frames per 180° of rotation is constructed in 3D showing four different angle rotating around the y-axis (a). The angle between the actin fiber direction and polarization is 70° and a separation cannot be easily with images indicated. An animation video of the 3D structure can better show the separation. Plotting the intensity of each actin fiber against time frames (blue and red curves) shows a phase shift of ~70° (b).

4.1.6 GUVs Imaging

Giant Unilamellar Vesicles (GUVs) are liposomes with a diameter ranging from several micrometers up to one hundred micrometer. GUVs become increasingly widely used for addressing physical and biochemical properties of the cell membrane. Their size, which is usually above the diffraction limit, allows biologists to study and observe the GUVs with conventional light microscopy techniques (fluorescence-related microscopy), such as confocal microscopy and wide-field microscopy. The advantage of fluorescence microscopy over other approaches is the ability to spatially resolve any phase available in the GUV membrane by targeting the different fluorescent markers specific to those phases.

The visualized GUVs in this work were labeled with Texas Red-DHPE dye which has a maximum absorption at 584 nm and a maximum emission at 608 nm. The wavelength

used for two-photon excitation was 740 nm and the setup used for these measurements is shown in Figure 3-3. The DOE (Diffractive Optical element) provides 9x9 focused points (81 focused points) of the 740 nm laser beam (Figure 4-38 a). The diameter of these points depends on the telescope used after the DOE. The diameter could be enlarged or diminished by the telescope. In order to achieve two-photon excitation, high photon density is required in the focal volume because two photons must be absorbed simultaneously. Therefore, short laser pulses (140 fs), with a high repetition rate (80 MHz) and around 3 Watt averaged power, were used. In addition, the microscope objective, which focuses the excitation beam down to a very small diameter (minimum is around 300 nm diameter), increases the volume density in the focal volume and thus allows for two-photon absorption.

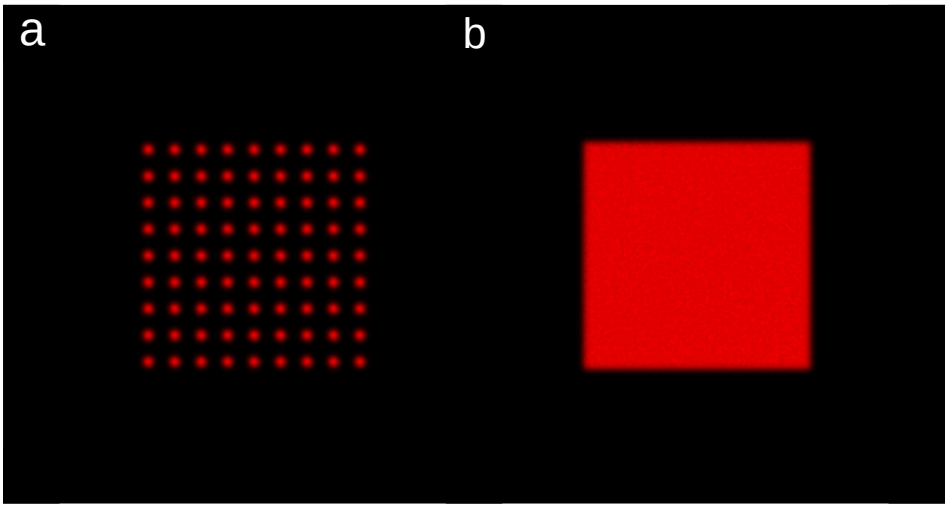

Figure 4-38: Two-photon excitation using DOE to provide 9x9 focused points in the focal volume (a). A piezo-scanner which moves three steps in the X-direction and three steps in the Y-direction (nine steps in total) is used to illuminate the focal area homogeneously (b).

A piezo-scanner was used to move the 9x9 focused point three steps in X-direction and three steps in Y direction to illuminate the whole dark area between the spots. A total movement of nine steps was then recorded within one frame using the EMCCD camera. This resulted in a homogenous illumination of the focal area (Figure 4-38 b). The laser beam's averaged power is then distributed equally over the whole focal area.

All measured GUV samples have shown modulated fluorescent signals. The modulated signal is very obvious in the averaged phase images (Figure 4-39 **a**) where fluorescence intensity distribution changes in each step. Plotting the angle of rotation α against fluorescence intensity for one pixel or several pixels of each frame shows a modulated signal which fits to the sine–squared function of the angle α (Figure 4-39 b).

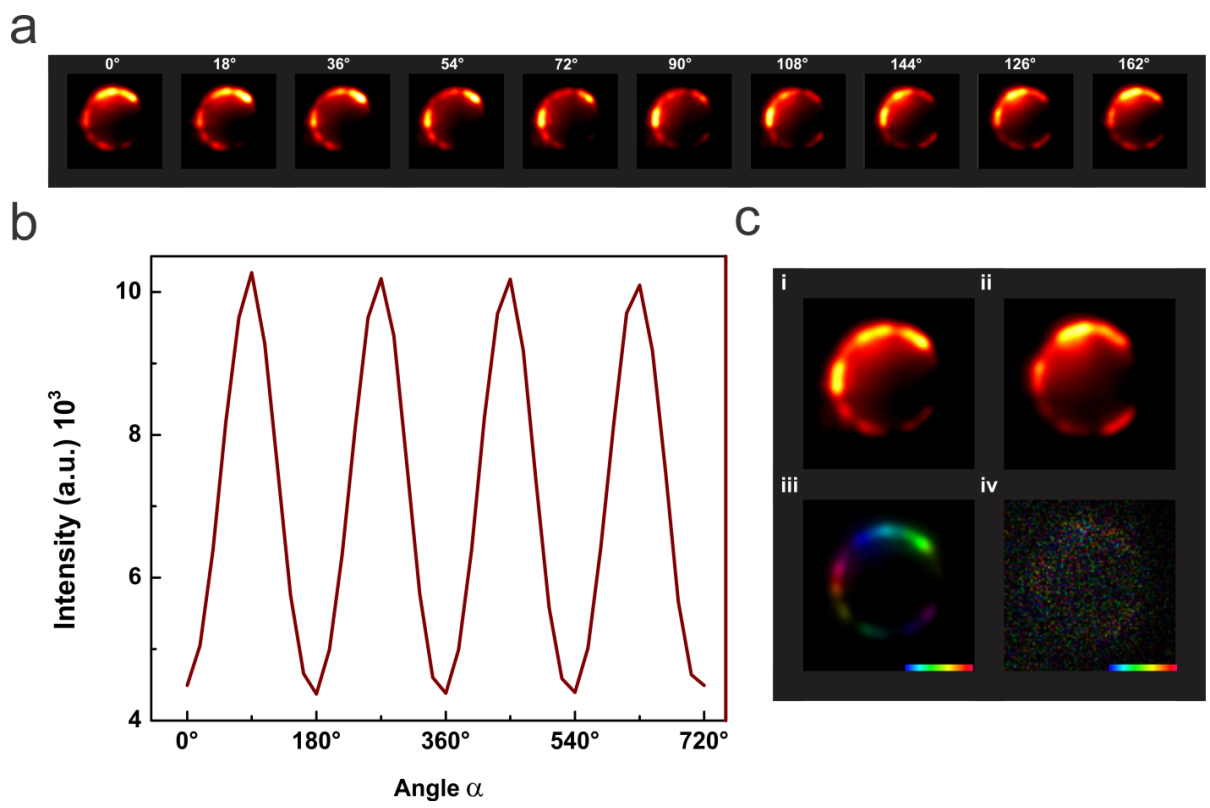

Figure 4-39: Phase average images in one period for one GUV labeled with Texas Red-DHPE dye (a). Modulated signal of 9 pixels area of the modulated stacked images shows a sine–squared function (b). Average image of modulated stacked images of GUV labeled with Texas Red-DHPE dye (c i), Average image of non-modulated stacked images of the same GUV sample and position (c ii), Color coded image produced from the Fourier transform amplitude and phase of the modulated stacked images of GUV labeled with Texas Red-DHPE dye showing different colors (different phases are detected) (c iii). Color coded image produced from the Fourier transform amplitude and phase of the non-modulated stacked images of the same GUV sample and position showing no different colors (no phases are detected) (Figure 4-39c iv).

In order to illustrate the difference between the modulated stacked images and the non-modulated stacked images, GUVs were recorded while rotating the half-wave plate. The same positions previously recorded were recorded again without rotating the half-wave plate (Figure 4-39 c). Using the Fourier transform function to determine the different phases in a GUV image results in a color coded image with a certain color for each phase. Figure 4-39 (c i) shows an average image from the modulated stacked images and its phase color coded image (Figure 4-39 c iii). The average image from the modulated stacked images and the average image from the non-modulated stacked images have no differences, other than the slight differences in fluorescence intensity in some parts of the GUV image (Figure 4-39 c i & ii). This difference is due to bleaching since the non-modulated stacked images were measured for two minutes and were measured after the modulated stacked images. On the other hand the Fourier transform image of the modulated image differs from the Fourier transform image of the non-modulated image. The Fourier transform image of the modulated image clearly shows different phases presented with color-coded image (Figure 4-39 c iii). However, the Fourier transform image of the non-modulated image shows no phases detected at all. Consequently, no colors were detected (Figure 4-39 c iv).

Many GUVs samples were measured in the same way and all have shown similar modulation signals. All of the GUVs samples measured with the Polarization Demodulation technique have shown different phases clearly illustrated with different colors. Texas Red-DHPE dye was used to label these GUVs but it did not cover or bind to the entire surface area of the GUVs. The area which was not labeled with Texas Red-DHPE dye are missing from the GUVs structure and appear simply as dark shadows (Figure 4-40 **a** & **c**). In the center of the measured GUVs, a part of the background appears clearly than the remaining background. This is to be expected when the measured sample is thick or has a spherical shape. The modulation is very obvious in the focal area and appears on the membrane of the GUVs samples.

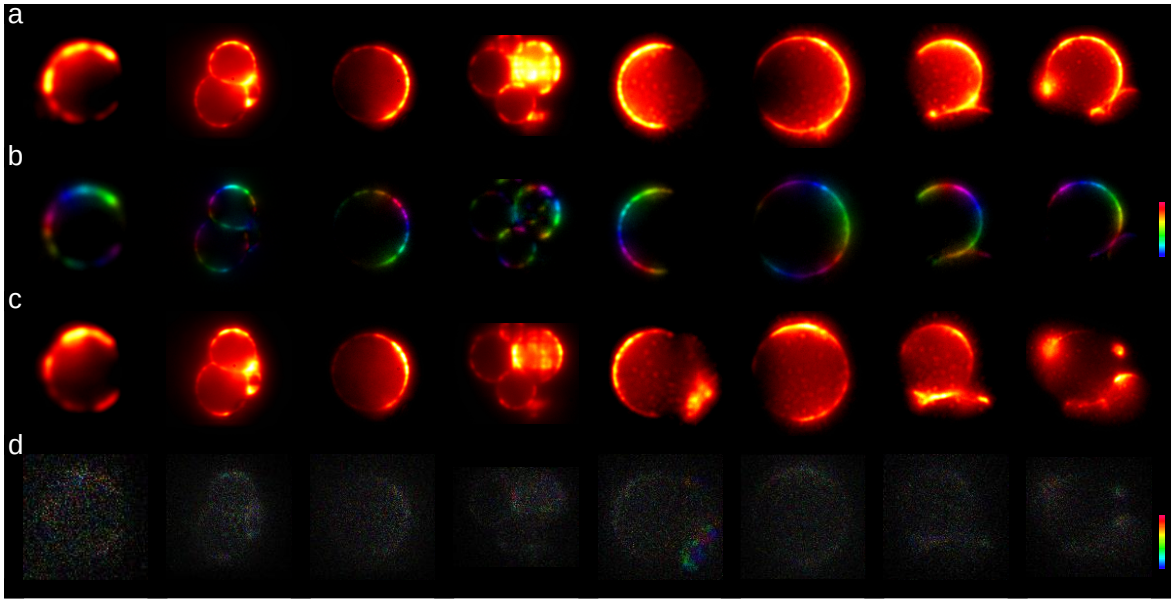

Figure 4-40: Average image from modulated stacked images of 8 GUVs samples labeled with Texas Red-DHPE dye (a). Color coded images produced from the Fourier transform amplitude and phase of the modulated stacked images of the 8 GUVs samples labeled with Texas Red-DHPE dye. The different colors represent the different phases that were detected (b). Average image from non-modulated stacked images of the same 8 GUVs samples and positions (c). Color coded images produced from the Fourier transform amplitude and phase of the unmodulated stacked images of the same 8 GUVs samples and positions showing no different colors (no phases are detected) (d).

Fourier transform function was applied to those modulated stacked images to locate the different phases of the GUVs' modulated structure. The results were color coded images of the GUVs samples (Figure 4-40 **b**) which indicate the modulated structure of the labeled membrane. Any unmodulated structures, like the background in the center of the GUVs' structure, have been removed. The positions of the GUVs samples were measured again but without modulation. The rotatable half waveplate was prevented from rotating and the result was just a constant linear polarized light that excite the GUVs samples. The average stacked images from the modulated samples are slightly different from the unmodulated samples. The fluorescence intensity in some parts of the unmodulated GUVs' structures is less than those same parts of the modulated GUVs' structures (Figure 4-40 **a** and **c**). This is due to the fact that the linear polarized light fully excites the dyes with parallel dipole

moments. The rest is just partially excited or not excited at all, depending on the angle between the dipole moment of the dye and that of the polarized light. Applying the Fourier transform function on the unmodulated stacked images of the GUVs samples results in images with no phases detected and therefore no clear colors appeared in these images (Figure 4-40 d).

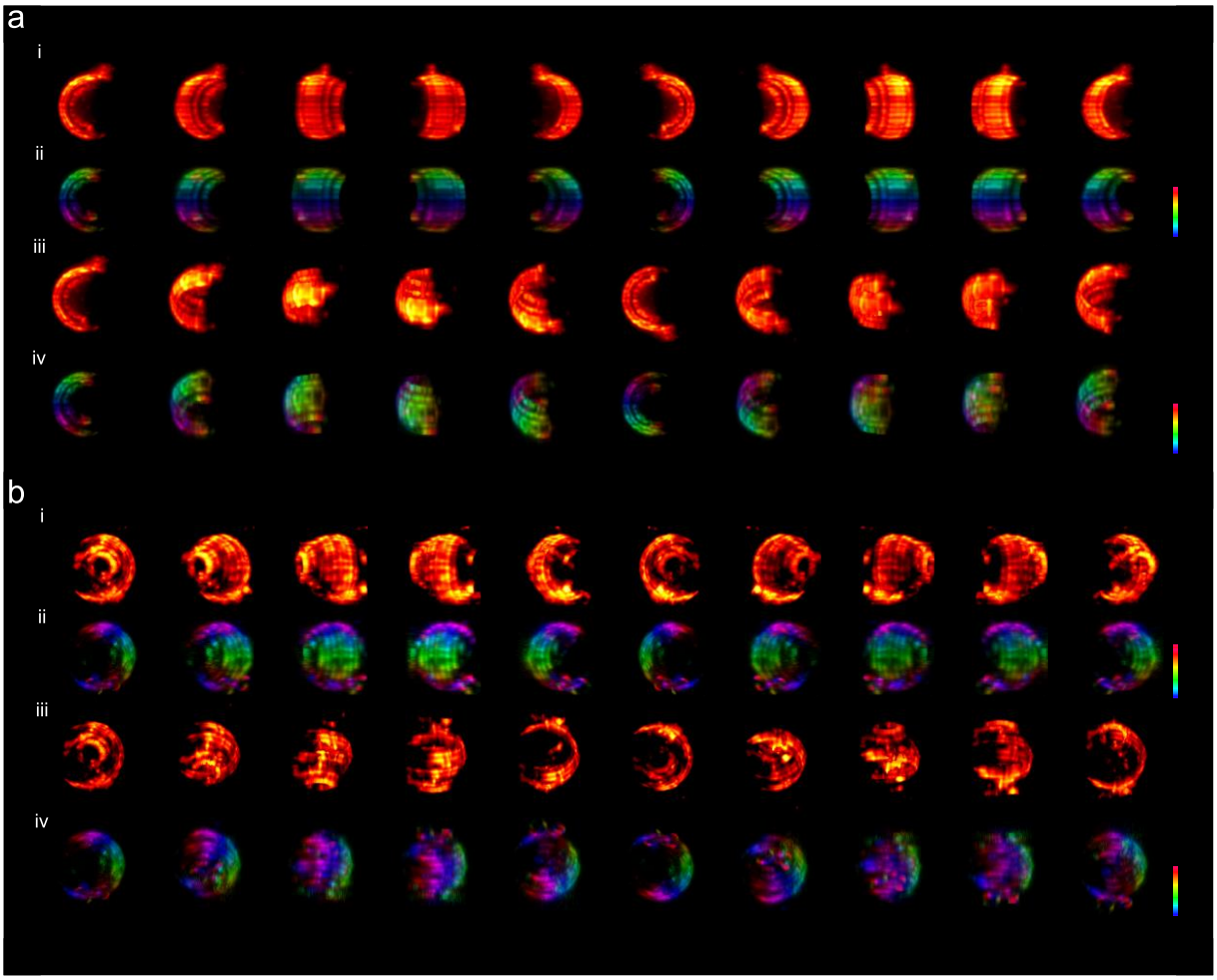

Figure 4-41: Two examples of 3-dimentional view of GUVs samples (a rotates on x-axis and b rotates on y-axis). Average 3D image from modulated stacked images labeled with Texas Red-DHPE dye rotating around y-axis in 10 steps (a and b, i). Average 3D image from modulated stacked images labeled with Texas Red-DHPE dye rotating around x-axis in 10 steps (a and b, iii). 3D Color cod-

ed images produced from the Fourier transform amplitude and phase of the modulated stacked images of the 3D GUVs samples showing the same color distribution through out the whole sphere (different phases are detected in x-y directions but similar phases are detected in z- direction). They rotate around x-axis in 10 steps (a and b ii). The same previous GUV ample but rotating around the y-axis in 10 steps (a and b iv).

GUVs were labeled with Texas Red-DHPE dye. It was observed that GUVs samples with several GUVs in the field of view showed the same color cod distribution as illustrated in Figure 4-40. For example, the second column in Figure 4-40 demonstrates a GUV sample containing two vesicles. The color coded image shows the same color distribution for both vesicles. The same effect is observed in Figure 4-40 column 4. It is concluded that Texas Red-DHPE molecules are perpendicularly attached to the GUV surface; therefore Texas Red-DHPE molecules are having always the same angle in respect to the attached surface.

Two GUV samples were measured in three dimensions in order to depict the phase distribution across the whole sphere. The measurement was carried out by scanning in directions x-y for 300 frames. The scan then moved one step in direction Z, corresponding to 500 nm. The result was as expected; each slice has almost the exact same color distribution as the other slices in the other GUV sample (Figure 4-41). The GUVs samples were prepared in high density so that they settle in the bottom of the Lab-tek chamber. Some small GUVs were observed moving in the sample solution while a normal sized GUV sample was measured. The small GUVs were diffusing in the sample solution relatively slow where the intended standard sized GUV sample or unit to be measured was static.

The rotatable half-wave plate completes a full rotation of the polarized light in 33 milliseconds. The small GUVs were diffusing in this time scale. It was possible to track one small GUV while it was moving during measuring (Figure 4-42). A modulation signal was observed from the diffusing GUV. The diffusing GUV was visualized with Furrier transform images as demonstrated in Figure 4-42 (**ii**). Each position was measured in one period of rotation within 33 milliseconds and after this time the GUV moved to another position. This

example provides a clear evidence on the fact that samples of dynamic fluorescent dyes mobility can be modulated. With an advanced CCD camera and with enough detected photons it would be possible to observe modulation from faster samples.

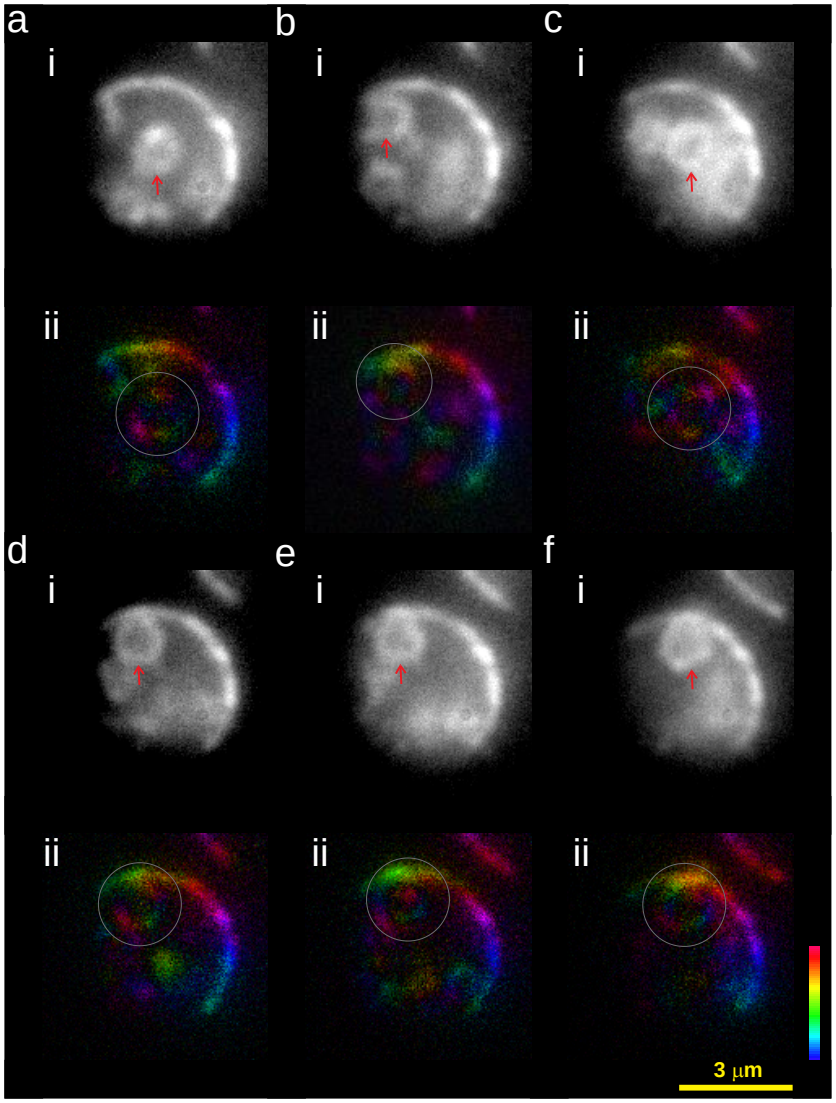

Figure 4-42: Diffusing small GUV unit which remains constant just for 33 ms. That is sufficient to complete one period of linear polarized light rotation. Averaged image from 10 frames showing different positions of the small diffusing GUV marked with a red arrow (a,b,c,d,e and f, i). Frequency domain visualization (Fourier transform) of each position indicates different colors from the diffusing GUV unit which corresponds to the modulation signal marked with grey circles (a,b,c,d,e and f, ii).

4.1.7 Fixed Nerve Cell Imaging

Dendritic spines are neuronal actin-rich protrusions which contain neurotransmitter receptors and function as major receptor of excitatory synaptic input. Dendritic spines play a major role in neural processing and their morphology is different. The importance of spines comes from which any changes in spine size or density will affect the strength of synaptic transmission. Scientists indicated that dendritic spines undergo morphological reformation during any development in sensory stimuli or memory.

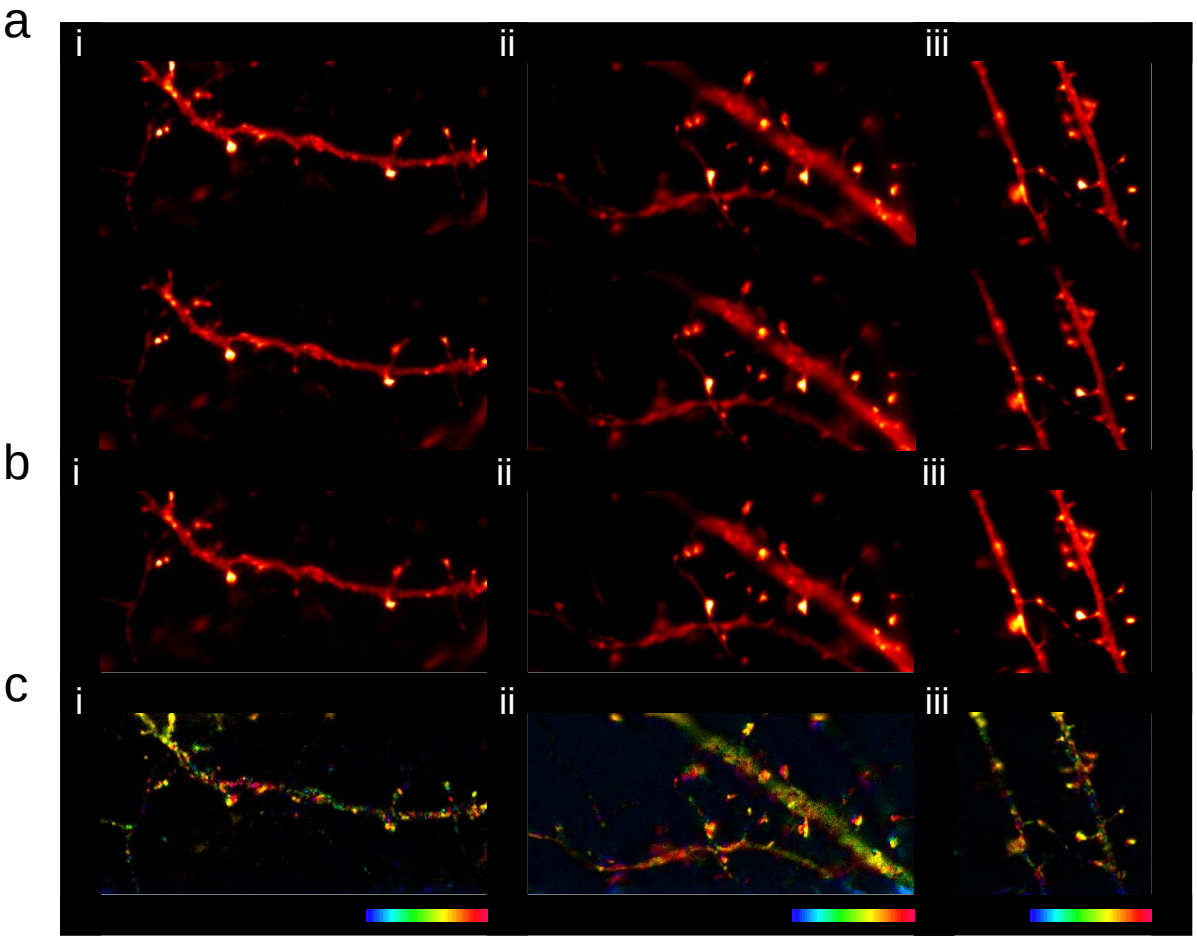

Figure 4-43: Three examples of nerve cells labelled with LifeAct-eGFP measured with the Polarization Demodulation technique setup and with splitting the fluorescent light to perpendicular linear polarized light and parallel linear polarized light and detected on the EMCCD camera (a, i, ii and iii). The two stacked images are merged together forming one averaged stacked image (b, i, ii and iii).

Corresponding color coded images produced from the Fourier transform amplitude and phase of the modulated merged stacked images of the nerve cell samples showing diverse of colors (different phases are detected) (c, i, ii and iii).

Two types of targeted nerve cells were measured and visualized with the Polarization Demodulation setup. The first type was a membrane-targeted of farnesylated form of eGFP sample. The second type was a construct expressing LifeAct-eGFP targeting actin filaments in the cytoskeleton. The maximum excitation wavelength of the eGFP is 488 nm and its maximum emission is 509 nm. The nerve cell samples were measured using the setup with the Sapphire 488-50 laser. The nerve cells were then detected either with one channel (one image) on the EMCCD camera or with two channels (two images) on the EMCCD camera. Three different nerve cell samples were measured with the Polarization Demodulation technique and polarizing splitting in the detection path (Figure 4-43 a i, ii and iii). The measured stacked images were subsequently merged into one channel and averaged (Figure 4-43 b i, ii and iii). Applying Fourier transform on these merged stacked images resulted in a color coded image, showing the modulation signals detected from each sample (Figure 4-43 c i, ii and iii). The dendritic spines have high labeling densities. It was obvious that different modulation signals are detected, with a range of different colors distributed heterogeneously along the measured sample, as depicted in Figure 4-43 (c i, ii and iii). Three more samples of nerve cells were also measured using the the setup with a Sapphire 488-50 laser. However this time, they were detected with just one channel (one image) (Figure 4-44 a i, ii and iii). Likewise, these samples show a variation of colors in the Fourier transform images (Figure 4-44 b i, ii and iii). This clearly proves that it is possible to detect modulation signals from heterogeneously samples of high labeling densities. It has been shown that different phases of these modulation signals can be used to distinguish, for example, the spine apparatus from its surrounding membrane even when this is not possible in its corresponding diffraction limited images.

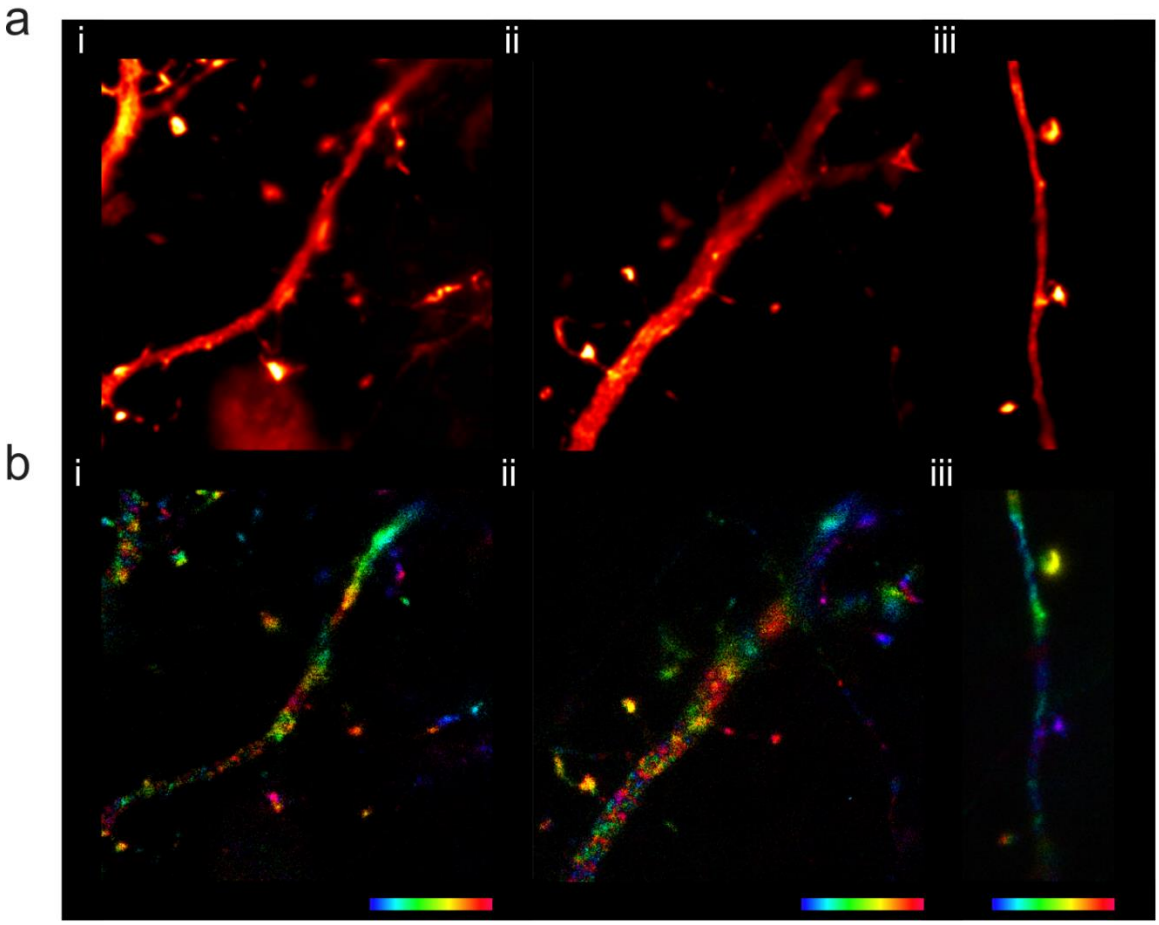

Figure 4-44: Averaged stacked images of three different nerve cells samples labelled with F-eGFP measured with the Polarization Demodulation setup (a i, ii and iii). Corresponding color coded images produced from the Fourier transform amplitude and phase of the modulated merged stacked images of the nerve cell samples showing different colors (different phases are detected) (b, i, ii and iii).

5 Summary and Discussion

In this work, the additional information contained in the orientation of fluorescence markers labelled to various structures was explored. A large range of differently labelled samples was investigated: Samples of very low labelling density (single molecules on a coverslip) or of higher label densities (phalloidin labelled actin filaments, Texas Red-DHPE labeled GUVs or EGFP labelled hippocampal neurons). Samples of rather heterogeneous label orientations (single molecules, EGFP labelled hippocampal neurons) were compared to samples of rather homogeneous label orientation with close orientation structure relationships (phalloidin labelled actin filaments and Texas Red-DHPE labeled GUVs). In addition, samples of rather high label mobility (Texas Red-DHPE labeled GUVs) were compared to samples with rather fixed labelling (single molecules, fixed EGFP labelled hippocampal neurons).This large range of investigated samples gave very valuable insights in the information content provided by molecular orientation as well as possibilities and limitations to use this information to discern labelled structure on different length scales, including sub-diffractional distance regimes.

To investigate these samples a simple and thus robust set-up was designed based on a wide-field light microscopy setup and a rotating waveplate, which is synchronized and accurately controlled, with a wide-field light microscopy setup. The synchronization is necessary in order to repeatedly and accurately measure the exact frame with its corresponding polarizing light angle. The advantage of modulating the excitation polarization in a wide field system rather than differentiation of the emission polarization is the intrinsic spatial stability in the optical detection path-way. This prevents shifting in the detected image when the polarization is changed in the detection path or when two images of different polarization are imaged onto different parts of the CCD camera. The system can work with all types of standard lasers whether it was a constant wave laser or a pulsed laser. The excitation intensity used was within the standard range of excitation intensities similar to wide-field and confocal Microscopies. No special optics or complicated alignments were needed for SPoD system.

It was demonstrated in this work that when two single molecules overlap spatially but differ in their orientations it was possible to distinguish between them by their phases. The separability depends on the relative orientation but longer acquisition times allows in principle to separate molecules of similar orientations at subdiffractional distances. In future applications, an extension to 3-D orientation measurements will significantly enhance the separability by polarization since the probability of similar orientations in three dimensions is much smaller than in two dimensions. In biological samples of higher labeling density often structurally preferred average orientations of several fluorescent markers were detected resulting in measurable polarization differences of different structures in the samples.

Samples of linear actin filaments that have a well-defined fluorescent markers orientation that persist along the actin fiber were systematically investigated. A series of profile plots of the modulation amplitudes in the crossing region of fibers demonstrated that subdiffractional details can be observed down to a distance of $\sim$150 nm in actin fibers of various relative polarization angles. When considering specific images at a certain phases (time frames) in the averaged signals of the modulating, separations down to $\sim$60 nm are possible. This is because the modulation amplitude in a certain frame reaches its maximum of one actin Fiber and the maximum modulation amplitude of the second actin fiber appears at another frame (time) which result in a good differentiation between the two actin fibers. Actin fibers with an angle below 10° in between show a worse separation below 150 nm because both actin fibers have a small difference in their orientation. Fitting theoretical functions to the observed data confirm a separation down to 150 nm in the modulation amplitudes and down to 60 nm in certain time frames of the modulated part of the data. Also in samples with more heterogeneously labelled orientation details of the underlying structures could be discerned by their orientation. In a spine head, for instance, the membranes in the apparatus are often aligned in parallel sheets. This orientation information can in principle be used to identify and localize the spine apparatus even on subdiffractional length scales when labelling with a strong structure-orientation relationship is chosen. In general, it was often observed that the average orientation of the fluorescent markers maintains longer when it is attached to a rigid structure. In such cases, averaging the modulation over several periods is of advantage for reducing background and noise in measured samples to

achieve sufficient and better modulation signal. Even if a high density of randomly oriented labels is present there will still be a residual polarization and modulation with modulation amplitude being inversely proportional to the number of molecules N_{mol}.

In summary, the structure-polarization relationship of fluorescently labelled samples provide very valuable additional information about the underlying structures and enables in principle to separate subdiffractional details even down to distances of about 50-60 nm. In future applications the extension to determining the polarization in all three dimensions will greatly enhance the additional information gain and the separability of subdiffractional details. Faster detection schemes will extend the application range to samples which are currently not accessible by this approach due to high orientational mobility. To this end, extending the analysis to correlational measurements of rotational diffusion of structurally hindered fluorescence markers will be of high potential for future development.

Note: Part of the results shown in this work was published by Nature Methods journal [1,60].

References

1 Hafi, N., Grunwald, M., van den Heuvel, L. S., Aspelmeier, T. *et al.* Fluorescence nanoscopy by polarization modulation and polarization angle narrowing. *Nat Meth* **11**, 579-584, (2014).

2 Brand, C., Meerts, W. L. & Schmitt, M. How and Why Do Transition Dipole Moment Orientations Depend on Conformer Structure? *The Journal of Physical Chemistry A* **115**, 9612-9619, (2011).

3 Courjon, D. *History of Near-field Optics*. doi:10.1142/9781848161351_0001

10.1142/9781848161351_0001 (PUBLISHED BY IMPERIAL COLLEGE PRESS AND DISTRIBUTED BY WORLD SCIENTIFIC PUBLISHING CO., 2003).

4 Abbe, E. Beiträge zur Theorie des Mikroskops und der mikroskopischen Wahrnehmung. *Archiv f. mikrosk. Anatomie* **9**, 413-418, (1873).

5 Lauterbach, M. Finding, defining and breaking the diffraction barrier in microscopy - a historical perspective. *Optical Nanoscopy* **1**, 8, (2012).

6 Rayleigh, L. XV. On the theory of optical images, with special reference to the microscope. *Philosophical Magazine Series 5* **42**, 167-195, (1896).

7 Betzig, E., Patterson, G. H., Sougrat, R., Lindwasser, O. W. *et al.* Imaging Intracellular Fluorescent Proteins at Nanometer Resolution. *Science* **313**, 1642-1645, (2006).

8 Hess, S. T., Girirajan, T. P. K. & Mason, M. D. Ultra-High Resolution Imaging by Fluorescence Photoactivation Localization Microscopy. *Biophysical journal* **91**, 4258-4272, (2006).

9 Giepmans, B. N. G., Adams, S. R., Ellisman, M. H. & Tsien, R. Y. The Fluorescent Toolbox for Assessing Protein Location and Function. *Science* **312**, 217-224, (2006).

10 Huang, B., Babcock, H. & Zhuang, X. Breaking the Diffraction Barrier: Super-Resolution Imaging of Cells. *Cell* **143**, 1047-1058, (2010).

11 Hell, S. W. Far-Field Optical Nanoscopy. *Science* **316**, 1153-1158, (2007).

12 Gustafsson, M. G. L. Nonlinear structured-illumination microscopy: Wide-field fluorescence imaging with theoretically unlimited resolution. *Proceedings of the National Academy of Sciences of the United States of America* **102**, 13081-13086, (2005).

13 Hell, S. W. Microscopy and its focal switch. *Nat Meth* **6**, 24-32, (2009).

14 Huang, B., Bates, M. & Zhuang, X. Super-Resolution Fluorescence Microscopy. *Annual Review of Biochemistry* **78**, 993-1016, (2009).

15 Lippincott-Schwartz, J. & Manley, S. Putting super-resolution fluorescence microscopy to work. *Nat Meth* **6**, 21-23, (2009).

16 Hell, S. W. & Wichmann, J. Breaking the diffraction resolution limit by stimulated emission: stimulated-emission-depletion fluorescence microscopy. *Opt. Lett.* **19**, 780-782, (1994).

17 Rust, M. J., Bates, M. & Zhuang, X. Sub-diffraction-limit imaging by stochastic optical reconstruction microscopy (STORM). *Nat Meth* **3**, 793-796, (2006).

18 Dertinger, T., Colyer, R., Iyer, G., Weiss, S. & Enderlein, J. Fast, background-free, 3D super-resolution optical fluctuation imaging (SOFI). *Proceedings of the National Academy of Sciences* **106**, 22287-22292, (2009).

19 Gustafsson, M. G. L. Surpassing the lateral resolution limit by a factor of two using structured illumination microscopy. *Journal of Microscopy* **198**, 82-87, (2000).

20 Geisler, C., Hotz, T., Schönle, A., Hell, S. W. *et al.* Drift estimation for single marker switching based imaging schemes. *Opt. Express* **20**, 7274-7289, (2012).

21 Hell, S. W. Toward fluorescence nanoscopy. *Nat Biotech* **21**, 1347-1355, (2003).

22 Heintzmann, R., Jovin, T. M. & Cremer, C. Saturated patterned excitation microscopy?a concept for optical resolution improvement. *J. Opt. Soc. Am. A* **19**, 1599-1609, (2002).

23 Dobrucki, J. W. *Fluorescence Microscopy*. in *Fluorescence Microscopy* 10.1002/9783527671595.ch3 97-142 (Wiley-VCH Verlag GmbH & Co. KGaA, 2013).

24 Lewis, A., Isaacson, M., Harootunian, A. & Muray, A. Development of a 500 Å spatial resolution light microscope: I. light is efficiently transmitted through λ/16 diameter apertures. *Ultramicroscopy* **13**, 227-231, (1984).

25 Pohl, D. W., Denk, W. & Lanz, M. Optical stethoscopy: Image recording with resolution lambda/20. *Applied Physics Letters* **44**, 651-653, (1984).

26 Lereu, A. L., Passian, A. & Dumas, P. Near field optical microscopy: a brief review. *International Journal of Nanotechnology* **9**, 488-501, (2012).

27 Hecht, B., Sick, B., Wild, U. P., Deckert, V. *et al.* Scanning near-field optical microscopy with aperture probes: Fundamentals and applications. *The Journal of Chemical Physics* **112**, 7761-7774, (2000).

28 Courjon, D., Sarayeddine, K. & Spajer, M. Scanning tunneling optical microscopy. *Optics Communications* **71**, 23-28, (1989).

29 Reddick, R. C., Warmack, R. J. & Ferrell, T. L. New form of scanning optical microscopy. *Physical Review B* **39**, 767-770, (1989).

30 Trache, A. & Meininger, G. A. *Total Internal Reflection Fluorescence (TIRF) Microscopy*. in *Current Protocols in Microbiology* 10.1002/9780471729259.mc02a02s10 (John Wiley & Sons, Inc., 2005).

31 Fish, K. N. *Total Internal Reflection Fluorescence (TIRF) Microscopy*. in *Current Protocols in Cytometry* 10.1002/0471142956.cy1218s50 (John Wiley & Sons, Inc., 2001).

32 Axelrod, D. Total Internal Reflection Fluorescence Microscopy in Cell Biology. *Traffic* **2**, 764-774, (2001).

33 Marvin, M. Microscopy apparatus. United States patent (1961).

34 Gustafsson, M. G. L. Extended resolution fluorescence microscopy. *Current Opinion in Structural Biology* **9**, 627-628, (1999).

35 Inoué, S. *Foundations of Confocal Scanned Imaging in Light Microscopy*. in *Handbook Of Biological Confocal Microscopy* 10.1007/978-0-387-45524-2_1 (ed James B. Pawley) Ch. 1, 1-19 (Springer US, 2006).

36 Walla, P. J. *Modern Biophysical Chemistry, Detection and Analysis of Biomolecules.*, (WILEY-VCH 2009).

37 Wilson, T., Shepparu, C. J. R. & Löschke, K. Theory and practice of scanning optical microscopy. Academic Press, London 1984, 213 Seiten, 138 Abbildungen, Preis $ 39.50 ISBN 0-12-757760-2. *Crystal Research and Technology* **20**, 1608-1608, (1985).

38 Brand, L., Eggeling, C., Zander, C., Drexhage, K. H. & Seidel, C. A. M. Single-Molecule Identification of Coumarin-120 by Time-Resolved Fluorescence Detection: Comparison of One- and Two-Photon Excitation in Solution. *The Journal of Physical Chemistry A* **101**, 4313-4321, (1997).

39 Kirz, J., Jacobsen, C. & Howells, M. Soft X-ray microscopes and their biological applications. *Quarterly Reviews of Biophysics* **28**, 33-130

M133 - 110.1017/S0033583500003139, (1995).

40 Shapiro, D., Thibault, P., Beetz, T., Elser, V. *et al.* in *Proceedings of the National Academy of Sciences of the United States of America* Vol. 102 15343-15346 (2005).

41 Ruska, E. über Fortschritte im Bau und in der Leistung des magnetischen Elektronenmikroskops. *Z. Physik* **87**, 580-602, (1934).

42 Ruska, E. The development of the electron microscope and of electron microscopy. *Biosci Rep* **7**, 607-629, (1987).

43 Klar, T. A. & Hell, S. W. Subdiffraction resolution in far-field fluorescence microscopy. *Opt. Lett.* **24**, 954-956, (1999).

44 Rittweger, E., Han, K. Y., Irvine, S. E., Eggeling, C. & Hell, S. W. STED microscopy reveals crystal colour centres with nanometric resolution. *Nat Photon* **3**, 144-147, (2009).

45 Heintzmann, R. & Gustafsson, M. G. L. Subdiffraction resolution in continuous samples. *Nat Photon* **3**, 362-364, (2009).

46 Schermelleh, L., Heintzmann, R. & Leonhardt, H. A guide to super-resolution fluorescence microscopy. *The Journal of Cell Biology* **190**, 165-175, (2010).

47 Heintzmann, R. Saturated patterned excitation microscopy with two-dimensional excitation patterns. *Micron* **34**, 283-291, (2003).

48 Henriques, R., Griffiths, C., Hesper Rego, E. & Mhlanga, M. M. PALM and STORM: Unlocking live-cell super-resolution. *Biopolymers* **95**, 322-331, (2011).

49 Bates, M., Huang, B. & Zhuang, X. Super-resolution microscopy by nanoscale localization of photo-switchable fluorescent probes. *Current Opinion in Chemical Biology* **12**, 505-514, (2008).

50 Michaelsen, K., Zagrebelsky, M., Berndt-Huch, J., Polack, M. *et al.* Neurotrophin receptors TrkB.T1 and p75NTR cooperate in modulating both functional and structural plasticity in mature hippocampal neurons. *Eur. J. Neurosci.* **32**, 1854-1865, (2010).

51 Riedl, J., Crevenna, A. H., Kessenbrock, K., Yu, J. H. *et al.* Lifeact: a versatile marker to visualize F-actin. *Nat Meth* **5**, 605-607, (2008).

52 L Mathivet, S. C., P F Devaux. Shape change and physical properties of giant phospholipid vesicles prepared in the presence of an AC electric field. *Biophys J* **70**, 1112-1121, (1996).

53 Orth, A., Johannes, L., RÃ¶mer, W. & Steinem, C. Creating and Modulating Microdomains in Pore-Spanning Membranes. *ChemPhysChem* **13**, 108-114, (2012).

54 Veatch, S. L. & Keller, S. L. Miscibility Phase Diagrams of Giant Vesicles Containing Sphingomyelin. *Physical Review Letters* **94**, 148101, (2005).

55 Harvey Lodish, A. B., Chris A. Kaiser, Monty Krieger, Anthony Bretscher, Hidde Ploegh, Angelika Amon, Matthew P. Scott. *molecular cell biology*. (Freeman, W. H. & Company, 2004).

56 Oda, T., Iwasa, M., Aihara, T., Maeda, Y. & Narita, A. The nature of the globular- to fibrous-actin transition. *Nature* **457**, 441-445, (2009).

57 Oda, T., Namba, K. & Maéda, Y. Position and Orientation of Phalloidin in F-Actin Determined by X-Ray Fiber Diffraction Analysis. *Biophysical journal* **88**, 2727-2736, (2005).

58 Lorenz, M., Popp, D. & Holmes, K. C. Refinement of the F-Actin Model against X-ray Fiber Diffraction Data by the Use of a Directed Mutation Algorithm. *Journal of Molecular Biology* **234**, 826-836, (1993).

59 Wu, Y. & Ma, J. Refinement of F-Actin Model against Fiber Diffraction Data by Long-Range Normal Modes. *Biophysical journal* **86**, 116-124, (2004).

60 Hafi, N., Grunwald, M., van den Heuvel, L. S., Aspelmeier, T. *et al.* Reply to "Polarization modulation adds little additional information to super-resolution fluorescence microscopy". *Nat Meth* **13**, 8-9, (2016).

Acknowledgements

اللهم لك الحمد

I would like to express my appreciations to those people who have given me their time, assistance and patience so generously; I would like also to say "Thanks" for those that might I forget to mention them in my acknowledgements.

To my parents, brothers and sisters, I would like to thank them for their financial and moral support during my studies. I would like to express my deepest appreciation for each member of my family; My deceased mother Fatima, my father Murshid, my brothers; Bashar, Mohammad and Baha'a and finally my sisters; Alaà and Doaà for their support. To my brothers 'Baha, I would like to thank him especially for his financial and moral support during my studies.

I would like to exhibit my deepest gratitude to my Prof. Peter Jomo Walla for his care, his consistent trust and his support. I thank him also for giving me the opportunity to join his research team.

I would like to express my sincere thanks for all my colleagues and friends for their support and their valuable discussions.

Many thanks for Prof. Dr. Martin Korte and Dr. Marta Zagrebelsky Holz for providing the nerve cells samples. As well as many thanks for Professor Dr. Claudia Steinem Ole M. Schütte for providing the GUVs samples

Special thanks and appreciation to the group in Max Planck Institute, Göttingen for the valuable support, discussions and suggestions.

Finally, I would like to dedicate this work to my parents for their unending support, willingness to accept and eagerness to love.